ANTIMONY DOPED P-TYPE ZINC OXIDE FOR PIEZOTRONICS AND OPTOELECTRONICS

A Dissertation
Presented to
The Academic Faculty

By

Ken C. Pradel

In Partial Fulfillment
Of the Requirements for the Degree
Doctor of Philisophy in
School of Materials Science and Engineering

Georgia Institute of Technology

December, 2015

ANTIMONY DOPED P-TYPE ZINC OXIDE FOR PIEZOTRONICS AND OPTOELECTRONICS

Approved by:

Dr. Zhong Lin Wang, Advisor
School of Materials Science and Engineering
Georgia Institute of Technology

Dr. Elsa Reichmanis
Scool of Chemical and Biological Engineering
Georgia Institute of Technology

Dr. Benjamin Klein
School of Electrical and Computer Engineering
Georgia Institute of Technology

Dr. Preet Singh
School of Materials Science and Engineering
Georgia Institute of Technology

Dr. Meilin Liu
School of Materials Science and Engineering
Georgia Institute of Technology

Date Approved: October 6, 2015

ACKNOWLEDGEMENTS

I would like to start by thanking my advisor, Dr. Zhong Lin Wang, for his support and guidance during my time here at Georgia Tech. I will never forget the trust and academic freedom he gave me to pursue a research topic that would not only be challenging, but may have proven fruitless, as it has for so many other researchers in the past. It is thanks to him that I was able to carve out my own niche, and pursue a project I could truly be passionate about.

I would also like to thank my committee members for their assistance over the years. I would like to thank Dr. Elsa Reichmanis for leading the IGERT program, which showed me the bigger picture my work could have through its integration of scientific and public policy courses. I would like to thank Dr. Preet Singh for the numerous conversations about research and life on the walks to and from IPST. Next, I would like to thank Dr. Meilin Liu for teaching many of the fundamental concepts that form the foundation of my knowledge of materials science through the courses I took with him. I would like to thank Dr. Benjamin Klein for giving me the opportunity to investigate more exotic applications of my material in radiation detection through our collaborative effort with Dr. Nolan Hertel. Finally, I would like to thank Dr. Christopher Summers, who could not be present at my thesis defense, but was a key member of my proposal committee, and always a great source of advice.

I would like to thank all the members of Dr. Wang's group, for their help and support. First and foremost, I would like to thank Dr. Wenzhuo Wu, who helped guide my work during my career here, and helping me find greater context and application for my

research. I would have been completely lost in my research had you not reached out and taken interest in my work. I would also like to thank Dr. Yong Ding for his technical assistance and constant moral support. Your great interest in my research was always a major motivator to develop new novel structures for us to probe together. I would also like to give special thanks to Drs. Youfan Hu, Zong-Hong Lin, Yusheng Zhou, Xiaonan Wen for their advice and friendship. To all the other members of the group, both past and present, and too numerous to list, I thank you for all your help as well. I would also like to thank Dr. Naoki Fukata, his group, and the staff at NIMS for everything during my term in Japan as part of the EAPSI program. This was easily the most rewarding experience of my graduate career, and I will never forget the time I spent there.

Lastly, I would like to thank everyone else who supported me during my career. My parents, Daniel and Chari Pradel, for their constant love and guidance. Thank you for laughing with me during the good times and being a shoulder to cry on during the hard ones. I would like to thank Dr. Jiaxing Huang at Northwestern University for inspiring me to pursue graduate school and research. Thank you to all the friends I made during my years in Atlanta, especially Major White, Ashley, Sean, Phil, Samson, and Yisha for all your moral support. I would like to thank my idols and muses, which are too many to count. Finally, I would like to thank my cat Fatty, for being a constant source of amusement.

TABLE OF CONTENTS

LIST OF TABLES

LIST OF FIGURES

SUMMARY

Zinc oxide is a semiconducting material that has received lot of attention due to its numerous proeprties such as wide direct band gap, piezoelectricity, and numerous low cost and robust methods of synthesizing nanomaterials. Its piezoelectric properties have been harnessed for use in energy production through nanogenerators, and to tune carrier transport, birthing a field known as piezotronics. However, one weakness of ZnO is that it is notoriously difficult to dope *p*-type. Antimony was investigated as a *p*-type dopant for ZnO, and found to have a stability of up to 3 years, which is completely unprecedented in the literature. Furthermore, a variety of zinc oxide structures ranging from ultra-long nanowires to thin films were produced and their piezotronic properties were demonstrated. By making *p*-*n* homojunctions using doped and undoped ZnO, enhanced nanogenerators were produced which could see application in gesture recognition. As a proof of concept, a simple photodetector was also derived from a core-shell nanowire structure. Finally, the ability to integrate this material with other semiconductors was demonstrated by growing a heterojunction with silicon nanowires, and investigating its electrical properties. All this work together lays the foundation for a fundamentally new material that could see application in future electronics, optoelectronics, and human-machine interfacing.

CHAPTER 1: INTRODUCTION

Since the term was first coined in 2007,[1] the field of piezotronics has grown to envelop numerous applications in tactile sensing and energy generation. The key to piezotronics has been coupling a material's piezoelectric and semiconducting properties to tune carrier transport through the material. This provides a novel alternative to the electrically induced field effect used in conventional electronics. An expansion of the concept of piezotronics is the piezophototronic effect, where the piezopotential is used to tune the materials optoelectronic properties, for applications such as enhanced light emitting diodes and solar cells.

For the vast majority of these studies, the material of choice has been naturally *n*-type ZnO nanowires as they are single crystalline and easy to synthesize. However, there have been few studies on the piezoelectric and piezotronic properties of *p*-type materials. As a II-VI semiconductor, the obvious candidates for doping ZnO are either group I elements such as Li or Na, or group V elements like N or P. Part of the difficulty in *p*-type doping ZnO is the formation of low energy compensating donors such as hydrogen or zinc interstitials. Furthermore, some dopants such as nitrogen which should theoretically work well due to their similar atomic radius actually form deep acceptor states, and therefore cannot produce p-type conductivity.[2] If stable *p*-type ZnO can be realized, then it is possible to produce homojunction based devices with more complex piezotronic functionality. Furthermore, it could find application in integration with other non-piezoelectric semiconductors for other optoelectronic applications.

Over the past four years, I have worked on developing stable *p*-type ZnO in order to investigate its piezoelectric and piezotronic properties. Using antimony doped *p*-type ZnO; I demonstrated that the piezotronic effect is universal to all piezoelectric semiconductors regardless of carrier type. Furthermore, I thoroughly investigated the growth, producing *p*-*n* homojunction architectures, such as stacked films, and core-shells and used these structures to investigate its piezoelectric, and optoelectronic properties. Finally, in a collaborative effort with the National Institute for Materials Science in Japan, I integrated *p*-type ZnO nanowires with n-type silicon nanowires to demonstrate its compatibility with other materials systems by investigating its applications in photodetection.

CHAPTER 2: LITERATURE REVIEW

2.1 Harnessing Piezopotential: Nanogenerators, Piezotronics, and Piezophototronics

Piezoelectricity is a phenomenon where an electrical potential is induced in a material due to an applied strain. Lead zirconium titanate (PZT), a perovskite material, has one of the higher piezoelectric coefficients, and has seen numerous applications in sensors and actuators. However, it is also difficult to reliably produce nanostructures of, and the presence of lead makes it undesirable for biological applications. As a result, wurtzite materials such as zinc oxide (ZnO) has served as the model system for piezoelectric nanogenerators and piezotronics due to the wide variety of techniques available to produce high quality nanostructures.[3] In ZnO, the Zn^{2+} cations and O^{2-} anions are tetrahedrally coordinated, and the charge centers overlap. When a strain is applied, the charge centers are displaced relative to each other, resulting in a dipole moment. These dipole moments add up along the length of the material, resulting in a potential drop, known as piezopotential. This phenomenon has been harnessed for several applications: piezoelectric nanogenerators for energy harvesting, piezotronics for strain sensing, and piezophototronics for optoelectronics.[4]

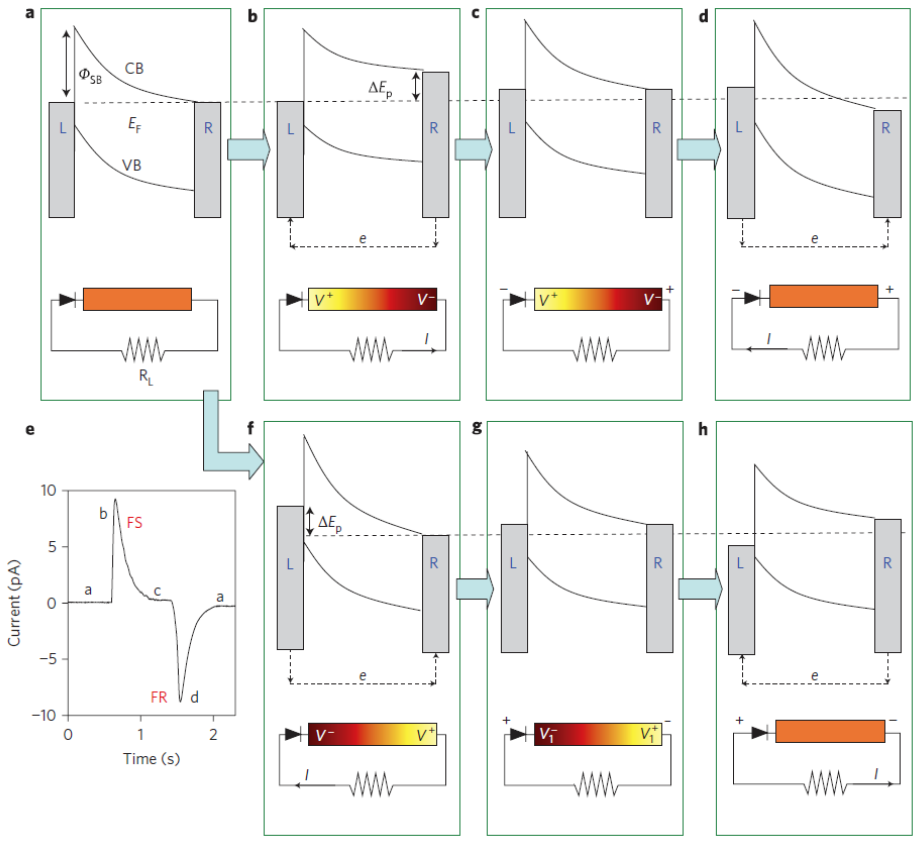

Figure 1 Mechanism for current generation in single wire nanogenerators. Under tension or compression, the Schottky barrier height at the end with negative piezo-polarization charges will be raised, driving electrons away through an external circuit, producing a positive current pulse. When the stress is released, the piezo-polarization charges disappear, so the electrons which had accumulated at the Schottky barrier flow back through the circuit producing a negative current pulse. [5]

ZnO nanowire based nanogenerators have been investigated starting from a proof of concept using single nanowires[6] to devices consisting of arrays of wires capable of driving consumer electronics.[7] For a simple single wire nanogenerator, each end of the wire is fixed to an electrode, with one side forming a Schottky contact, and the other an Ohmic contact as illustrated in Figure 1.[5] When strained, the induced piezopotential raises the conduction band and Fermi level on the negative side, driving electrons through an external circuit from the negative to the positive end, producing a current spike. As the electrons do not have enough energy to overcome the Schottky barrier, they accumulate at the metal-

semiconductor interface. Eventually, the potential created by the accumulated electrons balances that of the piezopotential, and a new equilibrium Fermi level is reached. When the strain is released, and the nanowire relaxes, the piezopotential disappears, and all the electrons which had accumulated at the Schottky barrier flow back through the external circuit in the opposite direction, producing a reverse current spike. By cyclically straining and releasing the nanogenerator, alternating current can be produced. This fundamental concept can be harnessed and applied to develop electronics powered by the surrounding environment, known as self-powered systems.[8] Over the years the output and efficiency of the nanogenerator has improved from single wire devices able to produce 6.5 mV at 13 pA,[6] to large arrays with an output of 58V and current of 134 μA.[9]

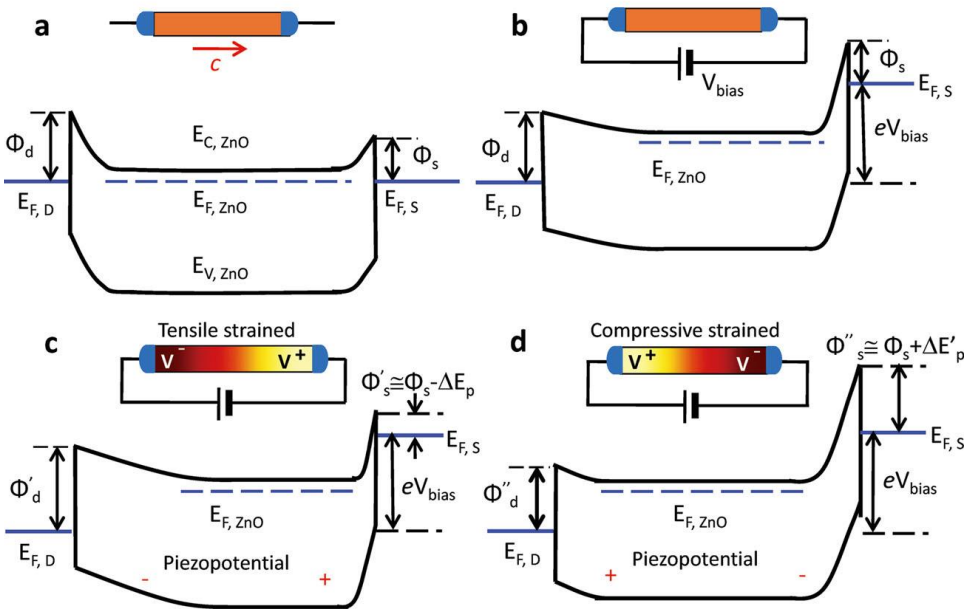

Figure 2 Schematic representation of the piezotronic effect. (a) Band structure of a ZnO nanowire with two Schottky contacts at equilibrium. (b) When an external bias is applied, quasi-Fermi levels form at each end. (c) Under tensile strain, the Schottky barrier height at the source end is reduced, due to the positive piezopotential, while the barrier height at the drain end is increased. (d)The opposite trend is observed under compressive strain.[10]

When applied to piezotronics, this same piezopotential is used to tune the flow of current through the nanowire.[1, 11-13] In a typical setup for *n*-type nanowires, a pair of Schottky contacts is formed between the nanowire and metal electrodes (Figure 2a). Under forward bias (Figure 2b), quasi-Fermi levels form at the metal-semiconductor contacts. When the material is strained, the Schottky barrier height will decrease on the end with positive piezopotential, while the barrier height will increase on the end with negative piezopotential. If the doping level in the nanowire is finite, these immobile ionic charges are partially screened and attract the majority charge carrier, in this case electrons, towards the metal-semiconductor interface, lowering the barrier height. Depending on the whether the wire is under tensile (Figure 2c) or compressive (Figure 2d) strain, the conductivity will increase or decrease under the same bias direction. This behavior is analogous to a typical MOSFET, except rather than using an applied electric field to control the flow of current, an applied strain is used. Similarly to nanogenerators, initial investigations were performed on single nanowires for applications such as logic[10] and memory[14] units. As the technology has been improved, arrays for tactile sensing have also been produced.[15]

Piezophototronics expands upon the previous concepts by coupling piezoelectricity with the materials optoelectronic properties.[12, 16] By shining a laser with a higher energy than the bandgap of ZnO on a Schottky junction, the barrier height can be lowered. As the barrier height can be changed by straining the nanowire through the piezotronic effect, the transport properties of nanowire devices can be precisely tuned through controlled application of strain and light to make a Schottky contact Ohmic or vice versa.[17] The piezophototronic effect has been used to improve the sensitivity of photodetectors[18-20] by optimizing the Schottky barrier height to allow for efficient electron-hole recombination.

Furthermore, this effect is also applicable to *p*-*n* junctions for enhanced solar cells[21, 22] and LEDS.[23] By tuning the barrier height of the *p*-*n* junction, the conversion efficiency or luminescence of these two devices could be improved. As with piezotronics, this was initially investigated using single wire devices, and later expanded to array, allowing for applications such as pressure enhanced electroluminescent imaging.[24]

2.2 Hydrothermal Synthesis of ZnO

A wide variety of techniques exist to synthesize ZnO nanowires, each with their own strengths and weaknesses. Vapor based techniques such as vapor-liquid-solid or vapor-solid-solid, produce single crystalline nanowires with a low defect density and long length,[25] but these methods require very high temperatures, on the order of 900-1300 °C, which limits the choice of substrates for growth. Molecular beam epitaxy (MBE) has also been used to produce high purity single crystalline ZnO nanorods.[26] However, MBE is a costly and slow process due to its high vacuum requirements. Solution based hydrothermal growth has proven to be one of the most popular means of producing ZnO nanowires with several advantages over the aforementioned methods.[27] First, it is low cost, as the precursors needed are relatively inexpensive, and no special equipment is needed outside of a furnace and glass jars. Next, it can be performed on a number of different substrates, including polymers, due to the low temperature needed (65-95°C), enabling applications in flexible electronics. The growth can also be easily scaled up, allowing for uniform wafer scale growth.[28] Finally, the nanowire dimensions can be easily tuned by adjusting growth parameters such as temperature, time, or precursor concentrations.[29]

In its most basic form, hydrothermal synthesis of ZnO nanowires is performed by mixing a zinc salt, such as zinc nitrate or zinc chloride, with equal molar parts hexamethylenetetramine (HMTA) in water. A substrate with a seed layer is placed in the solution, and is heated in an oven anywhere for several hours. To avoid agglomeration of homogeneously nucleated material on the substrate, it is typically floated on the solution surface, seed layer down. HMTA acts as a weak base, which slowly hydrolyzes water to provide oxygen as shown in the following reactions:[30]

$$(CH_2)_6N_4 + 6H_2O \leftrightarrow 4NH_3 + 6HCHO \quad (1)$$

$$NH_3 + H_2O \leftrightarrow NH_3 \cdot H_2O \quad (2)$$

$$NH_3 \cdot H_2O \leftrightarrow NH_4^+ + OH^- \quad (3)$$

The resulting OH^- anions react with the Zn^{2+} cations from the salt to form ZnO as follows:

$$Zn^{2+} + 2OH^- \leftrightarrow Zn(OH)_2 \quad (4)$$

$$Zn(OH)_2 \leftrightarrow ZnO + H_2O \quad (5)$$

As a result, the growth rate is highly dependent on the pH of the solution, and has been shown to reach a maximum at a pH of 10.6.[31] At higher levels, it has been suggested that subreactions such as the dissolution of ZnO occur, slowing down growth. ZnO naturally forms aligned wires as it grows preferentially along the [0001] direction.[32] Additionally, by forming a wire it minimizes the surface area of the high energy (0001) surface.

In order to facilitate growth, a seed layer is commonly added to the substrate of choice. Some commonly used seed layers are gallium nitride, gold, and zinc oxide. GaN produces very well aligned vertical nanowires due to the good lattice matching between the two materials.[33] When used in conjunction with a mask defined through electron beam[34] or laser interference lithography,[35] large patterned arrays of wires can be produced.

However, sapphire substrates coated with GaN are expensive and rigid, limiting its practical applications. While Au can be sputtered onto a variety of substrates, thermal annealing is required to improve the crystallinity of the surface so that growth is more favorable.[36] Despite this, the growth density is still relatively low. ZnO deposited through physical vapor deposition is one of the more effective seed layers as it should naturally have perfect lattice matching.[37] Factors such as seed layer thickness and doping have also been shown to have an effect on nanowire growth rate and alignment.[38] As the seed layer becomes thicker, the sputtered ZnO grains become larger, allowing for wires with a larger diameter at the cost of number density. Because the larger grains also increase the surface roughness, the wire alignment becomes poorer as a result.

Adjusting the growth parameters directly affects the resulting nanowires.[29] Temperature was found to be one of the larger determinants of nanowire morphology. At very high or low temperatures, the growth density of the nanowires decreases. This was attributed to basic kinetics of nucleation and growth. At low temperatures, the Zn ions cannot diffuse as easily, which results in large nuclei. On the other hand, if the temperature is too high, the growth material will have a higher affinity to the already formed nuclei, resulting in more growth, but less nucleation. A similar trend is observed with changes in precursor concentration. Increasing the concentration of zinc nitrate and HMTA improves deposition density until it reaches a saturation point. This can also be explained by nucleation and growth phenomena. With a higher precursor concentration, more nucleation sites are needed to balance out the increased chemical potential. However, once the concentration goes beyond the saturation point, it is more probable that the Zn ions will attach to the existing nanorods rather than form new nuclei. By investigating growth time,

one can observe the growth flow.[39] During the initial stages, lateral growth dominates. Next, the nanowires will continue growing axially while the width remained constant. Eventually, the wires will continue to grow in both directions, becoming longer and wider.

Hydrothermal growth can be controlled further through the use of chemical additives. When sodium citrate is added to the growth, lower aspect ratio wires are produced.[40] This is attributed to the citrate ions binding preferentially to the (0001) surface, which inhibits lateral growth in favor of axial growth. With a high enough citrate concentration, stacked plates will form instead. Changing the zinc source to zinc chloride or acetate has been shown to have a similar effect, and have been used to produce ZnO nanosheets[41] and films[42] respectively. Polymers such as polyvinyl alcohol (PVA)[43] and polyethylenimine (PEI)[28] have been shown to have the opposite effect, binding to the $(01\bar{1}0)$ and $(2\bar{1}\bar{1}0)$ faces, promoting higher aspect ratio nanowires. PEI can be used in conjunction with high concentrations of ammonium hydroxide to grow ultra-long ZnO nanowires.[44] During growth, material is lost due to homogeneous nucleation and growth in solution, depleting nutrients away from the seeded substrate where growth is desired. While the increase in pH should cause ZnO to precipitate out, the ammonia groups complex with the Zn^{2+} ions to inhibit nucleation.[45] As the solution is heated, the ammonia slowly evaporates, releasing Zn^{2+} for the reaction to progress. Using this system, it is possible to produce nanowire arrays over 60 μm long.[46]

2.3 *p*-type Doping of ZnO

Successful *p*-type doping of ZnO has remained a controversial field of study for several years.[47, 48] As synthesized ZnO is typically *n*-type due to the ease of formation of

intrinsic defects such zinc[49] or hydrogen[50] interstitials, which act as donors. It was previously believed that oxygen vacancies were responsible for the unintended *n*-type conductivity due to their low formation energy, but first principles calculations have proven that not to be the case, as oxygen vacancies form a deep donor state.[51] Other studies have suggested that a more complex donor complex containing Zn_i-V_O complexes[52] or metastable oxygen vacancies[53] could explain ZnO's *n*-type behavior. As a II-VI semiconductor, group I or V elements should act as *p*-type dopants in ZnO. The primary challenge is introducing acceptors into the material without forming more compensating donor defects as a result. Molecular beam epitaxy and vapor-liquid-solid nanowire growth have been used to achieve *p*-type ZnO,[48, 54-59] but as these techniques are costly or limited in terms of substrate compatibility, here I will narrow the scope to focus on hydrothermally grown nanowires.

Group I elements such as lithium have been used to produce *p*-type ZnO nanowires[60] through the hydrothermal method due to its low acceptor energy. In the as grown nanowires, it was found that the Li ions primarily occupied interstitial sites. While Li should act as an acceptor when in the Zn site (Li_{Zn}^{1-}), more often it forms an interstitial due to its smaller atomic radius, making it act as a donor (Li_i^{1+}). By annealing the sample in oxygen at 500°C, the Li ions migrated to the Zn sites to produce *p*-type conductivity, which was verified using a single nanowire field effect transistor (NWFET). By growing the nanowires on an *n*-type seed layer, a pn homojunction with typical rectifying behavior was demonstrated, with a turn-on voltage of 5.5 V.

Potassium has also been used to produce *p*-type conduction in densely packed ZnO nanorod films.[61, 62] When a small concentration of dopant was added to the growth, strong

p-type conduction was observed in as-grown films using Hall Effect measurement. However, as the concentration increased, the hole concentration decreased until the sample became *n*-type again. At low dopant concentrations, the majority of the K ions enter the Zn sites, forming acceptors. However, as more potassium is incorporated, an increasing number form interstitials, which cancel out and eventually overwhelms the acceptors. Due to the limited incorporation of potassium in acceptor sites, the only way to achieve higher hole concentrations was to anneal the ZnO at elevated temperatures to out-diffuse hydrogen and potassium interstitials.[62]

Group V elements such as phosphorus[63, 64] have also been used to achieve *p*-type conduction in ZnO. Ammonium phosphate ($NH_4H_2PO_4$) was used as the dopant source in both works. It was proposed that P is doped through the formation of $Zn_3(PO_4)_2$ in solution, which is incorporated into the nanorods during growth.[63] By annealing the sample, the P ions could be released to form P_{Zn}-$2V_{Zn}$ acceptor complexes. A later study on this same system showed that by adding ammonium hydroxide to the growth solution, the dopant concentration could be improved.[64] As $Zn_3(PO_4)_2$ is more soluble than ZnO in a basic solution, by increasing the solution pH, more P ions can be released. In both cases, homojunction structures were produced by growing a layer of *p*-type nanorods on top of a layer of *n*-type nanorods, and the rectification behavior was measured.

Of the group V elements, antimony has displayed the highest level of stability. As Sb has a much higher atomic radius than oxygen, one theory suggests that the Sb enters the Zn site to form a Sb_{Zn}-$2V_{Zn}$ complex to produce *p*-type doping, rather than entering the oxygen site.[65] Sb atoms were incorporated into the ZnO lattice by coordinating them with glycolate ligand. During growth, antimony glycolate is absorbed onto the growing surface

of the nanowire, and the glycolate ligand desorbs, leaving the Sb ion behind, while normal ZnO growth continues.[66] Single wire field effect transistors showed *p*-type conduction in doped wires, even without annealing. While the carrier concentration for both samples was similar, annealing led to a huge improvement in carrier mobility from 0.03 to 1.2 $cm^2V^{-1}s^{-1}$. A follow up STEM study showed that the incorporation of Sb led to the formation of head to head basal plane inversion domain boundaries.[67] ZnO naturally grows much faster along the positive c-axis, compared to the negative c-axis, so growth continues around the dopant plane leading to the formation of voids. From density functional theory calculations, they found that an extra basal plane of oxygen atoms acted as electron acceptors, and were the source of the nanowires' *p*-type characteristics. Doped ZnO nanowires grown using this method have shown stable *p*-type conductivity for an unprecedented 18 months,[67] making Sb one of the more promising doping candidates.

2.4 *p*-type Piezontronics

Some preliminary studies have been performed on the piezoelectric properties of *p*-type ZnO. When ZnO nanowires are deformed using conductive AFM, the sign of the output voltage will change depending on the primary charge carrier.[55, 68] When the AFM tip bends the nanowire, positive and negative piezopotential is induced along the stretched and compressed sides, respectively. In an *n*-type nanowire, the free electrons accumulate at the stretched side, screening the positive piezopotential. The remnant positive piezopotential creates a reversely biased Schottky barrier between the nanowire and the AFM tip which blocks the flow of electrons. When the AFM tip scans over to the compressed end, the negative piezopotential creates a forward biased Schottky barrier,

which drives electrons through the tip, producing a negative transient current spike. Conversely, in *p*-type nanowires, a forward biased Schottky barrier is formed when the tip contacts the stretched side with positive piezopotential, as the free holes are accumulating at the compressed side. This drives charge carriers from the tip to the nanowire, producing a positive current spike. Using this method, the primary charge carrier of doped piezoelectric nanowires can be identified through the polarity of the piezoelectric output. Even if a core-shell *p*-*n* structure is made, the piezoelectric behavior will obey that of the shell layer, as the nature of the output is an interface effect.[68]

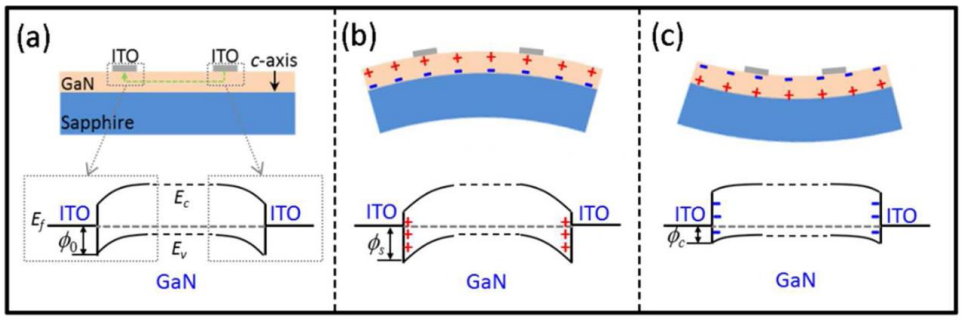

Figure 3 Demonstration of the piezotronic effect in *p*-type GaN films. As the electrodes are located on the same side, applied strain causes equal changes to their Schottky barrier height.[69]

p-type GaN thin films have been used to demonstrate the piezophotronic effect.[69] Mg-doped GaN films were grown on sapphire substrates using metal organic chemical vapor deposition (MOCVD), and indium tin oxide (ITO) electrodes were deposited on the surface to form Schottky contacts (Figure 3a). Unlike nanowires, in this case, the piezotronic effect is symmetrical as the two contacts are on the same side. When the substrate was bent, such that the film was under compressive strain (Figure 3b), positive piezoelectric charges are generated at the metal-semiconductor contacts. As the material is *p*-type, this raises the Schottky barrier height, reducing the film's conductivity. Conversely, under tensile strain (Figure 3c), negative charges accumulate at the interface, causing the

barrier height to decrease, thus improving conductivity. By straining the film, the electroluminescent intensity of the film can be adjusted, as the change in barrier height tunes the minority carrier injection efficiency. When positive piezoelectric charges form at the Schottky junction, the barrier for electron injection into the *p*-type GaN material is decreased as the positive charges attract electrons from the external circuit.

2.5 Piezopotential and *p-n* junctions

The piezoelectric properties of ZnO can be further modified through the formation of a *p-n* junction. In addition, to the aforementioned piezophototronic effect, *p-n* junctions with ZnO have been also shown to have a beneficial effect on nanogenerator output.[70, 71] When a *p-n* junction forms, the free electrons and holes in each layer redistribute to balance the local potential, forming a charge depletion region. Because of the lower free charge carrier concentration, the internal screening is reduced, so the output should increase.[12] This has been demonstrated previously with the formation of a heterojunction with the *p*-type conducting polymer poly(3-hexylthiophene-2,5-diyl) (P3HT).[70] Over 4 times the output voltage was observed compared to a single piezoelectric layer. However, the improvement was found to be dependent on the direction in which the device was strained. Under forward load, the film is under tensile strain, so a positive piezopotential forms at the interface with the junction, while a negative one forms at the electrode. In this case, enhancement is observed due to the aforementioned reasons. However, when the device was bent in reverse, no such enhancement was observed. In this case, the negative piezopotential forms at the junction region. Because the negative piezopotential cannot effectively drive charges through the *p*-type layer, the overall potential is reduced.

Additionally, it has been shown that a *p*-*n* junction can be used to replace the Schottky contact used in traditional piezoelectric nanogenerators.[71] If ZnO is strained such that a positive piezoelectric polarization charge forms at an Ohmic contact, and a negative charge at the *p*-*n* junction , the positive piezoelectric polarization charge is quickly screened by free electrons from the material and external circuit. On the other hand, the negative charge is screened much more slowly for two reasons. First, the free carrier density and mobility is much lower in the *p*-type polymer compared to a metal contact. As such, while the potential will eventually be completely screened, it will happen much slower than with an Ohmic contact. Secondly, the depletion region has a built in electric field which cancels out the piezo-polarization electric field, slowing down the rate of screening.

2.6 Zinc Oxide/Silicon Heterojunctions

Nanoscale heterojunctions between ZnO and other semiconducting materials has been extensively studied for applications in optoelectronics.[72-75] Silicon has been the natural choice as the basis for these devices as it is a ubiquitous material which forms the basis for much of our modern technology. Similarly to ZnO, a variety of synthetic techniques exist to produce Si nanowires,[76] such as the previously described VLS method,[77] electron beam lithography,[78] and nano-imprint lithography.[79-81] This last technique is of particular interest as it can produce complex structures at a high throughput and low cost. In brief,[79] first the substrate of choice is coated in a resist, such as polymethyl methacrylate (PMMA), and a master mold with the desired pattern is pressed into it while the substrate is heated above the resist's glass transition temperature, transferring the

pattern to the resist. Next, the resist is etched using reactive ion etching (RIE), selectively exposing the patterned regions. As the mold can be reused, it is possible to continuously replicate high resolution patterns produced through slower techniques such as electron beam lithography at a much faster pace, making this of practical use for industry.

This is followed by a deposition of chromium and liftoff which will be needed to define nanowires for the Bosch process.[82] In the Bosch process, the silicon is exposed to alternating sulfer hexafluoride (SF_6) and Octafluorocyclobutane (C_4F_8) plasma. The first plasma acts as an etchant while the latter forms a passivation layer over the Si surface. Because the SF_6 plasma is highly directional, it will sputter away the passivation layer and expose the bottom of the substrate faster than the side walls of the nanowire, allowing for uniform etching of the substrate. This is repeated over several hundred cycles, producing Si nanowires with minimal tapering.

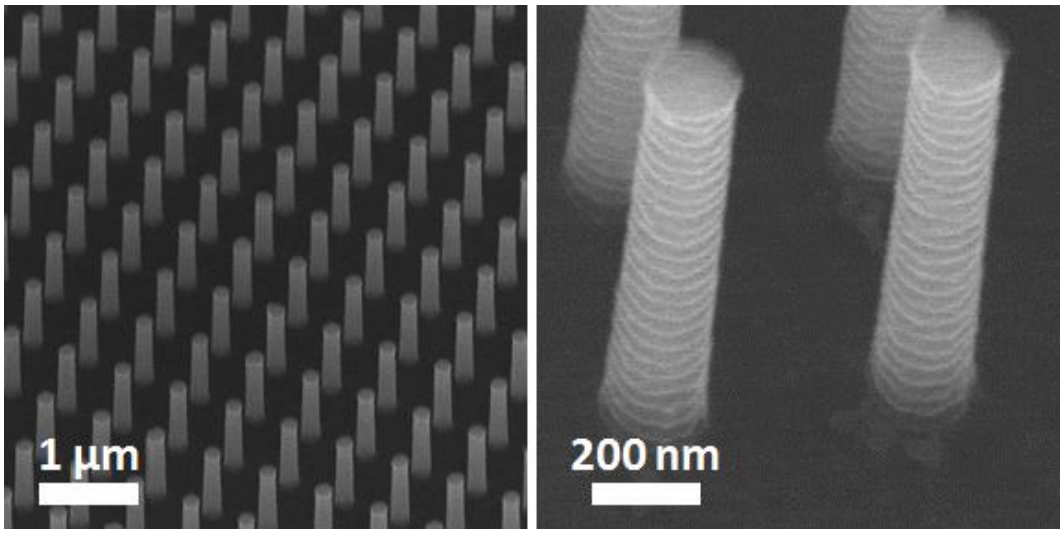

Figure 4 Silicon nanowire array patterned and grown using nano-imprint lithography and the Bosch process.

One commonly seen application of ZnO/Si heterojunctions is photodetectors. Because of the nanoscaled features, there is a significantly higher contact area between the *n* and *p*-type semiconductors, which should improve the device sensitivity.[72] Furthermore,

ZnO has a high refractive index which could help in light trapping. Other works have shown that the piezophototronic effect can be applied to heterojunction structures.[75] ZnO nanowires were grown on a micropatterned Si substrate in order to improve light absorption. By applying a compressive strain to the nanowire array, the authors were able to adjust the device's sensitivity, with a relative enhancement of up to 177%. When the ZnO nanowires are strained, the positive piezo-polarization charges that form at the interface between the Si and ZnO cause the depletion width to expand in the *p*-Si side, increasing the photon-absorption volume. On the ZnO side, the piezo-polarization charges form an electron trap, which slows down the separation of photo-generated electron-hole pairs, thus lowering the photocurrent. Therefore, a certain amount of strain optimization was needed to get the maximum enhancement in photocurrent.

CHAPTER 3: SYNTHESIS OF SB-DOPED P-TYPE ZNO NANOWIRES

3.1 Introduction

Piezoelectric semiconductors such as ZnO, GaN, InN and ZnS have attracted increased attention in the burgeoning field of piezotronics and piezo-phototronics. However, all previous studies used intrinsically *n*-type ZnO and few studies of piezotronics based on *p*-type materials, especially *p*-type ZnO have been done. In order to develop a full understanding of the theory of piezotronics, and enable novel applications in electronics and optoelectronics, it is essential to investigate the feasibility of *p*-type piezoelectric semiconductors for piezotronic applications.

p-type doping in ZnO nanowires (NWs) has been previously achieved through a variety of methods, but there have been problems with instability, causing the very feasibility of *p*-type ZnO to come into question. To date, the longest reported stability of *p*-type ZnO has been 18 months, through a solution based hydrothermal method based on antimony glycolate to control the release rate of the dopant.[66, 67] However, those solution-grown NWs were only a few μm in length, making manipulation and further experimentation difficult. To perform meaningful measurements, especially for piezotronics, significantly longer nanowires are needed.

In this chapter, the successful growth of ultra-long *p*-type ZnO NWs up to 60 μm in length using a low-temperature solution growth method will be demonstrated.[46] After verifying the carrier type using well-established experimental methods, the first reported

investigation of the piezotronic effect in *p*-type ZnO was shown and further demonstrated the sensing and energy harvesting applications of *p*-type piezotronic devices.

3.2 Synthesis and Microscopy

Doped ZnO NWs were synthesized using a modified hydrothermal method previously reported by Wang et al.[66] To produce longer wires, high concentrations of ammonia were added to the growth solution to inhibit self-nucleation.[44] A solution of 25 mM zinc nitrate ($Zn(NO_3)_2$), 12.5 mM hexamethylenetetramine (HMTA), 5 mM polyethylenemine (800 M_w PEI) and 0.8 M ammonium hydroxide was prepared. The dopant solution was prepared by mixing an equal molar ratio of sodium hydroxide (NaOH) and glycolic acid ($C_2H_4O_3$) in water. Antimony acetate ($Sb(CH_3COO)_3$) was then added to this solution in a 1:12 molar ratio. All chemicals were purchased from Sigma-Aldrich and Alfa Aesar, and used as received without further purification. Dopant with concentration between 0.2 and 2% molar relative to zinc was added to the solution. The samples were grown on silicon wafers with a 100-nm thick sputtered ZnO seed layer for 24 hours in a 95 °C oven, and corresponding results are shown in Figure 5. Considerable improvement in NW length can be seen here, with wires reaching lengths of up to 60 μm at 0.2% doping (Figure 5a), over an order of magnitude longer than those previously reported. As the doping concentration increased, the wire length decreased dramatically, while the diameter remained constantly between 200-300 nm (Figure 5a-d). Although the exact underlying mechanism for the observed change in aspect ratio (Figure 5g) is not clear, the reduced length might be attributed to the incorporated dopant providing an energetic barrier to crystal growth.[83]

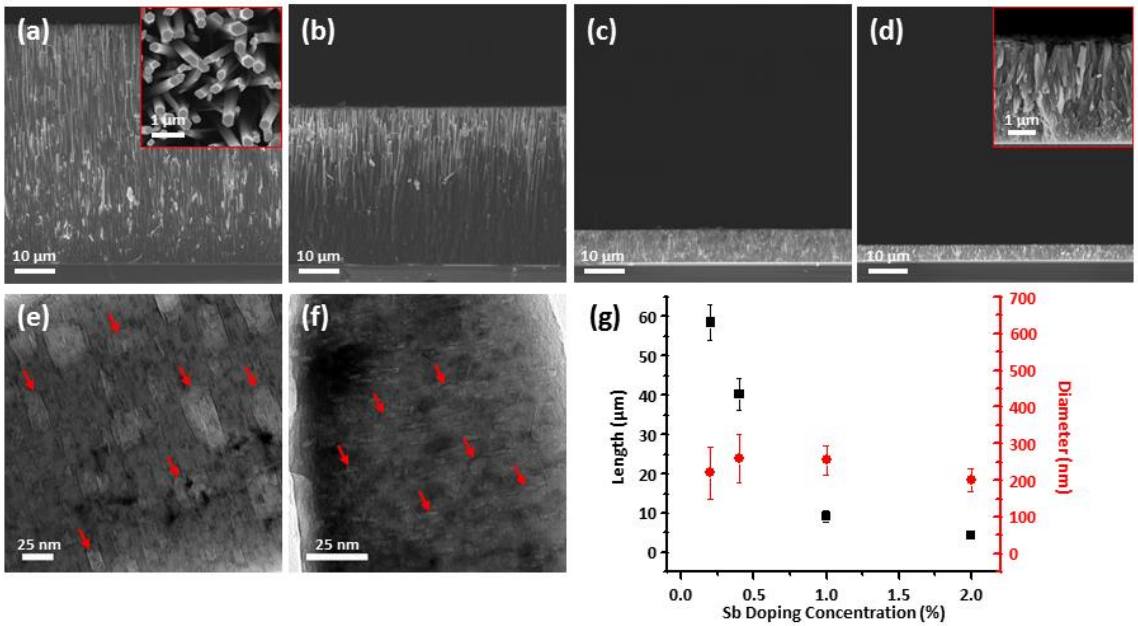

Figure 5 Cross-sectional SEM images of Sb doped *p*-type ZnO at (a) 0.2, (b) 0.4, (c) 1, and (d) 2% doping in solution. Inset in (a) shows that the wires are still distinct from one another, rather than a continuous film. HRTEM images of (e) 0.2% and (f) 2% Sb doped NWs show voids induced due to the presence of dopant, as highlighted with red arrowheads. (g) Plot of NW length and diameter as a function of doping level, showing a steady decrease in wire length, while the diameter remained constant.[46]

Voids can be observed inside the as-synthesized NWs using high-resolution transmission electron microscopy (HRTEM), which is consistent with those observed by Yankovich et al.[67] (Figure 5eand f), suggesting that the doping mechanism is the same despite the differences in growth solution and length of as-fabricated NWs. Yankovich reported that these voids form exclusively above basal planes of Sb atoms, which incorporate an extra plane of O atoms that act as acceptors. This study using scanning transmission electron microscopy also confirms the presence of Sb atomic planes in the lattice (Appendix A). This co-doping reaction explains the excellent stability of *p*-type samples previously reported. The concentration of voids increases when the dopant concentration increases from 0.2 to 2% (Figure 5f), reinforcing our previous hypothesis on the inhibition of crystal growth due to energetic barriers (Figure 5g). Significantly smaller voids are observed in the heavily doped sample as well. I believe that the formation of

dopant basal planes is related to classical precipitation kinetics.[84] In the higher doped samples, there will be more nucleation events due to the increased dopant concentration. Because of the overlapping diffusion fields of the different nucleation sites in the higher doped samples, the growth rate will quickly drop off leading to smaller dopant planes, and thus smaller voids. Due to the lower number of nucleation events in the lower doped sample, there is no diffusion overlap, allowing for faster growth of dopant planes, which form larger voids. Since the dopant is only incorporated onto the bottom face of the void,[67] a large number of small voids will incorporate more dopant into the NW than a few large ones.

3.3 TEM Analysis of Void Structure

Using electron tomography,[85] it was possible to make a 3D reconstruction of the porous structure inside the doped nanowire. Using the FEI Tecnai F30 STEM with a single tilt holder, a single nanowire was focused on, and a series of images were taken at different angles. The starting tilt was at 30° (Figure 6a), and continued until -70° (Figure 6b) with steps of 1° or 2° in between. The voids are clearly visible in this sample as the dark spots. The objects to the right of the nanowire in Figure 6b is waste organics that were caught under the nanowire. Using the accompanying IMOD Inspect3D software, the nanowire was reconstructed to get a better understanding of the nature of the pores (Figure 6c,d). Because of the limit in resolution of the microscope, it is difficult to resolve the exact morphology of the voids, especially the smaller ones, which are not included in the reconstruction. There is also some artifacting observed, especially near the walls of the nanowire, where the voids seem to meld with the surface. Despite these limitations, this method does allow

us to see that the voids are randomly distributed throughout the nanowire, not only axially, but also radially, giving some insight into their formation.

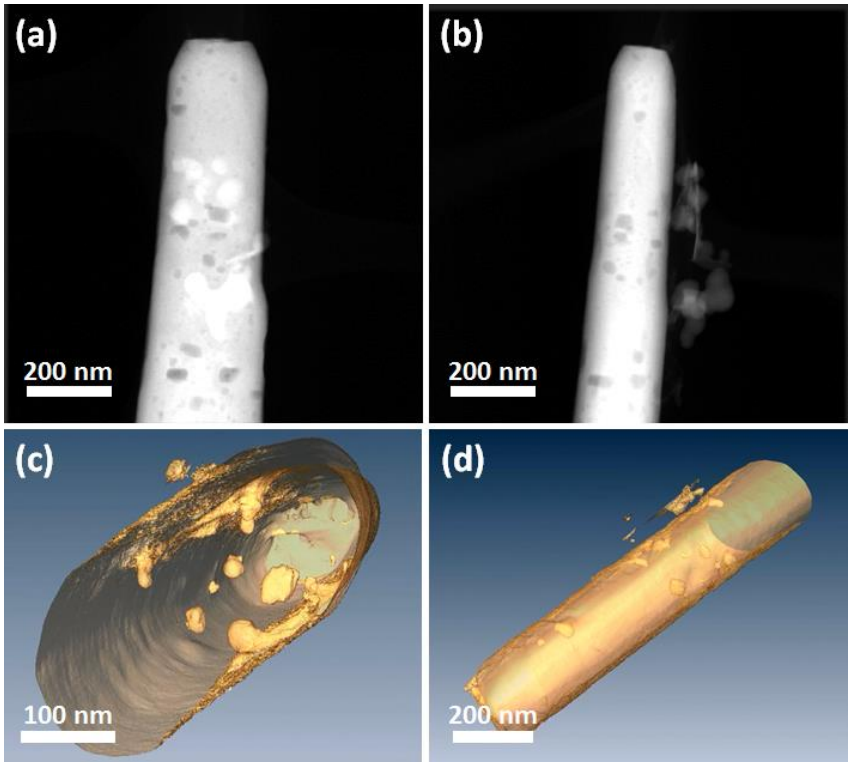

Figure 6 Electron tomography reconstruction of a 0.2% Sb doped nanowire. Doped nanowire at starting tilt of (a)30° and final position of -70°. (c,d) Three dimensional reconstruction of the doped nanowire showing the position of the voids.

Furthermore, using a Hitachi HD2700A aberration corrected STEM, it was possible to obtain high resolution images of a single doped nanowire (Figure 7). Nanowires were synthesized using similar growth conditions, but with the overall precursor concentration reduced in order to produce lower diameter nanowires. The doping concentration was kept at 0.2%, and the nanowires were annealed at 850°C to activate the dopant. Thanks to the smaller diameter, and higher power of this STEM, it is possible to observe much higher contrast from the voids in the overview image (Figure 7a). While some faceting is observed in this image, a zoomed in view shows that the void growth is not completely regular

(Figure 7b). The left side of the void in the image is where Sb was integrated into the nanowire during growth. As growth continued, the void expanded outward for a few atomic layers before contracting back in. Based on the changes in contrast in the void, this is clearly not a uniform process, which supports the irregular shapes seen in the previous electron tomography images. Because of the size of this void, it was difficult to get good contrast of the Sb layer. A pair of smaller voids were observed as shown in Figure 7c. In these, a plane of slightly brighter atoms can be observed to the left of the void. These match the structures previously observed by Yankovich et al. so the doping mechanism is the same despite the changes to the growth solution. Curiously, on the void to the left, this plane seems to extend a bit further past the void itself. It is possible that the annealing process gave the surrounding zinc atoms enough energy to diffuse into the voids, thus covering the antimony plane.

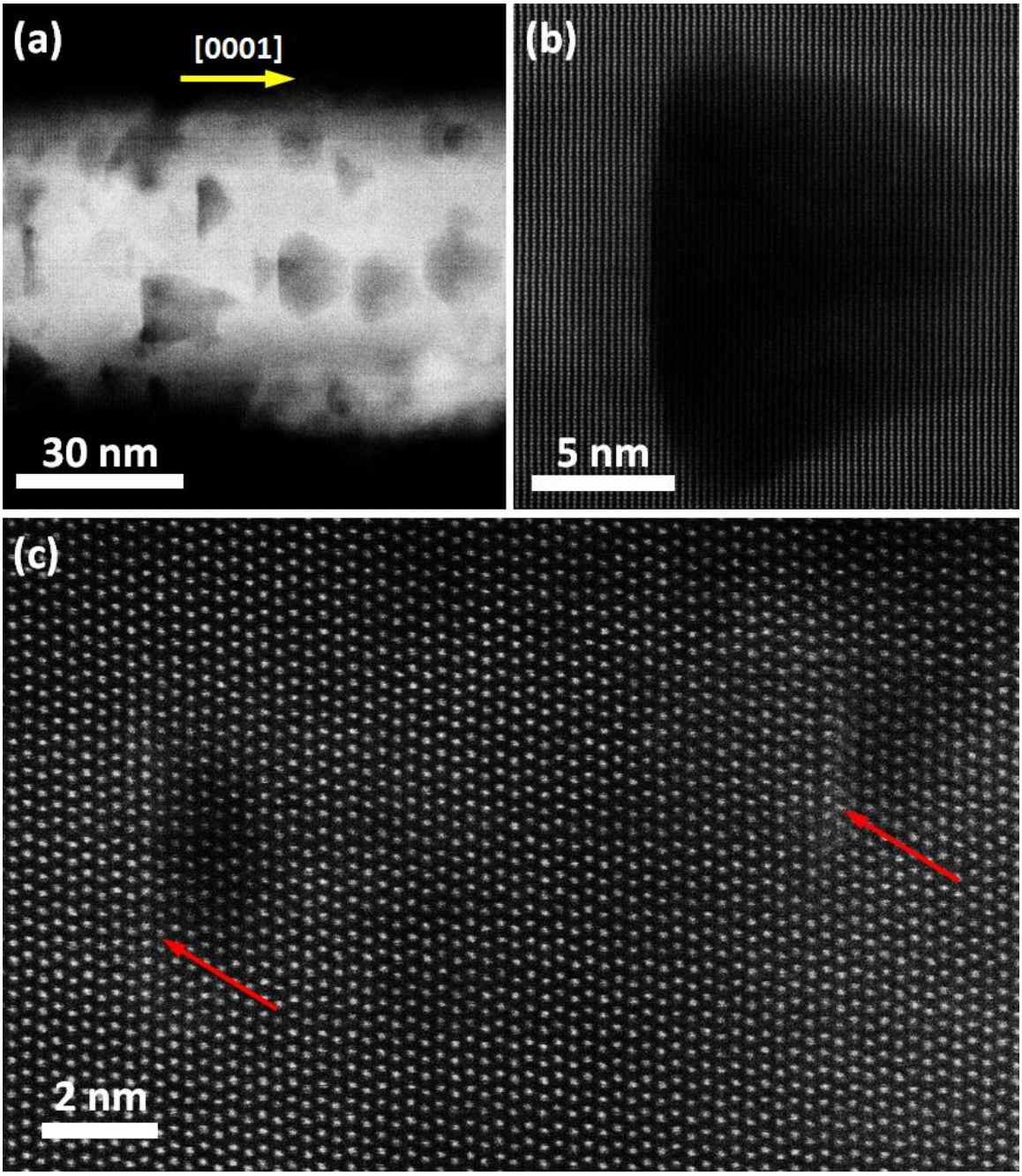

Figure 7 STEM images of a 0.2% doped nanowire taken using an aberration corrected STEM. (a) Overview of the whole nanowire with void structures clearly visible. (b) Zoomed in view of a single void. (c) High resolution images of two smaller voids. The red arrows point out the bright planes which are thought to be the Sb dopant.

3.4 Electrical Characterization

To characterize the charge carrier properties of as-synthesized ZnO NWs, single NW field effect transistors (FET) with a back-gate configuration were fabricated, as shown in the inset of Figure 8. The ZnO NWs were annealed at 850 °C in atmosphere to activate the dopants, and then re-dispersed in ethanol using ultrasonication, to transfer them to the Si substrate. A 200 nm thick SiO_2 was thermally-grown on heavily doped silicon substrates and acted as the gate dielectric. Source and drain electrodes (200-nm Ti for undoped NWs and 200-nm Ni for doped NWs) were defined by electron-beam lithography and deposited via electron-beam evaporation and standard lift-off processes. The electrical transport characteristics of the single NW FETs was measured using a semiconductor parameter analyzer (Keithley 4200), with results for both undoped (0%) and doped samples (0.2% and 1%) compared in Figure 8. The undoped ZnO NW-FET exhibited typical *n*-type characteristics with a threshold voltage of -2.8 V and on/off ratio of 10^4 (Figure 8). The mobility and carrier concentration were calculated as 3.22 $cm^2 \cdot V^{-1} \cdot s^{-1}$ and 2.2×10^{17} cm^{-3} respectively.[66] Clear *p*-type characteristics can be observed for both 0.2% and 1% Sb-doped ZnO NW-FETs. The on/off ratio, threshold voltage, mobility and carrier concentration of 0.2% doped sample are found to be 10^5, 2.1 V, 0.82 $cm^2 \cdot V^{-1} \cdot s^{-1}$ and 2.6×10^{17} cm^{-3} respectively, while the corresponding values for 1% doped samples are 10^4, 2.0 V, 1.24 $cm^2 \cdot V^{-1} \cdot s^{-1}$ and 3.8×10^{17} cm^{-3}. The electrical transport characteristic of the 0.2% doped sample was remeasured after 2 months, confirming stable *p*-type behavior.

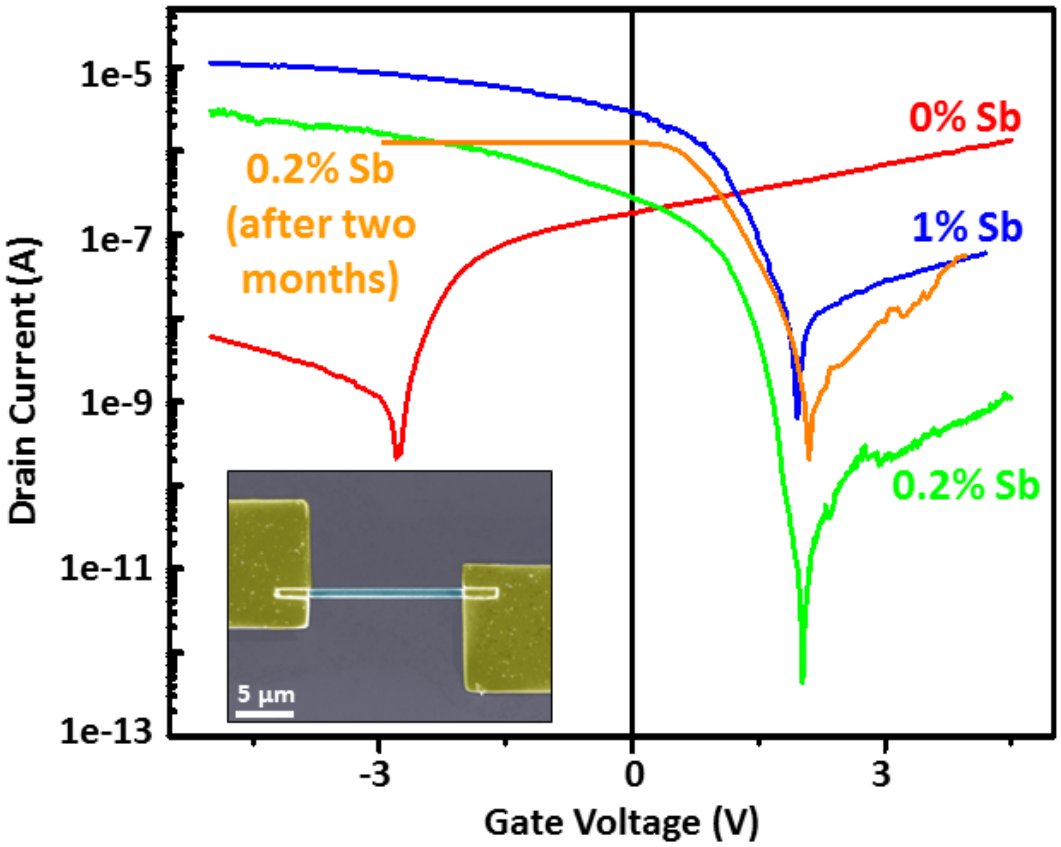

Figure 8 Single wire FET measurements of undoped and Sb doped nanowires. A back gate was used to apply the gate voltage. Inset shows as a false color SEM image of the experimental setup for a single wire. The 0.2% doped sample was remeasured after two months, showing stable *p*-type behavior.[46]

3.5 AFM Characterization

Previous reports have demonstrated that the majority charge carrier of doped piezoelectric semiconductor NWs can also be identified by measuring the piezoelectric response via conductive atomic force microscopy (AFM).[55, 68] In our experiment, a Pt-coated Si AFM tip (AFM: MFP-3D from Asylum Research) was scanned across an array of as-grown NWs in contact mode with a constant normal force of 5 nN. A 500 MΩ resistor was added to the circuit to calculate the voltage based on the output current. Consistent with previous literature, electrical signals with opposite polarities were observed in undoped and doped wires (Figure 9a-c). The resulting average and maximum output

voltage is summarized in Table 1. When the AFM tip bends a piezoelectric semiconductor NW, positive and negative piezopotential are induced along the stretched and compressed sides, respectively. In an *n*-type NW, the conduction band electrons tend to accumulate on the stretched side. Consequently, the positive piezopotential at the stretched side is partially screened by free charge carriers while the negative piezopotential is preserved. The remnant positive piezopotential due to incomplete screening by the free electrons results in a reversely-biased Schottky barrier between AFM tip and NW, which prevents the flow of electrons across the interface. When the AFM tip scans across the top of the NWs and touches the compressed side of the NW, negative piezopotential at that side gives rise to the forward-biased Schottky barrier. As a result, negative transient current spikes can be observed in external load due to the transport of free electrons from the semiconductor to the metal tip (Figure 9d left).[33] Conversely, in NWs with finite *p*-type doping, the holes tend to accumulate at the negative piezopotential side. In this case, the negative piezopotential at the compressed side is partially screened while the positive piezopotential is preserved. Unlike *n*-type semiconductors, the Schottky barrier at the metal/*p*-type semiconductor interface is forward-biased when the semiconductor side is positively-biased (Figure 9d right).[6] Therefore, positive piezopotential in bent *p*-type NWs will drive the flow of charge carriers from the metal tip to the NWs through the external load and positive transient current spikes can be observed. As a result, one can easily identify the majority carrier based on the sign of measured current during conductive AFM scanning. It is also interesting to note that the outputs from 1% doped NWs (Figure 9c) were an order of magnitude lower than those from the 0.2% doped samples, which can be attributed to the increased screening of strain-induced piezopotential in more heavily doped NWs.[34] By

characterizing the electrical transport and piezoelectric response measurements, the *p*-type doping of our ultra-long NWs was confirmed.

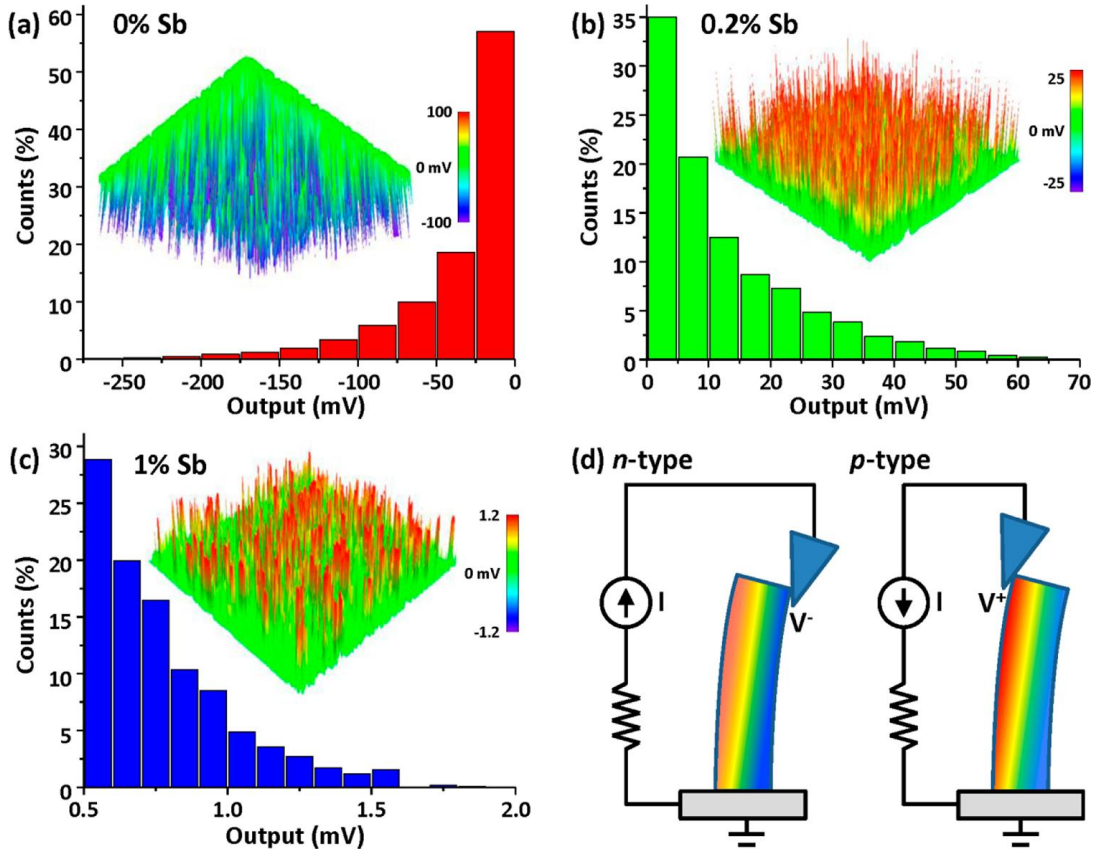

Figure 9 Conductive AFM measurements of the piezoelectric outputs of (a) 0, (b) 0.2, and (c) 1% Sb doped NWs. A histogram of the percent of peaks observed for each output range is plotted. (d) Schematic demonstrating the difference in screening of piezo-polarization charges, and the opposite polarity of piezoelectric outputs between transversely bent *n*- and *p*-type nanowires. Color gradient represents the distribution of piezopotential, with red indicating positive piezopotential and blue negative piezopotential.[46]

Table 1 Dependence of the output of a piezoelectric nanogenerator on Sb doping in *p*-type ZnO nanowires

Sb Doping (%)	Average Output (mV)	Maximum Output (mV)
0	-36.2	-482.1
0.2	12.9	73.2
1	0.77	1.83

The first antimony doped sample I tested was on April 22, 2012. A 2% doping level was used, and an average output of 16.2 mV. The same sample was kept in a desiccator since the initial measurement, and was remeasured on January 27, 2015, almost 3 years

later. The output was still positive, with a slightly lower output of 15.8 mV, showing that after all this time, the *p*-type doping was preserved. This is almost twice as long as the 18 months previously demonstrated by Yankovich et al. suggesting that Sb is a stable dopant which could see commercial viability. There is a noticeably higher level background signal, which can be attributed to a difference in scan area between the two samples, and the buildup of contamination while the device was in storage. While this method is a good simple method of checking the existence of doping, it is difficult to say whether the exact doping level has remained the same or if there have been some changes to the material as it has aged.

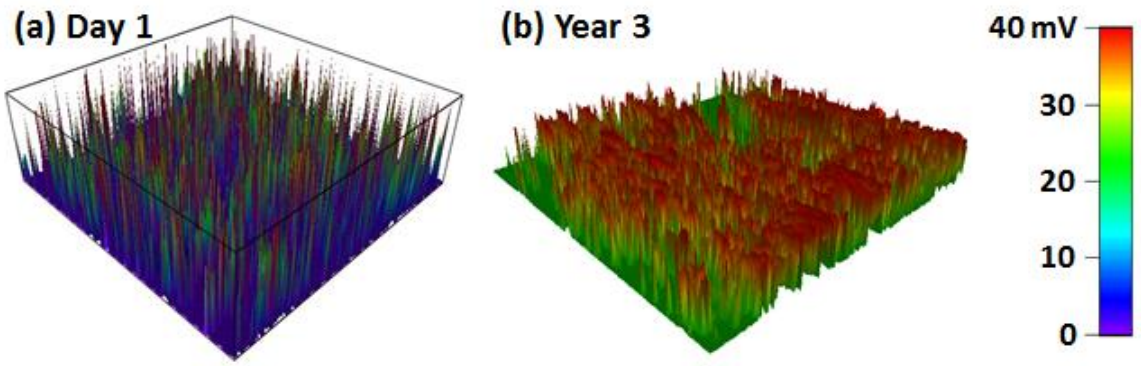

Figure 10 (a) Conductive AFM measurement of the output voltage of the first antimony doped ZnO grown. (b) AFM measurement of the same sample almost 3 years later, with the same signal polarity.

3.6 Piezotronic Characterization

To prepare samples for piezotronic measurements, as-synthesized Sb-doped ZnO NWs were sonicated in ethanol and transferred onto PET substrates. Titanium (200 nm thick) was chosen to form Schottky contacts with single *p*-type ZnO NWs. *I-V* characteristics of the as-fabricated two-terminal device was subsequently obtained when the device was subject to different strains and corresponding results shown in Figure 11a indicate that transport properties of the devices can be modulated by the applied mechanical

strain. The nanowire was attached laterally to a substrate, and its two ends bonded with metal. In such a configuration, since the diameters of *p*-type ZnO NWs (< 1 μm) is significantly smaller than the thickness of the PET substrates (~500 μm), strain induced in the *p*-type ZnO NWs is dictated by the substrate. Strain values in a single NW are calculated according to previous studies with tensile strain defined as positive and compressive strain defined as negative.[86] The polarity of the applied bias is with respect to drain electrode. For positive drain bias, the current through the device increased under tensile strain, and decreased with compressive strain (Figure 9a). Conversely, under negative drain bias, the opposite trend was observed, with the current increasing under compressive strain, and decreasing with increased tension. The "gating" effect of external strain on charge carrier transport in *p*-type ZnO NW piezotronic devices is demonstrated more explicitly in the inset of Figure 11a. Current values (*I*) in a device under various strains were measured at fixed bias (0.8 V and -0.8 V here). The corresponding strain-induced change in Schottky barrier height (SBH) was calculated and plotted in Figure 11a inset,[86] demonstrating a change of 53 meV in SBH at drain contact with an applied compressive strain of 0.68%. The band diagrams of *p*-type ZnO NW piezotronic device are shown in Figure 11b-d to better explain the underlying working mechanism. Band diagrams shown here are for positive drain bias, and corresponding diagrams can be obtained for negative drain bias. The Schottky barrier at the metal/*p*-type semiconductor interface causes the band structure to bend downwards. The transport properties of the device are dictated by the reversely biased contact due to its large voltage drop and are sensitive to changes in its SBH. For the case of positive drain bias (Figure 11b-d), the drain contact is reversely biased, so $\Delta\Phi_d$ dictates the charge carrier transport. When the device is

biased by an external power source, the quasi-Fermi levels at both contacts are separated, resulting in the band diagram shown in Figure 11b. When tensile strain is applied to the device, due to the orientation of the *c*-axis of the *p*-type NW, negative piezoelectric polarization charges are induced at the drain contact (Figure 11c). If the doping level inside the NW is finite, these immobile ionic charges will only be partially screened and can attract the majority charge carriers, holes, towards the metal-semiconductor interface, which decreases the SBH at the drain contact ($F'_d < F_d$), as shown in Figure 11c. At the same time, positive piezoelectric polarization charges are induced at the source contact, which results in an increased SBH at the source contact ($F'_s > F_s$). When compressive strain is applied to the device, on the other hand, positive piezoelectric polarization charges are induced at the drain contact (Figure 11d), which depletes holes near the metal-semiconductor interface and increases the SBH at drain contact ($F''_d > F_d$). Simultaneously, negative piezoelectric polarization charges are induced at source contact, lowering the SBH at source contact ($F''_s < F_s$). This leads to the observed *I*-*V* curves shown in Figure 11a, in which the applied mechanical strain functions as the controlling *gate* signal to modulate the carrier transport in *p*-type ZnO NWs based piezotronic transistors, the core concept of piezotronics.[12, 13]

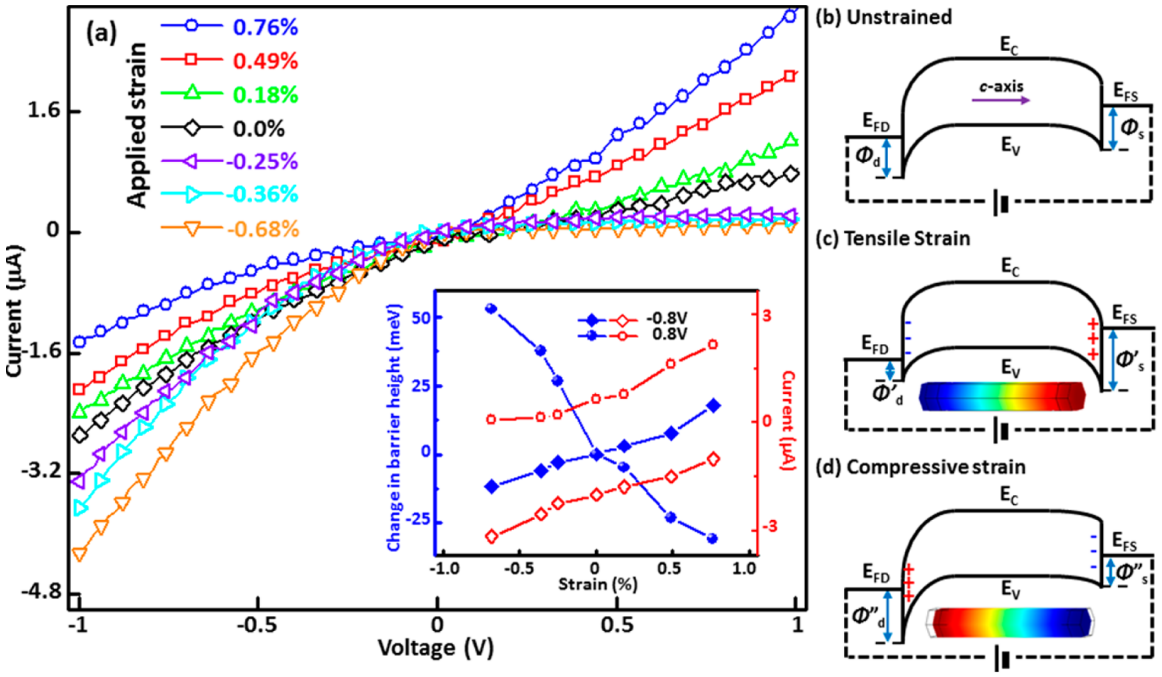

Figure 11 Demonstration of the piezotronic effect in *p*-type ZnO nanowires. (a) I-V curves show a modulation in current as a result of strain. (b)-(d) Schematic illustration of the change in band structure as a function of applied strain.[46]

3.7 Nanogenerator Performance

The piezoelectric-polarization-induced piezopotential in strained *p*-type ZnO NWs can also drive the flow of electrons through an external load without an applied electric bias, which can be utilized to harvest mechanical energy and converts it into electricity. Flexible piezoelectric nanogenerators (NGs) based on an array of *p*-type ZnO NWs were fabricated to demonstrate this concept (Figure 12). A layer of ITO was first sputtered onto PET substrates serving as the bottom electrode. A ZnO seed layer was subsequently sputtered onto the ITO layer. An array of *p*-type ZnO NWs was then grown through the hydrothermal method described previously, except the growth time was decreased to 2 hours for the 0 and 0.2% doped samples to produce wires of comparable length to the 1% doped samples. After growth, the as-synthesized NWs array was encapsulated with a polymethyl methacrylate (PMMA) layer and a layer of gold was evaporated onto the baked

PMMA to serve as the top electrode. Piezoelectric output was produced by applying periodic mechanical strain to the device. Due to the low doping concentration, no significant difference can be seen between the outputs of the 0 and 0.2% doped devices (~3.2V). However, there was a noticeable drop in output for the 1% doped sample (~1.7V). This can be attributed to the more significant screening of the induced piezo-polarization charges by the higher concentration of free charge carriers. Unlike the aforementioned AFM measurements for transversely bent ZnO NWs, no reversal in polarity of the outputs were observed here for *n*- and *p*-type samples due to the fundamental differences between these two scenarios. Because of the device structure and operation scheme of the flexible array NG, the strain induced piezopotential is distributed along the axial direction of the NWs, regardless of doping, which is different from the transverse distribution of piezopotential in the AFM study. The distribution of piezopotential induced along the NWs is dictated by the crystal structure and orientation, and not the type of majority carriers. As a result, the piezopotential of both undoped and doped samples will have the same polarity at corresponding contacts under the same straining conditions. Free electrons in undoped samples and holes in doped ones will only screen the piezopotential at their corresponding contacts, and will not change the direction of the electron flow through the external circuit, which defines the polarity of the measured electrical outputs.

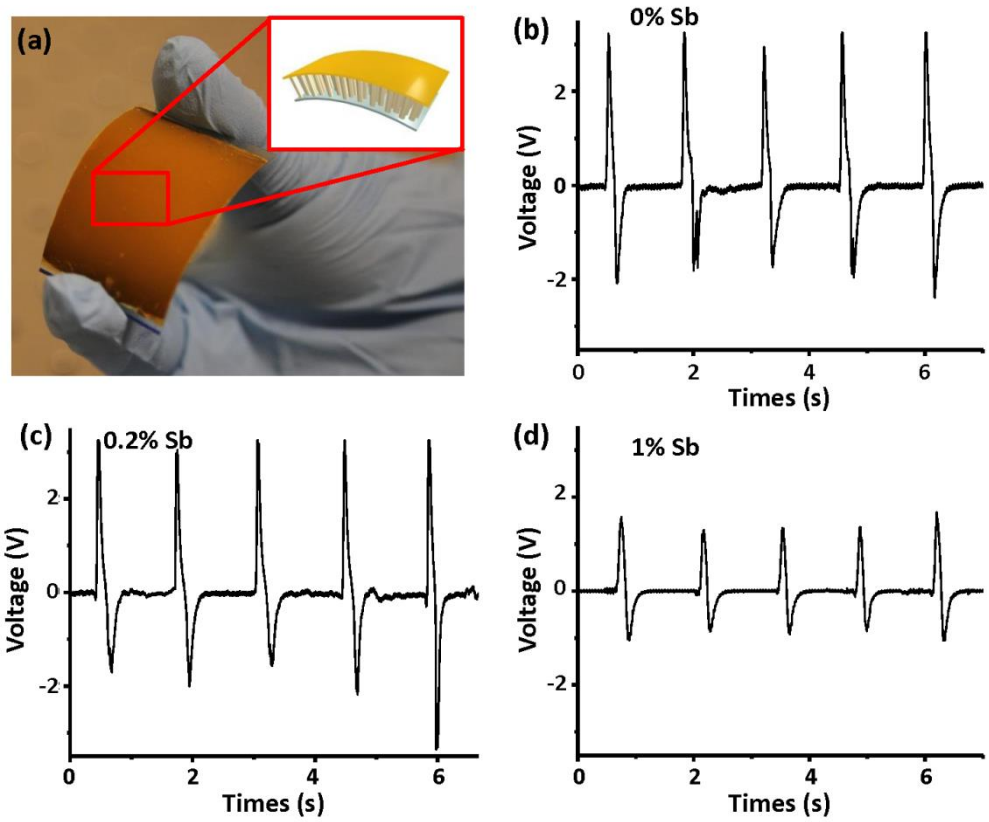

Figure 12 Flexible nanogenerators fabricated using *p*-type ZnO NWs array with different doping levels. (a) Photograph of the bent device to show its flexibility. A schematic of the device is shown in the inset. (b)-(d) Nanogenerator output as a function of doping level. The growth time was tuned so that all 3 samples would have similar wire length.[46]

3.8 Conclusion

In conclusion, using a modified solution grown method, I was able to produce ultra-long *p*-type ZnO wires with dimensions large enough for manipulation/integration into practical devices. I further investigated the universality of piezotronic effect in Sb-doped *p*-type ZnO NWs films and reported, for the first time, strain-gated piezotronic transistors as well as piezopotential-driven mechanical energy harvesting based on solution-grown *p*-type ZnO NWs. Investigating the piezotronic effect in *p*-type piezoelectric semiconductor is critical for developing a more sophisticated piezotronic theory and designing/fabricating novel piezotronic applications with more complex functionality. The results presented here broaden the scope of piezotronics and

extend the framework for its potential applications in electronics, optoelectronics, smart MEMS/NEMS and human-machine interfacing.

CHAPTER 4: HOMOJUNCTIONS FOR ENHANCED NANOGENERATORS

4.1 Introduction

Since the concept of the nanogenerator (NG) was first introduced, zinc oxide (ZnO) nanomaterials have served as the model system for studying and applying mechanical energy harvesting in micro/nano-scale systems. Over the years, as the understanding of the fundamental principles has improved, piezoelectric NG technology has advanced significantly, presenting their potential as practical miniaturized power sources[1]. One method to enhance the piezoelectric output in ZnO nanowire NG is through the formation of a *p*-*n* junction.[70, 71] As ZnO is intrinsically *n*-type doped, by coating an array of ZnO nanowires (NWs) with a *p*-type conducting polymer, such as poly(3-hexylthiophene-2,5-diyl) (P3HT), a *p*-*n* junction could be formed. Because the polymer attracts free electrons from ZnO, the screening of piezoelectric polarization inside ZnO NWs by free-carriers is reduced, which improves the performance compared to the junction-less device.

Although considerable enhancement has been achieved in these *p*-*n* heterojunction devices, it would be advantageous to use *p*-type ZnO instead to form a homojunction due to the improved chemical stability and mechanical durability between the two ZnO layers. Moreover, the matched band alignment and semiconductor properties between the single-crystalline *p*-ZnO and *n*-ZnO NWs may enable interesting applications in functional electronics and optoelectronics. In this section of my thesis, I will demonstrate the synthesis of ZnO nanowire film based homojunctions and its ability to enhance the performance of piezoelectric nanogenerators.[87] After characterizing the materials and its electrical

properties, the effect of the *p*-*n* junction and plasma treatment on its NG output will be demonstrated. Finally, using the optimum architecture, homojunction based nanogenerators were grown on silicone substrates for applications in gesture detection.

4.2 Synthesis and Microscopy

ZnO *p*-*n* homojunctions were obtained using a hydrothermal method[44] modified with sodium citrate. To produce the *n*-type layers, a solution of 25 mM zinc nitrate, 12.5 mM of hexamethylentetramine (HMTA), and 0.7 mM sodium citrate was made in water. 0.5 M of ammonium hydroxide was added to the solution to inhibit self-nucleation and precipitation in solution. The substrate was floated face down on the water surface, and left to react in an oven at 75°C for 30 minutes. To grow *p*-type ZnO, the precursor concentration and growth time were both doubled in order to compensate for the dopant's interference with normal ZnO growth. A doping level of 1% Sb relative to Zn was chosen, and 0.5 mM of Sb glycolate dopant was added to the solution. The same amount of ammonium hydroxide was added to this solution. As citrate ions binds preferentially to the (0001) surface of ZnO, growth in the axial direction is inhibited, thus promoting radial growth[40] and causing the NWs to expand and finally coalesce into a densely packed nanowire-film (Figure 13). To prepare the multilayer films, the substrate was put into a fresh solution for continued growth after growing the first layer. As such, I was able to grow both homogeneous and heterogeneous structures (Figure 13a-d) with a controllable thickness of ~1.5 μm per layer.

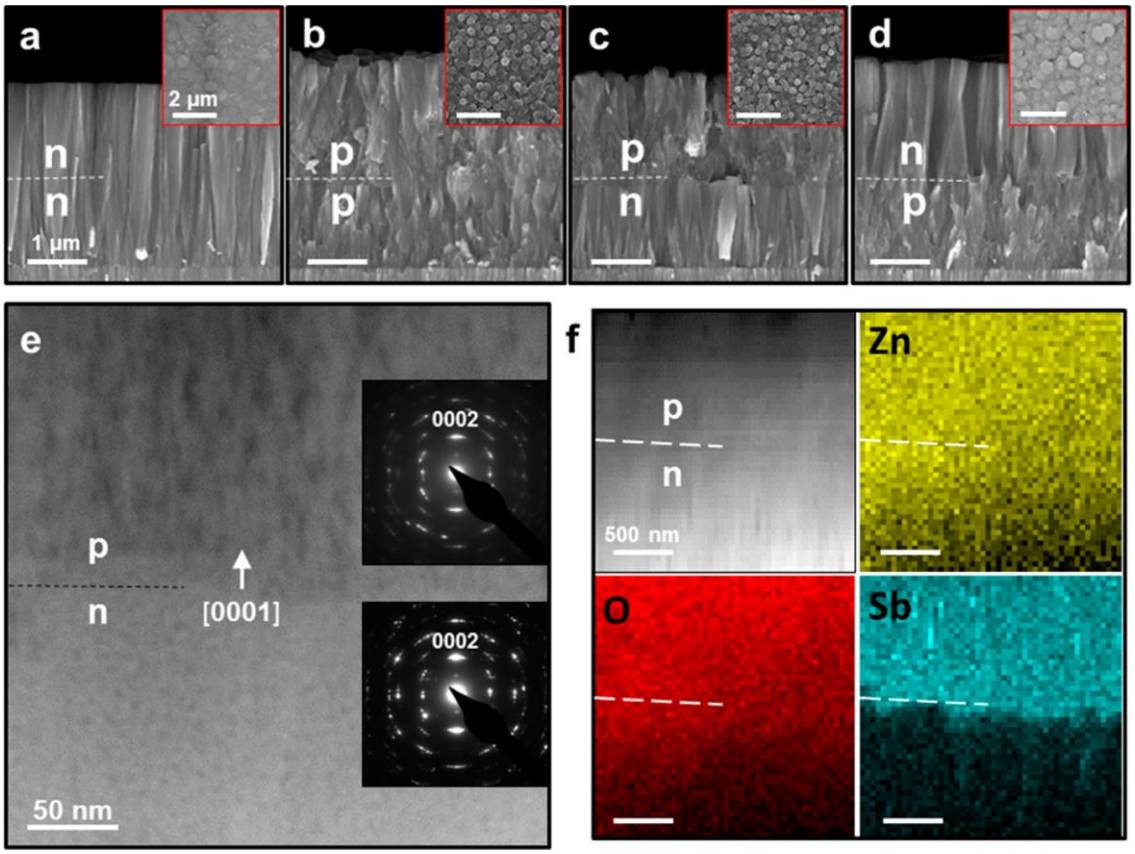

Figure 13 (a-d) Homogeneous and homojunction bilayer films grown through citrate modified hydrothermal method. The inset shows a top view of the sample. (e) STEM image of the interface between the n and *p*-type layers in the np sample. The insets give the electron diffraction patterns of each layer. (f) EDX scan of the interface, and the elemental distribution of Zn, O, and Sb in the n and *p*-type layers.[87]

Samples will be referred to in the order in which the layers were grown, i.e. **np** indicates the first layer grown is undoped (*n*-type) and the second one grown is *p*-type doped. From the cross sectional view, the undoped **nn** sample (Figure 13a) has a smooth and continuous growth with an even top surface. On the other hand, the growth for the **pp** sample (Figure 13b) is much less uniform due to the incorporation of the Sb dopant, producing variation in wire length of about 100 nm, which translates to surface roughness (Figure 13b inset). In the **np** and **pn** films (Figure 13c, d), differences in morphology of the doped and undoped films is clearly visible, and a clean interface showing where one growth stopped and the other started. The top view of the **np** film (Figure 13c) shows a

surface roughness comparable with the **pp** sample. From the top view of the **pn** film (Figure 13d), it appears that the top surface is not as uniform as its **nn** counterpart. The roughness from the underlying *p*-type layer translated to the *n*-type growth, producing the observed roughness. The modified hydrothermal method presented here is versatile and stable enough that multilayer samples with alternating layers of doped and undoped films can be produced (Figure 14), making solution-derived ZnO multi-junction structures possible for flexible electronics and optoelectronics.[15]

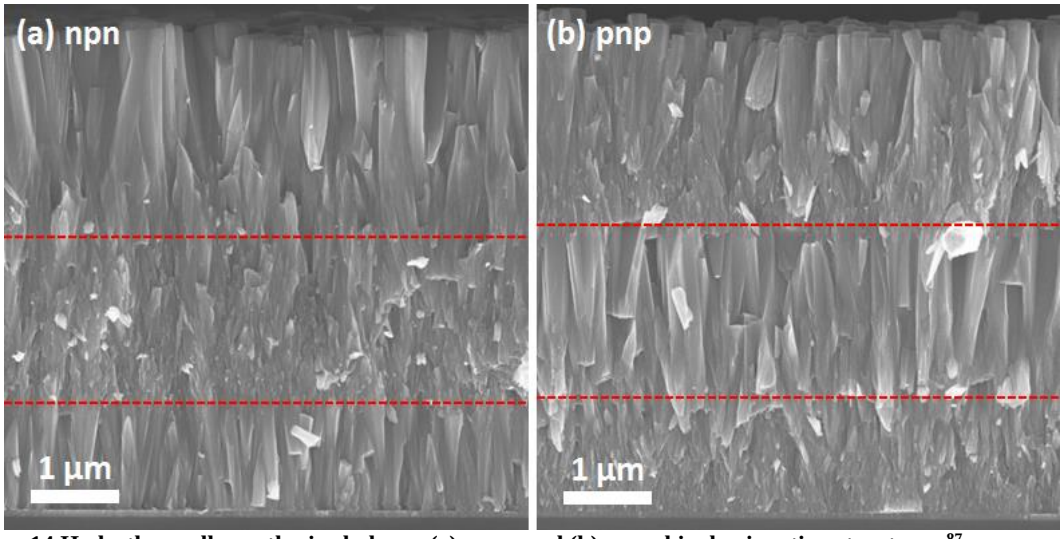

Figure 14 Hydrothermally synthesized planar (a) *n-p-n* and (b) *p-n-p* bipolar junction structures.[87]

To verify the incorporation of Sb dopant into the films, a cross-section of the **np** sample was analyzed using scanning transmission electron microscopy (STEM). At the interface (Figure 13e), a clear difference in microstructure between the undoped and doped regions can be observed. In the doped region, dark voids formed due to the incorporation of Sb atoms during growth, as demonstrated in previous studies.[46, 67] When Sb is incorporated into the ZnO lattice during growth, it forms atomic planes perpendicular to the growth direction that interfere with ZnO NWs growth. Because of this, ZnO continues to grow around the dopant, forming the observed voids in the NWs. On the other hand, the

undoped region at the bottom is brighter and more uniform due to the absence of internal defects. The light pitting observed in undoped region is due to the use of ion milling to thin the sample for analysis. Selected area electron diffraction (SAED) patterns were taken from each region, and both had nearly identical patterns, showing that the *c*-axes for both layers are aligned in the same direction (Figure 1e). To further verify the presence of Sb, energy-dispersive X-ray (EDX) mapping was performed at the interface between the two layers (Figure 13f). The Zn and O signals are uniformly distributed throughout the scanned region. The slightly lower signal in the bottom right is due to differences in sample thickness. A significantly stronger Sb signal is observed in the top half of the image, showing that the dopant was only present in the doped region. From the quantitative analysis through an EDX point scan taken on the *p*-type region (Figure 15), it was determined that the atomic percentage of Sb was 1.5% (Table 2), despite the concentration of dopant added to the solution was only 1%. This may be understood as follows. When Sb ions incorporate into the ZnO during NW growth, they cluster together into single-atomic planes.[26] Because subsequent layers of Zn and O cannot attach themselves to the Sb plane, growth simply continues around it, producing the aforementioned voids. Due to the addition of citrate, the growth rate of ZnO in the axial direction slows down, so there is more time for Sb to incorporate itself into the NWs. Additionally, there is always material consumed because of homogeneous nucleation in solution, so not all of the Zn source added to the solution could be incorporated into the as-synthesized sample itself, which may also explain this discrepancy in concentration.

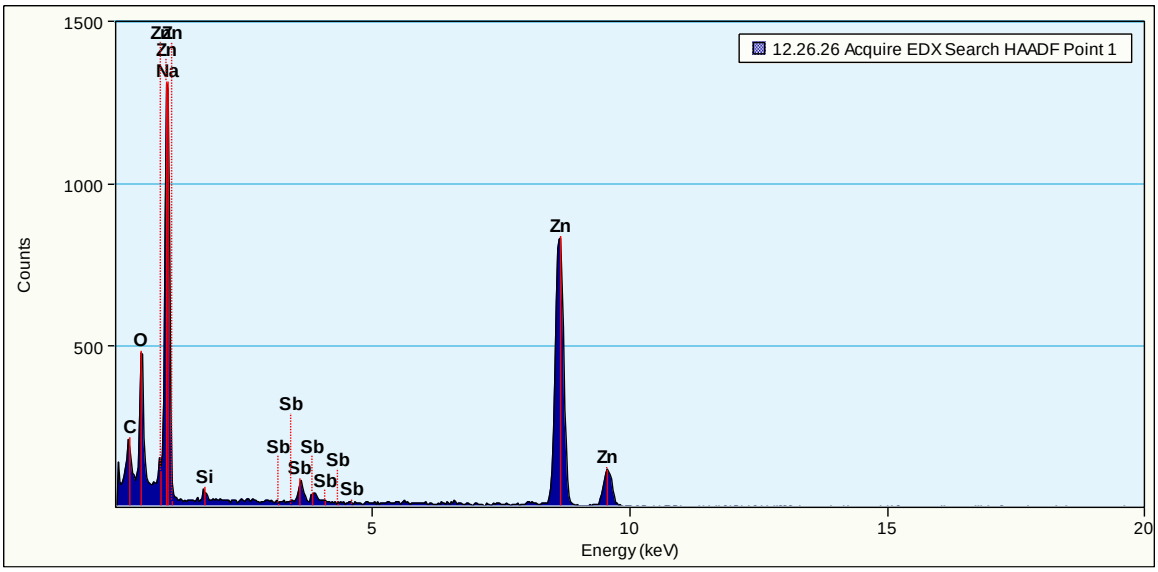

Figure 15 EDX scan of *p*-type layer in the np homojunction structure[87]

Table 2 Atomic and weight percentages of Zn, O, and Sb in the *p*-type layer derived from EDX.

Element	Weight %	Atomic %
O (K)	19.73	50.76
Zn (K)	75.80	47.72
Sb (L)	4.45	1.50

4.3 Electrical Characterization

Electrical measurements were performed to further verify the formation of *p-n* junction through the above process. A transparent conducting oxide (aluminum doped zinc oxide (AZO)) was chosen as electrode material to form both top and bottom electrical contacts with as-synthesized films in all samples. Electrical measurements were performed on a Keithley 4200 semiconductor parameter analyzer. From the two-terminal *I-V* measurements, clear linear behaviors are observed for both doped and undoped NW samples, suggesting that AZO forms good Ohmic contacts with both *n*- and *p*-ZnO NWs (Figure 16a, b). **pn** and **np** films were grown and measured in a similar fashion. When

performing all measurements, the top layer was under positive bias for consistency. Strong rectification behavior is observed for both the **np** and **pn** samples, with a turn-on voltage of about 1 V for **np** sample and negative turn-on voltage of -0.5 V for **pn** sample (Figure 16c). A slightly higher leakage current is observed for the **np** sample compared to the **pn** one. Because the *p*-type wires naturally grow less evenly, the top surface of the **np** sample will be rougher, compared to the **pn** sample (Figure 13c,d). This can lead to a poorer electrical contact in the **np** sample, and thus a higher leakage current. These results confirm the successful formation of *p*-*n* homojunction regardless of the order in which the *n*- or *p*-layers were grown first.

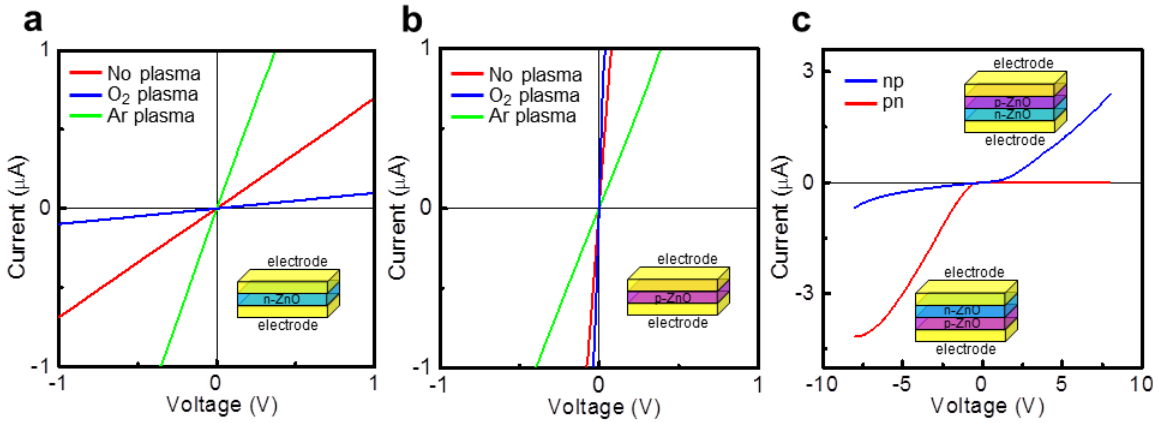

Figure 16 IV curves of (a) *n*-type and (b) *p*-type ZnO nanowire films treated with oxygen and argon plasma. (c) IV characteristics of homojunction structures grown in both np and pn orders. In both cases, the top electrode is under positive bias.[87]

Table 3 Resistance of single ZnO nanowire films before and after O_2 or Ar plasma treatment (MΩ).

	n-type	*p*-type
No plasma	1.44	0.07
O_2 plasma	10.1	0.03
Ar plasma	0.36	0.40

The effect of plasma treatment on the transport behavior of these samples was also investigated. Plasma treatment was performed in a Plasma-Therm reactive ion etcher. For O_2 plasma, a pressure of 300 mTorr, flow rate of 20 sccm, RF power of 200 W, and time of 20 minutes was used. For Ar plasma treatment, these values were 250 mTorr, 60 sccm, 50 W, and 30 minutes, respectively. Previous work has shown that treating *n*-type ZnO with oxygen or argon plasma can modulate its carrier concentration, and thus its piezoelectric properties.[88] As the free charge carriers in the nanowire are primarily responsible for the screening of the piezopotential, a more insulating material should have a stronger piezoelectric output. A baseline resistance of 1.44 MΩ for as-synthesized *n*-type ZnO was found. When treated with O_2 plasma, the resistance of *n*-type ZnO increased to 10.1 MΩ, while it decreased to 0.36 MΩ after treatment with Ar plasma (Figure 16a). These results are consistent with the widely-observed dependence of the electrical conductivity of *n*-type ZnO on the oxygen partial pressure. The exact origin of *n*-type conductivity in ZnO has been the subject of controversy, and various sources such as a metastable oxygen vacancy configuration,[53] oxygen vacancies stabilized with zinc interstitials[52] and multicoordinated hydrogen[51] have been proposed to contribute to the unintentional *n*-type conductivity of ZnO. For *p*-type ZnO, an opposite trend was observed (Figure 16b). Starting from a baseline resistance of 0.07 MΩ for as-synthesized *p*-ZnO, when treated with O_2 plasma, the resistance decreased to 0.04 MΩ, while it increased to 0.40 MΩ under Ar plasma. This is likely to be due to the formation or removal of compensating donor defects. As with the undoped *n*-type sample, the above mentioned donor sources are removed in *p*-ZnO under O_2 plasma. Rather than making the material more insulating as is in the *n*-type sample, this makes *p*-ZnO more conductive since the relative concentration

of free holes increases (blue curve in Figure 16b). The same is true for Ar plasma treatment. As more donor sources are produced, the depletion of free holes makes the material more insulating (green curve in Figure 16b). The changes in resistivity are summarized in Table 3.

4.4 Homojunction Nanogenerator

In order to determine the effect of homojunction on the piezoelectric output, different architectures were grown and the outputs were measured under consistent deformation (Appendix B). Stacked layers were grown on 2x2 cm flexible polyethylene terephthalate (PET) substrates with a commercially deposited layer of indium tin oxide (ITO) (R_S=60 Ω/sq) as a bottom electrode. The as-grown structure was then spin coated with PMMA A6 at 2000 RPM to form an insulating layer to prevent current leakage. AZO was sputtered on top of the whole structure as the top electrode, and test wires were affixed to the two electrodes using conductive silver paste. Finally, the whole structure was coated with a layer of polydimethylsiloxane (PDMS) as a packaging layer, producing a complete energy harvester. The resulting structure is shown both pictorially and schematically in Figure 17a. Single layers of *n* and *p*-type ZnO were used as the baseline for piezoelectric measurements (Figure 17b, c). In the experiment, compressive strain of -0.22% (Calculation shown in Appendix B) was periodically induced in the NW film by deforming the PET substrate. Since the polar axis (red arrow in Figure 17a) points away from the substrate in both the *n*- and *p*-ZnO NW films as confirmed in Figure 13e, negative/positive piezoelectric polarization charges ("-" and "+") are induced at the top/bottom of the films under compressive strain. The negative polarization charges can drive electrons through an

external circuit to screen the positive polarization charges at the bottom of the film and balance out the difference between quasi-Fermi levels at the top and bottom electrodes. This gives rise to the positive pulse observed in experiment. The response time of these devices can be measured by measuring the time from zero output to the peak. From this, a response time of 40 ms was measured (Figure 18), which is on a similar order of magnitude as previous studies on ZnO nanowires.[86, 89] When the strain is released, the piezoelectric polarization disappears, and the electrons that had once screened the positive polarization charges flow back through the external circuit and produce the negative pulse. Both kinds of NW films also experience internal screening of piezoelectric polarization by free carriers. The "e" and "h" symbols represent negative and positive free carriers in *n* and *p*-ZnO, respectively (Figure 17). The average output voltages of the as-synthesized *n*- and *p*-type samples were 7.10 and 7.13 mV respectively (Figure 17b, c).

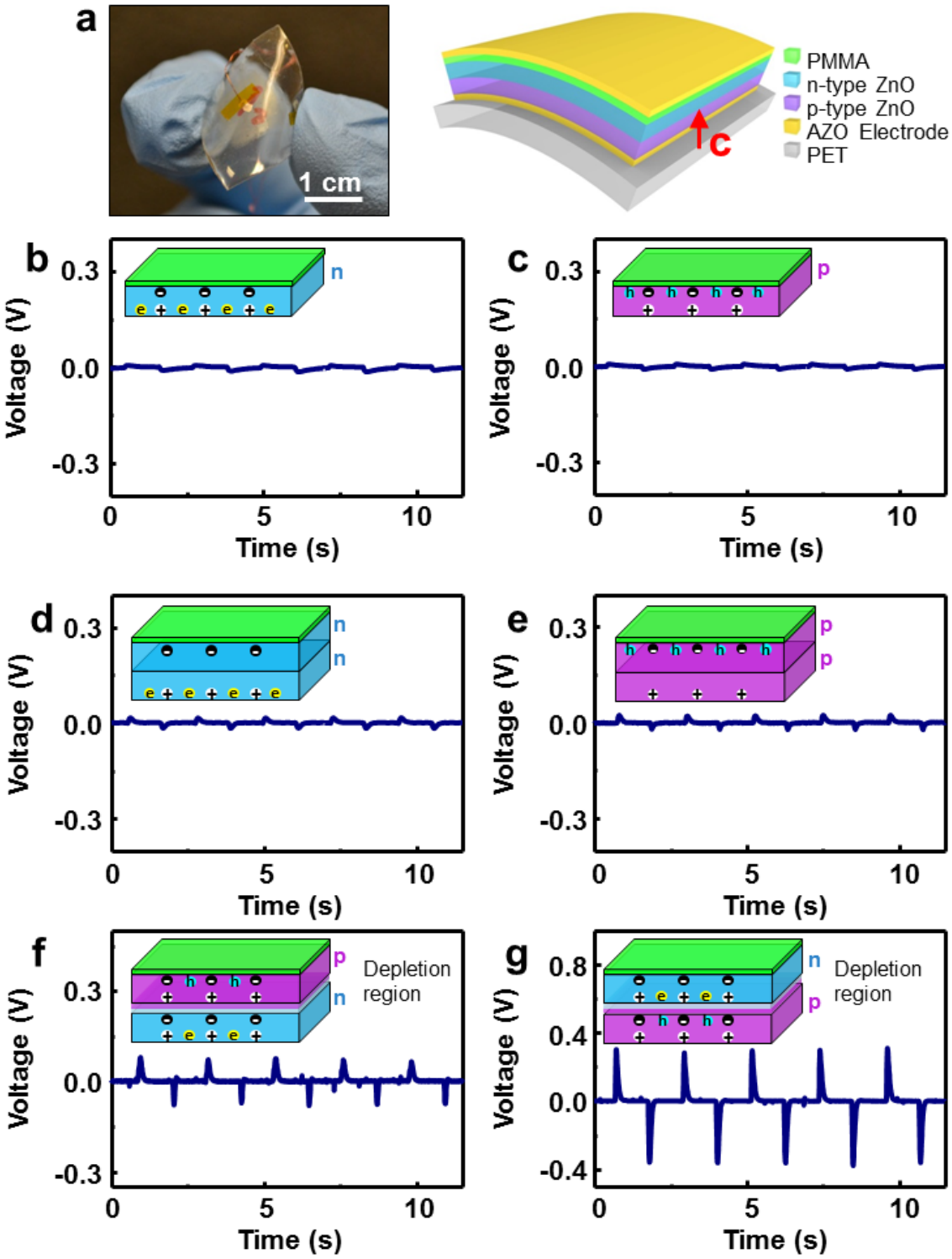

Figure 17 (a) Photograph and schematic representation of homojunction nanogenerators fabricated on PET substrates. Component thicknesses are exaggerated for clarity. Nanogenerator outputs for single layer (b) n abd (c) *p*-type samples. Double layer, single component (d) nn and (e) pp samples have roughly twice the output of their single layer counterparts. Forming (f) np or (g) pn homojunction nanogenerators leads to a significant improvement due to reduction in free charge carrier concentration by the depletion region.[87]

The piezoelectric output of bilayer structures was measured to see how adding a homojunction changes the output. To start, bilayer structures with single conductivity type was measured, and an average output of 13.9 and 24.2 mV was observed for the **nn** and **pp** structures, respectively (Figure 17d, e). This output makes sense with respect to the single layer samples (Figure 17b, c), as bilayer structures possess twice the thickness of the piezoelectric layers. This is analogous to connecting two single layer devices in series, which in principle doubles the output voltage. When an **np** nanogenerator is made, a noticeably higher output is observed (150 mV) compared to the single component bilayer structure (Figure 17f). Because of the formation of the depletion region, the free charge carrier concentration in each layer is reduced, although there is still some amount of screening. Therefore a significant improvement in the output can be observed compared to that of the bilayer structures with single conduction type. For the **pn** structure, the output increased by over an order of magnitude to 284 mV compared to the **nn** and **pp** samples. In this case, the free electrons and holes remaining in the *n* and *p*-type layers after the formation of the depletion region are attracted to the junction area to screen the respective piezo-polarization charges (Figure 17g). As a result, the piezo-charges at the electrodes are essentially unscreened, leading to a great improvement in the piezoelectric output. The corresponding output currents are shown in Appendix C, and summarized in Table 4, and the same trends are observed as a result of changes in screening.

The hydrothermal method is naturally prone to some variability in nanowire dimensions and doping which can affect the resulting nanogenerators piezoelectric output. Previous work on *p*-type ZnO nanowires[46] showed that increasing the doping level reduced the nanogenerator output, due to increased screening, so fluctuations in doping between

samples could affect the output. Fluctuations in wire dimensions can also have an effect on output, as the piezopotential is governed by the nanowire aspect ratio.[90] Based on the SEM images in Figure 13, I conclude that nanowire growth within a single sample is not variable enough to warrant concern. Compared to early studies of piezoelectric nanogenerators[38] with output voltage on the order of 80 mV, the output obtained in the **pn** structure is significantly improved. With optimized design and packaging, ZnO based nanogenerators with output on the order of tens of volts could be obtained.[39] By comparison, the structure presented in this work is relatively simple in order to emphasize the study of the fundamental materials system.

Table 4 Average output current and voltage of homojunction structures not subject to plasma treatment

Configuration	Voltage (mV)	Current (nA)
n	7.10	1.66
p	7.13	0.56
nn	13.9	0.473
pp	24.2	0.246
np	150	0.985
pn	284	10.6

To quantify the power output of the piezoelectric device, it is necessary to study the voltage and current outputs as a function of load resistance, as shown in Appendix C. The power output of the weakest and strongest devices, **n** and **pn**, were compared. In both cases, the output current is constant for load resistance up to ~10 MΩ, and then falls with increasing load, while the output voltage increases when the resistance exceeds 10 MΩ and tapers off around 2 GΩ. The maximum instantaneous power delivered onto the load for the

n device of 1.1 pW occurs when load resistance is 110 MΩ, and a largely enhanced power output of 232 pW for **pn** device is achieved when load resistance is 22 MΩ.

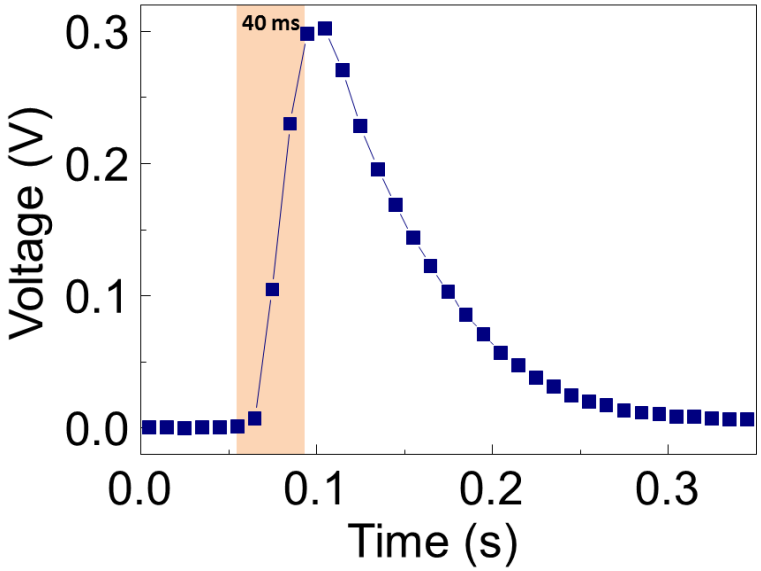

Figure 18 Zoomed in view of a single output peak from the pn device to demonstrate the response time.[87]

The change in output when the structures described earlier were treated with O_2 or Ar plasma was investigated. As demonstrated earlier in Figure 16, with the appropriate plasma treatment, the free charge carrier concentration in both *n*- and *p*-ZnO can be reduced, which mitigates the screening of piezoelectric polarization and thus improves the piezoelectric output for the single layer device. Single layer devices were fabricated, and treated with the appropriate plasma to increase the output voltage ($\mathbf{n_{O2}}$ & $\mathbf{p_{Ar}}$). The output increased by an order of magnitude when compared to the **n** and **p** samples from Figure 17, to 55.3 and 66.9 mV, for $\mathbf{n_{O2}}$ and $\mathbf{p_{Ar}}$, respectively (Figure 19 a, b).

Because the same plasma treatment has opposite effects depending on whether the material is *n*- or *p*-type, treating a homojunction structure with the same plasma will make one layer more insulating, and thus more piezoelectric, while making the other layer more conductive, and less piezoelectric. Based on this, I investigated the effect of ZnO *p*-*n*

homojunction on piezoelectric NG outputs when only one layer in the homojunction structure is piezoelectric while the other is more conducting. The first group of samples includes the **np** structure (Figure 19 c, d). In an O_2 plasma treated **np** structure ($\mathbf{n_{O2}p_{O2}}$), the bottom *n*-type layer becomes more insulating, and thus more piezoelectric, while the top *p*-type layer is more conducting, thus making its contribution to output negligible when compared to their as-synthesized counterparts (Figure 19c). Under compressive strain, the positive piezoelectric polarization charges in the $\mathbf{n_{O2}}$ layer should experience even less internal screening as there is a lower concentration of free electrons because of the formation of the depletion region. However, the output is only 7 mV, much weaker than the $\mathbf{n_{O2}}$ sample (Figure 19a). This is because the thick conducting $\mathbf{p_{O2}}$ layer is dampening the effect of the negative piezoelectric polarization charges induced near the top surface of the bottom *n*-type layer. Similarly, for the Ar plasma treated **np** structure ($\mathbf{n_{Ar}p_{Ar}}$), a reduced output (12.2 mV) compared to the $\mathbf{p_{Ar}}$ sample is observed (Figure 19d). Here, the bottom *n*-type layer is more conducting and the top *p*-type layer is more piezoelectric than their pristine counterparts. The partial screening in $\mathbf{p_{Ar}}$ layer due to free carriers (holes) is further reduced because of the formation of the depletion region. However, the output is reduced due to the rapid screening of the positive piezoelectric polarization in the $\mathbf{p_{Ar}}$ layer by free electrons from the *n*-type layer, leading to the significantly lower output observed.

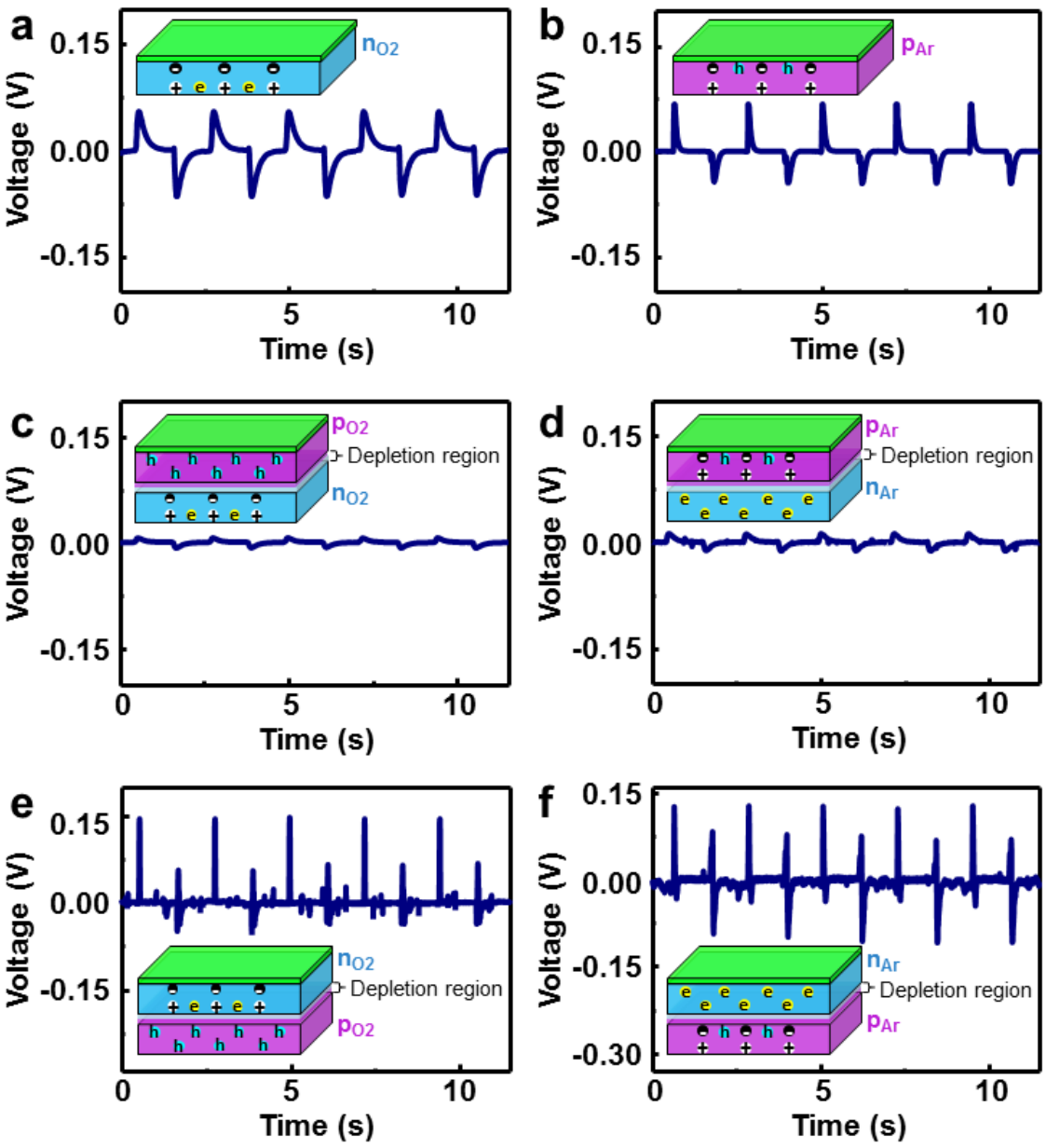

Figure 19 Output voltage for single layer and homojunction structures treated with either O_2 or Ar plasma. The sample naming convention follows that of the main text and the suffix denotes the plasma treatment used. Treating the *n*-type layer with (a) O_2 plasma (n_{O2}), or the *p*-type layer with (b) Ar plasma (p_{Ar}) reduces the free charge carrier concentration, thus improving output. Treating np structures with either (c) O_2 or (d) Ar plasma, the output voltage is greatly reduced. In the pn configuration, a noticeable improvement is observed for (e) O_2 and (f) Ar plasma treated samples.[87]

On the other hand, when a **pn** structure is used, the output is enhanced relative to the single layer device (Figure 19e, f). In an O_2 plasma treated **pn** structure ($\mathbf{p_{O2}n_{O2}}$) (Figure 19e), the bottom *p*-layer is conductive while the top *n*-layer is piezoelectric. Under compressive strain, the positive piezo-polarization charges induced at the bottom surface of the top *n*-layer experiences less internal screening from free electrons due to the O_2 plasma treatment and the depletion region formation. Additionally, the junction is now under reverse bias due to the distribution of piezoelectric polarization. It has been previously demonstrated that a *p*-*n* junction under reverse bias can function similarly to the Schottky barrier used in typical piezoelectric nanogenerator.[71] As the junction inhibits the flow of electrons from the circuit into the nanomaterials, the screening effect is slowed down. Moreover, the negative piezo-polarization charges induced at the top surface of the top *n*-layer are undampened and can more effectively drive electrons through the top electrode and external circuit, producing enhanced piezoelectric output of 146 mV (Figure 19f). Enhancement is also observed in the Ar plasma treated **pn** structure ($\mathbf{p_{Ar}n_{Ar}}$) sample, where the bottom *p*-layer is piezoelectric while the top *n*-layer is conductive. The positive piezo-polarization charges induced at the bottom surface of the bottom *p*-layer is unscreened, while the negative piezo-polarization charges experience reduced screening because of both the Ar-plasma treatment and the formation of the depletion region. These negative piezo-polarization charges can effectively repel electrons in the *n*-type region which accumulate at the interface with the PMMA layer. Both the negative piezo-charges and the undampened positive piezo-charges in the *p*-layer drive electrons through the rest of the circuit, producing significant piezoelectric output of 123 mV (Figure 19f). The average outputs are summarized in Table 5 and the output currents in Appendix D.

Table 5 Average output voltage and current of homojunction nanogenerators after oxygen or argon plasma treatment.

	O_2 plasma		Ar Plasma	
Configuration	Voltage (mV)	Current (nA)	Voltage (mV)	Current (nA)
n	55.3	1.17	n/a	n/a
p	n/a	n/a	66.9	1.18
np	7.00	0.269	12.2	0.528
pn	146	3.04	123	3.67

4.5 Homojunction Nanogenerators for Gesture Detection

Expanding on this demonstration of enhanced mechanical energy harvesting, piezoelectric nanodevices may also find unique applications as self-powered active sensors without external bias for detecting small-scale motion in biological systems,[91, 92] and potentially enabling novel human machine interfacing.[93] In particular, there has been a growing interest in wearable systems for hand gesture recognition for remote sensing and controlling. Visual approaches using cameras and computer vision algorithms have been implemented to interpret sign language with great success,[94, 95] but require external equipment and adequate lighting to function. The identification and recognition of posture, gait, and human behaviors have also been realized by wearable electronics based on electromyography[96] or photo-reflector arrays,[97] but neither device is truly conformable to the human body. Recent progress in skin-like electronics for measuring surface electromyography enables novel human-machine interface conformable to human skin.[98] Whereas, all these existing technologies for gesture recognition require an external power source, which may complicate the system design and limit operation schemes. Inspired by this, I explored the feasibility of our *p-n* homojunction piezoelectric devices for wearable

self-powered gesture recognition, which can directly recognize the small-scale movement of human muscles and convert it into electrical controlling signals without additional power source.

As the maximum output was obtained from the **pn** device, I proceeded to use this architecture to develop an ultra-thin, wearable piezoelectric device for detecting movement in flexor muscles in human fingers. Briefly, a polymer stack of PMMA (100 nm) and Ecoflex® silicone rubber (30 μm) were applied to a glass slide. The 1% Sb-doped *p*-type and *n*-type NW films were sequentially grown in the patterned AZO region on the PDMS using the above method. An insulating layer of the same silicone (20 μm) was applied to the structure followed by a sputtered layer of AZO as the top electrical contact. A 300 μm encapsulation layer of silicone was coated onto the device for protection. The flexible piezoelectric device was then released from the glass substrate by dissolving the PMMA sacrificial layer. The final device has a high degree of transparency and flexibility (Figure 20a). The small modulus (~55 kPa[99]) and thickness of the device (~350 μm) allows for good adhesion of the device to the skin by van der Waals forces, without needing hardware fixture or adhesive tapes, and the underlying skin can still naturally stretch and fold with minimal interference (Figure 20a). Transport measurement confirmed the successful formation of a *p*-*n* junction in the final device.

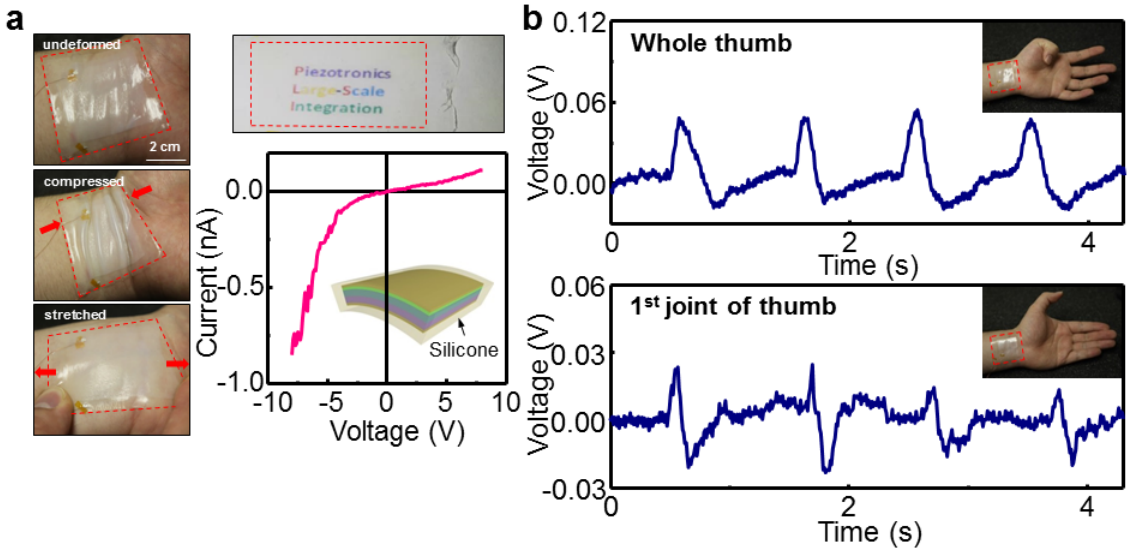

Figure 20 Homojunction nanogenerator grown in the pn configuration on silicone rubber for gesture recognition by measurement of flexor movement. (a) Photographs show the devices conformability and stretcahbility when mounted on a human wrist (left), and its transparency (top). The IV characteristics of the device was measured as before, confirming the presence of a pn junction. (b) The output of the device was measured based on the difference in flexion of the thumb. When the whole thumb is bent, a significantly higher output peak is observed, while maintaining a similar signal pattern.[87]

To demonstrate device's applicability, it was attached to a human wrist to detect movement of the underlying tendons, and the piezoelectric output produced based on different hand gestures was measured. The device's capability of detecting the difference in muscle movement even when the behavior of the same finger varies slightly was investigated. First the thumb was quickly bent and extended, producing a 50 mV pulse with each cycle (Figure 20b top). Furthermore, by repeating the same motion with only the first joint of the thumb, a smaller voltage pulse (15 mV) is produced. As a similar signal pattern is observed, the degree of bending can be identified based on signal intensity. Using this as a starting point, the output based on individual fingers being bent was compared. In a relaxed state, no output voltage was measured. Each finger was then bent and released in sequence starting with the thumb, producing distinct current pulses (Figure 21 left). The movement of the fingers is controlled by a variety of muscle groups. The extrinsic muscle

group in the forearm, the flexor digitorum superficialis, controls flexion of the index, middle, ring, and little finger, while the thenar muscle group in the hand control the thumb.[100] Since distinct outputs with characteristic patterns were observed for each finger, it suggests that the flexion of each individual finger can be identified based on the pattern shape from our piezoelectric device. A much larger pulse is observed when the little finger is flexed. This is because a separate group of muscles in the palm, the hypothenar eminence, also controls movement of the little finger. Because of the device's proximity to the palm, movement from both the hypothenar and flexor muscles are detected, thus producing a larger pulse. To show device consistency, the same device was attached to the subject's right hand wrist, and the same sequence was performed. A similar pattern was observed, albeit with higher signal amplitude (Figure 21 middle). I believe that this is because the device is attached to the subject's dominant hand, which is naturally stronger and more dexterous. Some similarities are observed between this pattern and those observed in the left hand, most notably that the little finger is still the dominant signal. The device was also attached to the back of the subject's left hand to measure output from the extensor tendons during gesturing. The output voltage was over an order of magnitude greater than those measured from the wrist (Figure 21 right). As the tendons are much closer to the surface of the skin in this case, a much stronger signal from this device can be expected. The pattern observed in this position differs significantly from the signals from the wrist. By using two or more devices in conjunction with each other, a more complex signal pattern can be obtained allowing for higher resolution gesture recognition with enhanced sensitivity and accuracy. To demonstrate the device stability, the output voltage was measured when the same gesture sequence was repeated for multiple cycles (Figure 21 bottom). Due to the

inconsistencies inherent to something as complex as finger motions, only representative output curves are presented here. The original output for these sequences is presented in Appendix D.

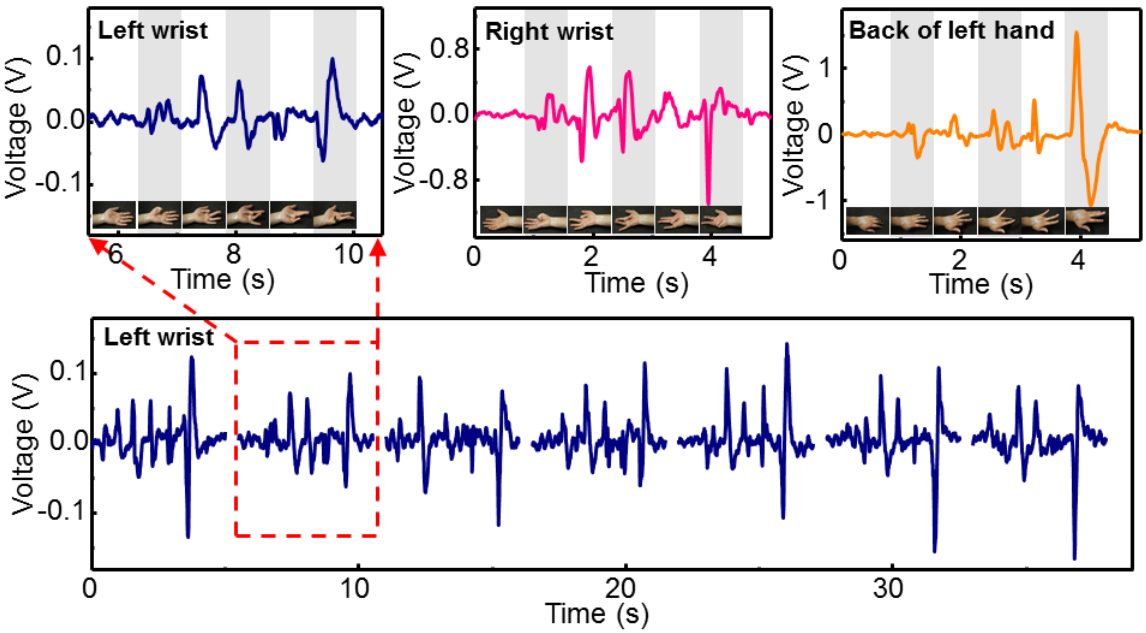

Figure 21 The device was used to measure signals when fingers were individually flexed and extended starting with the left wrist (left). A distinct signal pattern is observed for each finger. The same pattern was repeated with the right hand (center), producing a similar pattern, but with higher intensity. The device was attached to the back of the hand (right) to measure movement of the extensor tendons, producing a unique signal. By repeating the same gesture several times with the left hand, the device's stability was demonstrated.[87]

To develop a deeper understanding of this device's operation for gesture detection, the output for different gestures was investigated. The subject's fingers were bent in sequence starting with the thumb. However, in this case, the fingers were only released after all of them had been bent Figure 22a. A different signal pattern is observed for the thumb in this case, as it was kept bent and hence only partial patterns corresponding to the bent state from the signals in Figure 21 was observed. When all five fingers are released, a large pulse is observed with its own distinct signal pattern

For our device to be a fully functional gesture detector, the signals when multiple fingers are bent simultaneously must also be distinguished. The bent thumb (1 finger) from

earlier measurement was used as a baseline (Figure 22b). Next, the middle and ring fingers were bent and straightened simultaneously (2 fingers), producing a slightly higher peak output with a different shape. The output increases again when the index finger is added (3 fingers), however, the difference in peak output is not equal to that of bending the index finger individually, showing that this is not a simple additive process. Once the little finger is added (4 finger), its output dominates over the others resulting in a much sharper output. Finally, when a clenched fist is formed (5 fingers), the highest output is observed at -0.6 V. The signal shape is similar to that of the 4 finger case, as the little finger is still the dominant signal. With future structural optimization and signal processing studies, these devices could see use in human-electronics interfacing, bio-probes and therapeutic devices.

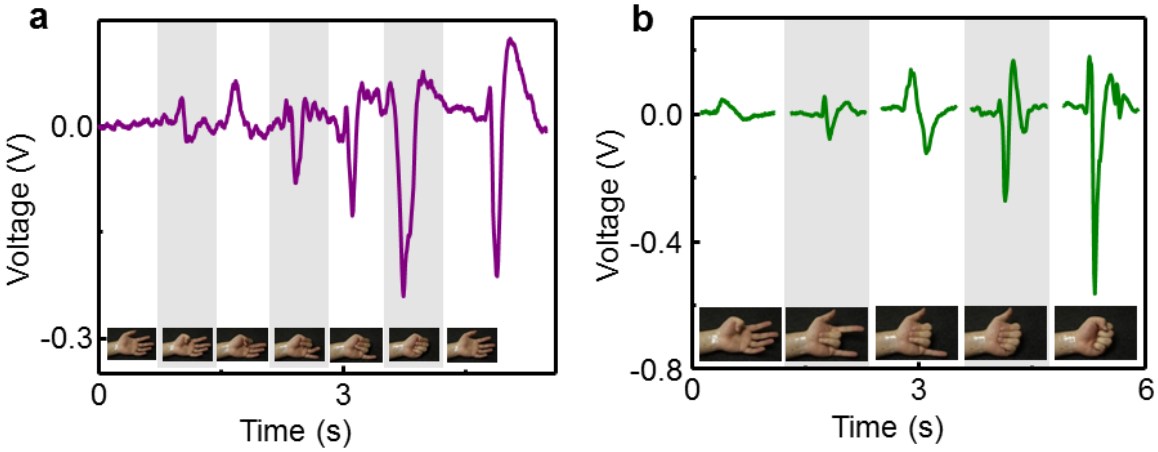

Figure 22 (a) The fingers were sequentially bent starting with the thumb, but unlike the previous pattern, were not released until the end, producing unique "half signals" compared to previous gestures. (b) Multifinger gestures were used to demonstrate the device's ability to detect more complex gestures. In order, the patterns are thumb; index and middle; index, middle, and ring; index, middle, ring, and litte; and all five fingers.[87]

4.6 Conclusion

In conclusion, for the first time the applicability of ZnO homojunction nanostructures in enhanced mechanical energy harvesting was demonstrated. By systematically designing and testing different material configurations and treatments, the

optimum materials design was found, and the resulting output is in agreement with previous fundamental theories on the working mechanism of piezoelectric NGs. The synthesis method presented in this work for producing densely packed NW films may serve as viable alternatives to conventional sputtered thin-films owing to its very low synthesis temperature. While this study only focused on bilayer structures, it shows the potential to produce more intricate *n-p-n* or *p-n-p* bipolar junctions for more complex electronics. Furthermore, the presented ultra-thin wearable piezoelectric device based on ZnO homojunction nanostructures is capable of detecting small-scale subdermal movement from the tendons in the human wrist and distinguishing different motions and hand gestures. The electronic output signals from our devices after processing the encoded information in ambient stimuli such as the muscle movement may make possible the control of embedded electronics and sensors for intelligent and adaptive operations in human-electronics interfacing, bio-probes and therapeutic devices.

CHAPTER 5: ZINC OXIDE CORE-SHELL BULK HOMOJUNCTIONS

5.1 Introduction

Core-shell nanowire structures have often been of interest for optoelectronics due to their high interfacial area. Numerous heterojunction structures with ZnO have been demonstrated using materials such as ZnS,[101] ZnSe,[102] iron oxide,[103, 104] and Al_2O_3,[105] showing applications in photovoltaics, light emitting diodes, and gas sensors. Because of the difficulties in producing *p*-type ZnO, there have been relatively few studies on growth of homojunction nanostructures,[106] which do not make any claims of long-term stability. In this section of my thesis, I demonstrate how core-shell ZnO nanowire homojunctions can be grown in multiple different configurations using the antimony based dopant described previously. Through thorough STEM analysis, I investigated the microstructure of these nanowires, and finally showed a simple application in ultraviolet photodetection.

5.2 Synthesis of Core-Shell Nanowires

Core-shell structures were grown based on previously demonstrated nanowire growth techniques. The following process is shown schematically in Figure 23a. Glass substrates were chosen as substrates, and 100 nm of aluminum doped zinc oxide was sputtered on to act as a seed layer and bottom electrode for subsequent electrical measurements. Compared to previous work, the zinc nitrate and HMTA concentrations were lowered to 5 and 2.5 mM in order to produce finer ZnO nanowires. Ammonium hydroxide was added to the solution in order to help prevent self-nucleation, thus

promoting more uniform nanowire growth. To produce *p*-type nanowires, antimony glycolate solution was added in a ratio of 1% relative to zinc. In both cases, 0.4 M ammonium hydroxide was also added to the solution, and the nanowires were grown at 95°C for 2 hours. Because a much lower zinc concentration is being used, not as much ammonia is needed to suppress homogeneous nucleation (0.8 M at 25 mM zinc nitrate). After growth, the substrates were removed from the solution, and placed into a new solution to grow the shell layer. For the shell layer, the solution concentrations used for the *n*- and *p*-type films from Chapter 4 were used.[87] Briefly, 50 mM of zinc nitrate and 25 mM HMTA were used for the *p*-type shell, with sodium citrate added to promote shorter, thicker wires. The concentration was reduced by half for the n-type shell. Ammonia was added to both solutions (0.5 M) and the film was grown at 75°C for 2 hours.

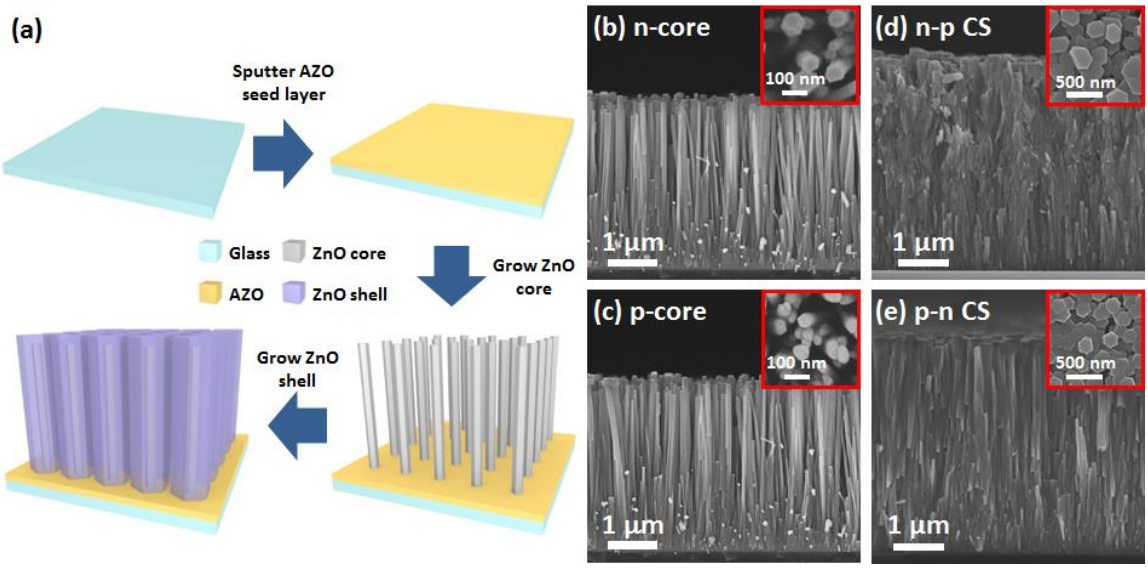

Figure 23 (a) Schematic representation of bulk homojunction growth. (b) *n* and (c) *p*-type core nanowires grown using the hydorthermal method. (d, e) Complete core-shell structure grown by putting the nanowires from the previous step into a new growth solution for 2 hours.

As can be observed from the cross-sectional SEM images, fine nanowires with a diameter of 0.5-1 µm formed after growth of the core layer (Figure 23b,c). The wires are

about 3 μm long, and there does not appear to be too big of a difference in morphology between the doped and undoped wires. After growing the shell layer, the nanowire length only increased by 1 μm, while the nanowire diameter and density increased dramatically, causing them to grow until they impinged upon each other (Figure 23d,e). The *p*-type shell layer also has some roughness to its surface due to the presence of the dopant. By taking a sample out at multiple intervals before the 2 hour mark, we can observe a steady increase in the nanowire diameter during the growth of the *p*-type shell (Figure 24). After only 15 minutes of growth, some roughness is seen on the nanowire surface from the shell layer growth, but there is not much change in the diameter. As the growth progresses to 30 minutes, the nanowires begin to regain their hexagonal structure, and become completely hexagonal again at 60 minutes. From the cross sectional view, the length remains constant over the first 30 minutes, and begins to grow longer after 60 minutes. From 60 to 120 minutes, the space between the nanowire tips fills up until a dense film is formed as seen in Figure 23.

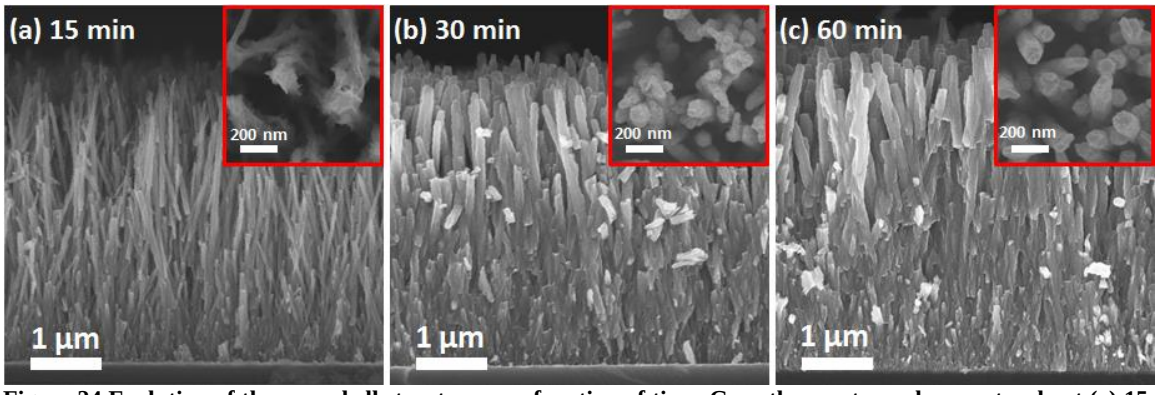

Figure 24 Evolution of the core-shell structure as a function of time. Growth was stopped prematurely at (a) 15, (b) 30, and (c) 60 minutes.

5.2 TEM Analysis

In order to characterize these structures, TEM and STEM analyses were used. For the purposes of TEM, the shell layer was only grown for 15 minutes, as clear images cannot be obtained if the sample is too thick. For the sake of brevity, n-type core, *p*-type shell nanowires will be referred to as **np** nanowires and *p*-type core, n-type shell nanowires will be **pn** wires. From the TEM image (Figure 25a), we can see an obvious difference in contrast between the core and shell layers. In the **np** nanowire, some porosity is observed in the shell layer. As demonstrated previously, this is characteristic of antimony doped ZnO nanowires. Due to its much larger atomic radius, the Sb atoms interfere with normal nanowire growth. The antimony forms plate-like precipitates in the nanowire, and normal ZnO growth continues around it, causing voids to form in the structure. These voids become even clearer in the dark field STEM image in Figure 25b. The n-type core can be easily differentiated as the bright white area in the center due to its lack of defects. Using high resolution TEM (HRTEM) (Figure 25c), we can observe that despite its porous nature, the shell layer is still monocrystalline due to the regular lattice spacing across the nanowire. Furthermore, we do not observe any distortion in the inset diffraction pattern in Figure 25d, suggesting that the shell is a continuation of the previous core growth, rather than a new nucleation and growth event. This is unlike the planar homojunction growth from Chapter 4, where the second layer of growth was a new nanowire growth, despite using the same growth solution. From the top view SEM images in Figure 23b, the nanowire tips are rounded, lacking the sharp anguler facets seen in the complete nanowires following the shell layer growth. This implies that the nanowires had not yet reached an energetically favorable aspect ratio, leading to continued growth.

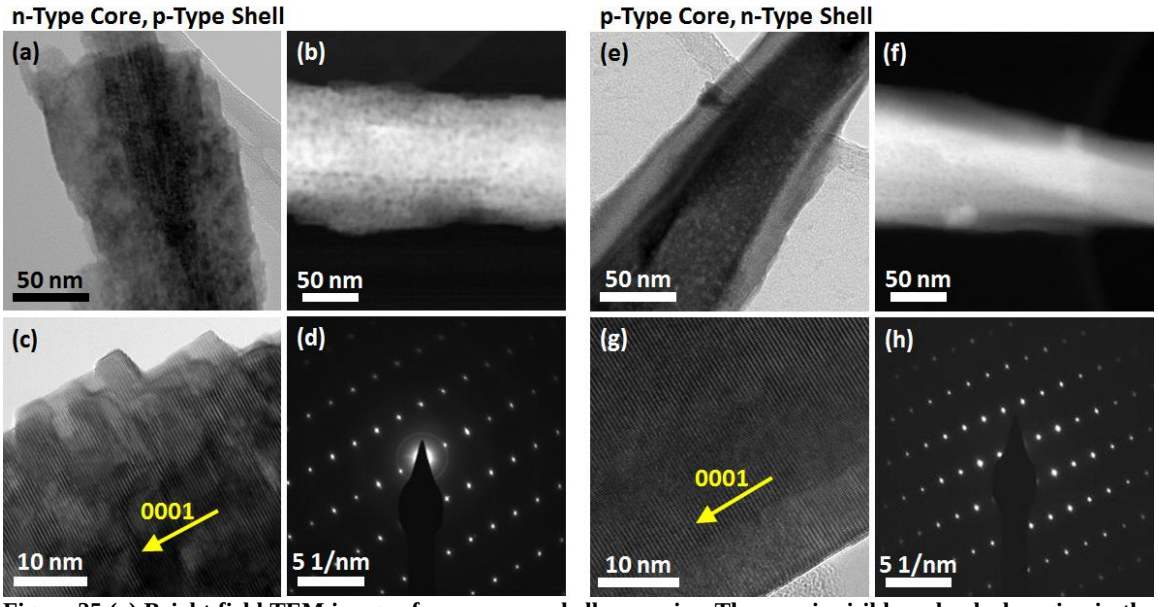

Figure 25 (a) Bright field TEM image of an n-p core shell nanowire. The core is visible as he dark region in the center. (b) STEM image of the n-p nanowire. The core is visible as the bright white center, while a porous shell can be seen consistent with previous reports on Sb doped ZnO. (c) High resolution TEM image of the shell layer. From the (d) SAED, the nanowire is single crystalline despite the multiple growth steps. (e) Bright field TEM image of the *p-n* core shell nanowire. The porosity caused by Sb is visible exclusively in the core layer. (f) STEM image of the core-shell wire. While the porosity is visible, the contrast is reduced due to the presence of the uniform shell layer. (g) HRTEM image and (h) SAED of the pn nanowire.

For the **pn** structure, a similar pattern is observed. From the TEM image (Figure 25e), we can see a darker core while the shell layer is lighter due to the difference in thickness. We can see some white spots in the core due to the void formation from doping. This is reinforced in the STEM image (Figure 25f), where the voids are also visible only in the core region, while the shell is clean. We do not get as clear a contrast from the voids in this case due to the presence of the clean shell layer. Similarly to the **np** sample, the HRTEM image (Figure 25g) also suggests that the structure is monocrystalline due to the regular lattice spacing. This is also supported by the inset diffraction pattern image (Figure 25h), where we do not see any distortion despite the multiple growth steps.

5.3 Electrical and Optoelectronic Characterization

In order to characterize the electrical properties of these homojunction films, 100 nm of ITO was deposited on top of the nanowires to form a top electrode. The AZO seed layer was used as the bottom electrode. In both the **np** and **pn** samples, the bottom (i.e. the core) was under forward bias. In both samples, we observe rectification consistent with *p-n* junction behavior (Figure 26). The **pn** sample has a turn on voltage of about 3V, while the **np** device has a turn on voltage of about 2.5V. There is also a noticeable amount of leakage when the devices are under reverse bias. Because of the way the sample is grown, there may be some contact between the shell layer and the bottom electrode. No patterning is used during growth of the core nanowire, so there is potentially exposed seed layer/electrode in between the nanowires. When the shell layer grows and backfills that space, it is possible for it to extend all the way to the seed layer, causing a short. This has been mitigated experimentally by allowing the core layer to grow for longer periods of time, which causes the nanowires to coalesce at the root, as can be seen from the cross sectional SEM images in Figure 23. Because of the random nature of nucleation and growth, this does not completely eliminate the issue, leading to some shorting, and thus leakage. Lithography techniques such as e-beam lithography or photolithography were considered to grow patterned ZnO nanowires for this investigation. However, the common photoresists used for these techniques, PMMA and SU8 were not compatible with high ammonia concentration used in the growth solution, which would cause them to swell and peel off the substrate. For future investigations, much more elaborate patterning techniques may need to be considered for investigating this growth method.

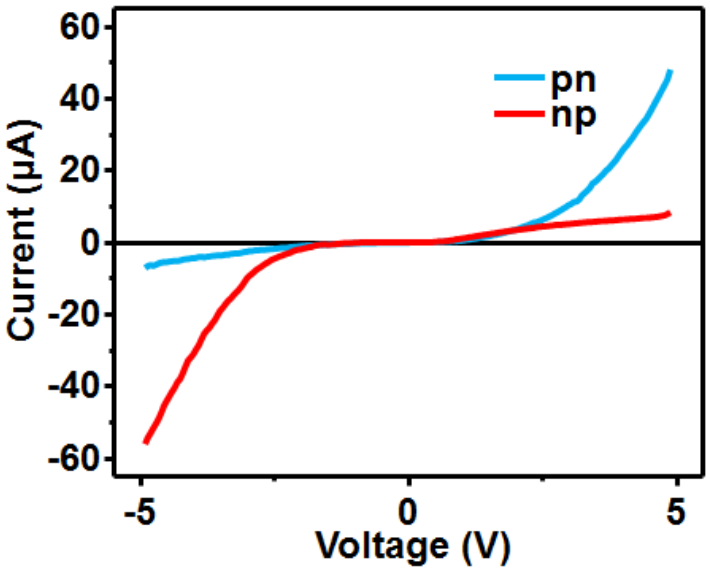

Figure 26 IV curves of the bulk homojunction structures. In both cases, the bottom layer is under positive forward bias.

The photoresponse of the **np** device was briefly investigated using an ultraviolet lamp. Because of the band gap of ZnO, it should primarily absorb these wavelengths. The lamp had two different wavelength settings with different power levels at 0.66 mW/cm^2 at 365 nm, and 1.61 mW/cm^2 at 254 nm. From the IV curves, it can be seen that the induced photocurrent causes the conductivity to increase in the device under both forward and reverse bias (Figure 27). Because the energy density of the 254 nm light is higher, a stronger response is observed. The standard method of normalizing photoresponse over different intensities is the responsivity term R[107] defined as:

$$R = \frac{I_{light} - I_{dark}}{P_{light}}$$

where I_{light} and I_{dark} are the current under illumination and in the dark, respectively, and P_{light} is the power of the light source. With an active area of 0.25 cm^2, the calculated responsivity for the two light sources was 0.024 and 0.015 A/W for the 365 and 254 nm light, respectively, so the sensitivity is on a similar order of magnitude for both

wavelengths. By increasing the driving voltage, the responsivity can be increased up to 0.203 A/W at 4V, putting it on par with commercially available Si based photodiodes.

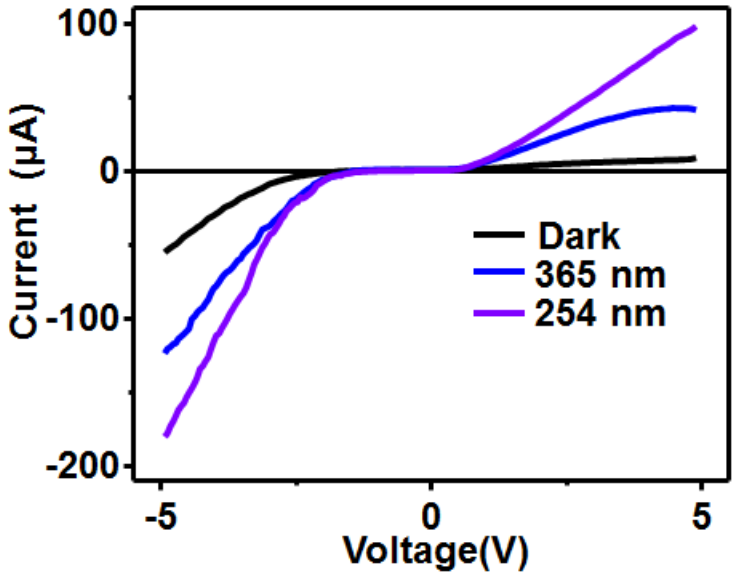

Figure 27 Photoresponse of the np bulk homojunction structure under ultraviolet light at 254 and 365 nm. The bottom layer is under positive forward bias.

Table 6 Dependence on responsivity (R) on wavelength and driving voltage. The units for R are A/W.

Voltage (V)	365 nm	254 nm
1	0.024	0.015
2	0.089	0.058
3	0.158	0.114
4	0.203	0.174

5.4 Conclusion

In conclusion, ZnO core shell homojunction structures were grown using a low temperature, solution based hydrothermal method. By combining growth methods for fine wires and dense films, a homojunction structure with a high surface area to volume ratio was produced. From microscopy investigations, despite the further changes in growth solution parameters, the telltale signs of doping, i.e. voids caused by antimony integration are still present, showing the further flexibility of this technique. Furthermore, the multistep

growth used still produces single crystalline nanowires. By performing simple optoelectronic measurements, in the ultraviolet range, this device shows potential for photodetection. There is still room for refinement in both the growth to reduce the shorting between the shell layer and the substrate, and in other potential optoelectronic applications such as light emission, which will be considered for future investigations.

CHAPTER 6: P-ZNO/N-SI HETEROJUNCTIONS FOR OPTOELECTRONICS

6.1 Introduction

Up until now, the research presented in this thesis has focused exclusively on *p*-*n* homojunctions produced using ZnO nanowires. While there is a novelty in a pure ZnO system, in order to demonstrate the commercial applicability of *p*-type ZnO, it is also important to show how it can be integrated with other semiconducting materials to produce heterojunction structures. Silicon is an ideal material for this investigation as it is a thoroughly researched and well understood material which is the basis for much of our modern technology. While ZnO/Si heterojunctions have been investigated in the past,[72, 73, 108] it has been done so with the opposite doping, i.e. *n*-type ZnO and *p*-type Si. With the help of Dr. Naoki Fukata at the National Institute for Materials Science in Tsukuba, Japan, for the first time, a solution derived *p*-ZnO/n-Si heterojunction structure was demonstrated. To increase the contact area between the two materials, Si nanowires grown through nanoimprint lithography were used as the base with ZnO grown off of it. After investigating the basic materials properties of this structure, its applicability as a photodetector was investigated.

6.2 Synthesis and Materials Characterization

Silicon core nanowires were synthesized through nanoimprint lithography and the Bosch process using n-Si(100) substrates.[80] Si substrates were patterned with 30 nm-thick Cr layer by UV-imprint lithography and lift-off processes. Then, SF_6 plasma followed by

C_4F_8 plasma was applied for deep Si etching to form SiNW structure. The flow rates of SF_6 and C_4F_8 were both fixed at 35 sccm under chamber pressure control of 0.75 Pa. The wires produced had a diameter of 150 nm, a length of 1.3 μm and a pitch of 500 nm. From the SEM image in Figure 28a, we can see that the nanowires and their spacing are uniform. ZnO nanowires were then grown using the hydrothermal method. To start, the Si nanowire samples were briefly etched in hydrofluoric acid to remove the oxide layer, and a 100 nm thin layer of ZnO was sputtered onto the nanowires to act as a seed layer for subsequent growth. From there, the substrate was floated face down in a solution bath containing 25 mM zinc nitrate, 12.5 mM hexamethylenetetramine (HMTA), 0.7 mM sodium citrate, 0.5M ammonium hydroxide, and 0.25 mM antimony glycolate dopant solution. The preparation of the dopant solution is described in previous literature.[109] Sodium citrate was added to produce lower aspect ratio ZnO nanowires which pack more densely during growth. These samples were grown for 1 hour at 75°C.

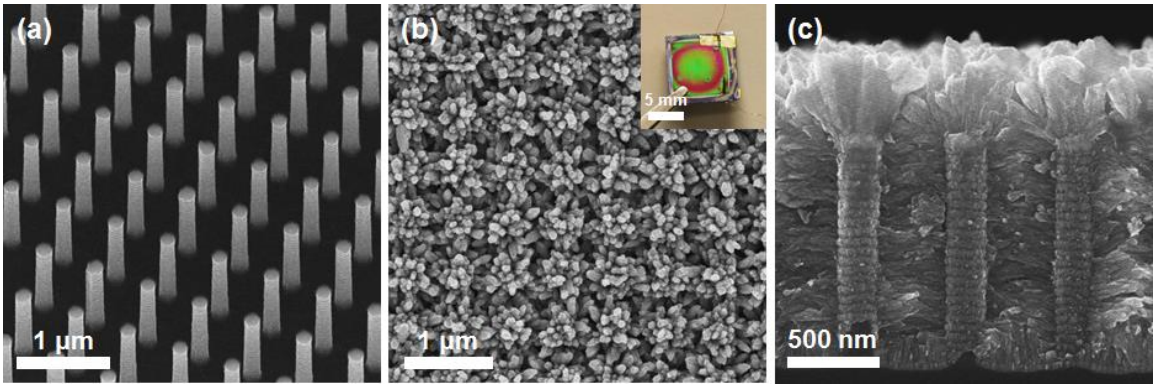

Figure 28 (a) SEM image of *n*-type Si nanowires grown through nanoimprint lithography. The nanowire dimensions are 1.3 μm in length, 150 nm in diameter, and spacing of 500 nm. (b) Top view of Si nanowire array following *p*-type ZnO nanowire growth. The inset shows a photograph of the whole structure. (c) Cross-sectional view of the heterojunction structure.

From a top view SEM image in Figure 28b, we can see urchin like ZnO nanowire structures with the same periodicity as the base Si. From the photograph in the inset, it

appears that the ZnO nanowires grew evenly over the entire sample By cleaving the sample and looking at the cross section (Figure 28c), we see that the urchin structures form from the tips of the Si nanowires, where the ZnO nanowires fanned out during growth. Along the sides of the Si wires, we can see that the ZnO grew perpendicularly to the surface, coalescing and completely filling the spaces between Si nanowires. The length of the ZnO wires were limited by the growth of other ZnO on adjacent Si nanowires. The growth rate appears to have been uniform as the ZnO nanowires meet in the center. We can also observe a small amount of growth from the bottom of the substrate, but the length is limited by growth from the sides of the Si nanowires.

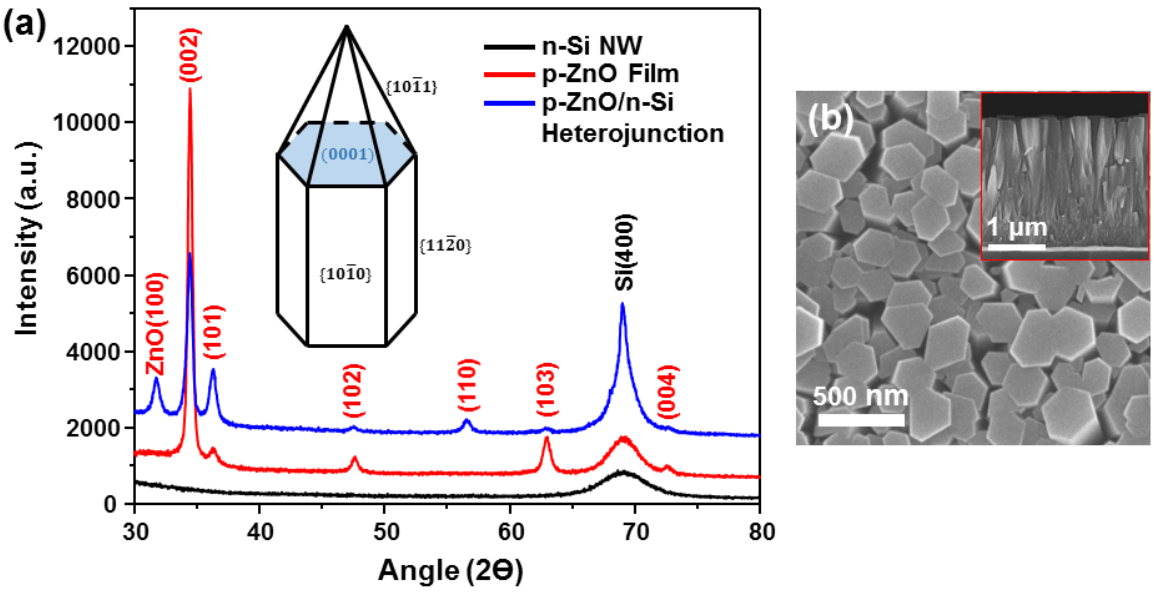

Figure 29 (a) XRD scan of the Si nanowire array, the *p*-type nanowire film grown on a flat Si substrate, and the nanowire heterojunction structure. The inset is a schematic of a partially grown ZnO nanowire with the crystal faces labeled. (b) SEM image of a *p*-type ZnO nanowire film grown using the same conditions for the heterojunction structure. The inset shows a cross sectional view of the same structure.

X-ray diffraction was used to further characterize the crystallinity of the as-grown structure (Figure 29a). As a control, first a Si nanowire array was measured, and only a Si(400) peak is observed. A ZnO nanowire film grown using the same method on a flat silicon wafer (Figure 29b) was also scanned as a comparison. For this film, a Si(400) peak

is still observed due to the underlying substrate, but several characteristic peaks for ZnO are also observed, the most prominent being the (002) peak. When zinc oxide nanowires are grown in the presence of sodium citrate, the citrate ions bind to the (0001) surface, slowing down growth along the c-axis, thus producing shorter, but fatter wires.[40] On a flat substrate, this will cause them to coalesce into a densely packed film.[87] Because these densely packed nanowires are well aligned, a strong (002) peak is observed. The next strongest peaks at (103) and (101) correspond to the incompletely grown nanowire faces.[110] There is always some irregularity during nanowire growth, but based on its relative intensity compared to the (002) peak, and the SEM image, this effect is minimal.

When taking the diffraction scan for the heterojunction structure, a combination of all the previously observed, as well as a noticeably new ZnO (100) and (110) peaks which correspond to the nonpolar side surfaces of the ZnO nanowire are observed. This makes sense as a large number of nanowires are growing parallel to the substrate. Because the ZnO layer is no longer as thick in this sample compared to the film, ZnO(002) peak has become weaker relative to the Si(400) peak. Furthermore, the intensity of the (101) peak has also increased due to the larger number of incompletely grown nanowires. The ZnO grown on the Si nanowires have a tapered end as opposed to the complete hexagonal structure observed in the film sample. While in principle, the hexagonal wires observed in Figure 28 should be obtainable, despite being grown at the same conditions, only partially grown nanowires were obtained. As the nano patterned Si substrate has a higher surface area than the flat surface, it's possible that more of the nutrients in solution were depleted during the same time, resulting in incompletely grown nanowires.

6.3 Optoelectronic Properties

In order to measure the device's electrical properties, 100 nm of ITO was sputtered onto the ZnO side to serve as the top electrode, while a silver contact was deposited on the back side of the Si wafer to form Ohmic contacts. Gold wires were attached to the substrate using silver paste as electrical leads. The completed structure is shown schematically in Figure 30. A Keithley 4200 semiconductor parameter analyzer was used to perform all electrical measurements. When the IV behavior was measured without any illumination under positive forward bias, strong rectification behavior is observed, showing that a *p-n* junction had formed (Figure 30). The samples were then annealed at 200°C in a nitrogen environment for 30 minutes in order to fuse the components together and improve the contact between the components. This led to a dramatic increase in conductivity under forward bias. Under reverse bias, the conductivity decreased, showing that the annealing process also helped reduce leakage.

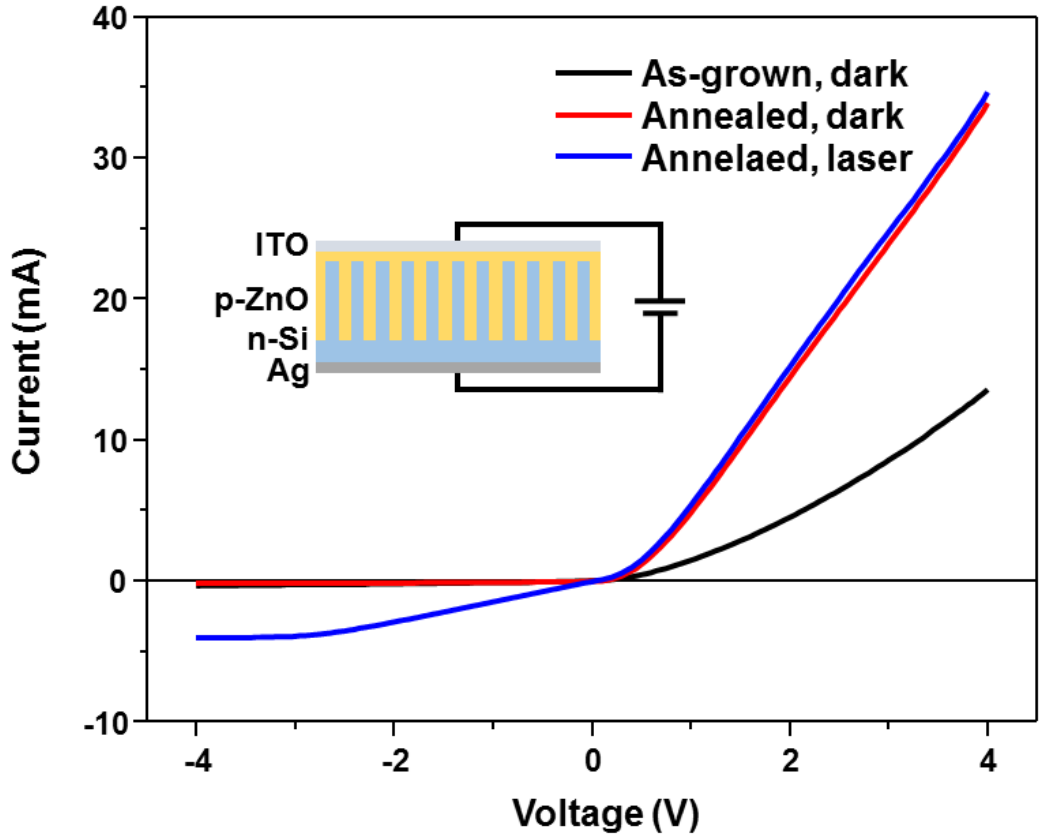

Figure 30 I-V behavior of the *p*-ZnO/n-Si heterojunction structure. The sample was measured in the dark both as-grown, and after annealing at 200°C in nitrogen. The photoresponse was measured with the annealed sample using a 442 nm laser.

To test the homojunction's photoresponse, a 34 mW laser with a wavelength of 442 nm was illuminated on the device. This led to a significant increase in the devices conductivity under reverse bias, while the conductivity only increased marginally under forward bias. As the device is fairly conductive under forward bias to begin with, the photocurrent produced is rather insignificant. As a result, all further photoresponse measurements were performed when the device was under a constant reverse bias of 1V. The photoresponse of the annealed and unannealed samples were compared, and there was a significantly higher increase in current under the same illumination. This can be partially accounted for by the reduction in leakage following annealing. It is also possible that the

annealing helped increase light transmission through the ZnO to the underlying Si layer.[111] More likely, the sintering increased the carrier mobility of the two components, leading to larger photocurrent. The photoresponse time was quite fast, less than 40 ms, which is the detection limit of our equipment.

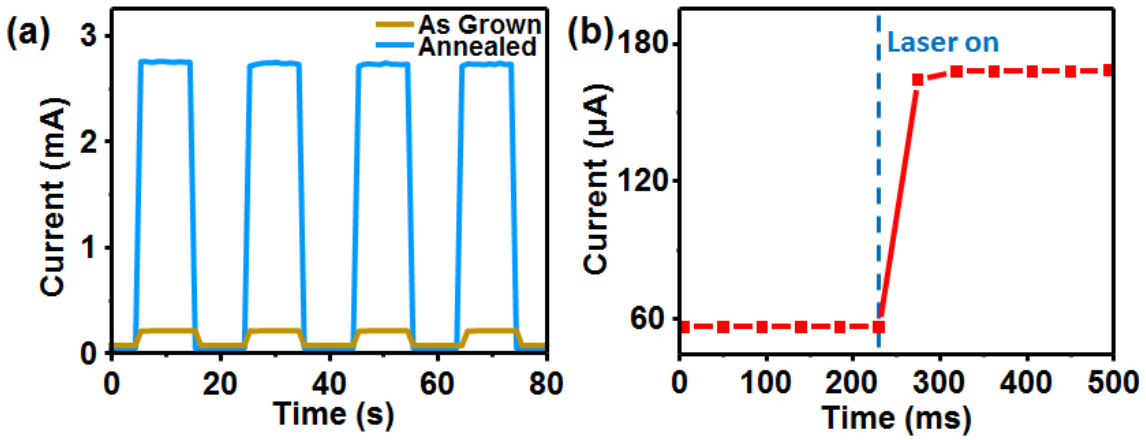

Figure 31 (a) Photoresponse of the annealed and unannealed heterojunction structure under illumination from a 34 mW laser. (b) Time response of the annealed device. The spacing between points is 40 ms. The laser intensity in this case was 100μW

The photoresponse of the device was investigated at various laser intensities to determine the heterojunction's sensitivity. The laser intensity was lowered by approximately an order of magnitude between each step, starting from 1.16 mW, and ending at 490 nW. As the light intensity decreased, the photocurrent also decreased dramatically. In the mW intensity range, the resulting current change is 1.21 mA. On the opposite end of the spectrum, at 490 nW, the current change is 442 nA. These values were normalized using the responsivity term R described in the previous chapter. This value was calculated for the different intensities and plotted alongside the corresponding change in current in Figure 33. The average photoresponsivity at these intensities was 1.02 A/W with a standard deviation of 0.07. This is several orders of magnitude higher than the 12.8 mA/W

observed for similar structures in previous literature.[72] Due to the denser nanowire growth, there is higher contact area, and thus more electron-hole pair generation.

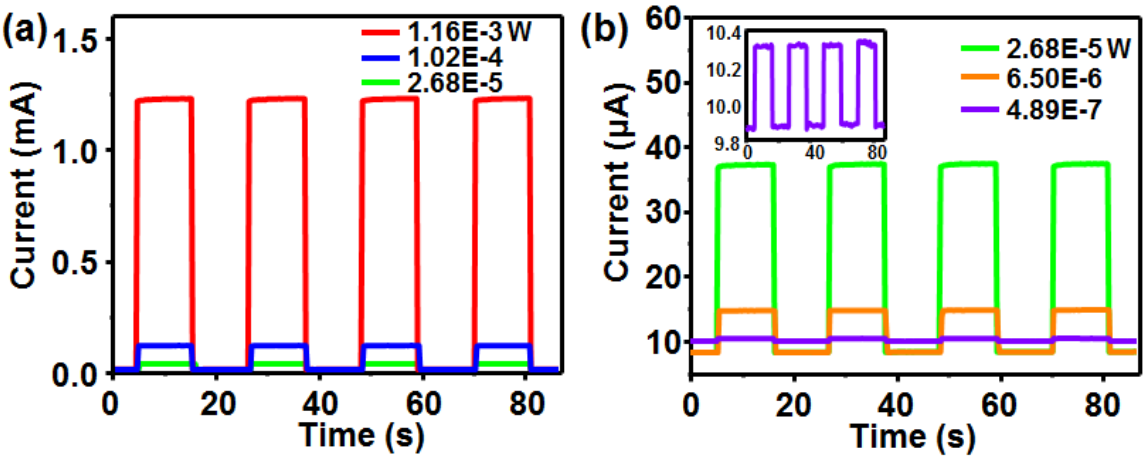

Figure 32 Heterojunction photoresponse measurements for different laser intensities. The data was split into two different plots for clarity. The inset in (b) shows a zoomed in view of the response at 4.89E-7 W.

Using the same sample, the photoresponse was measured at 325 nm ultraviolet laser (Figure 34). At this wavelength, the ZnO should be the photoactive material as the photon energy is higher than the band gap of ZnO. At the same bias, the responsivity is considerably lower. From the shape of the response, there is a higher capacitance when absorbing UV light than visible. While these features may also be present under 442 nm illumination, due to the much lower induced photocurrent under UV light, these features become more dominant. This lowered sensitivity can be attributed to the absorption coefficient of ZnO[112] is generally less than that of silicon,[113] this is to be expected. It is unclear what effect the doping has on these optical properties, and should be considered for future research on the fundamentals of this material.

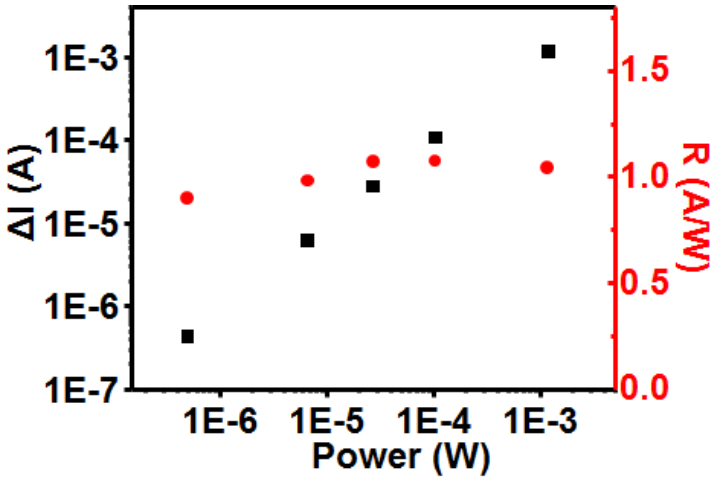

Figure 33 Current change and responsivity as a function of laser power for the heterojunction structure at 442 nm laser intensity.

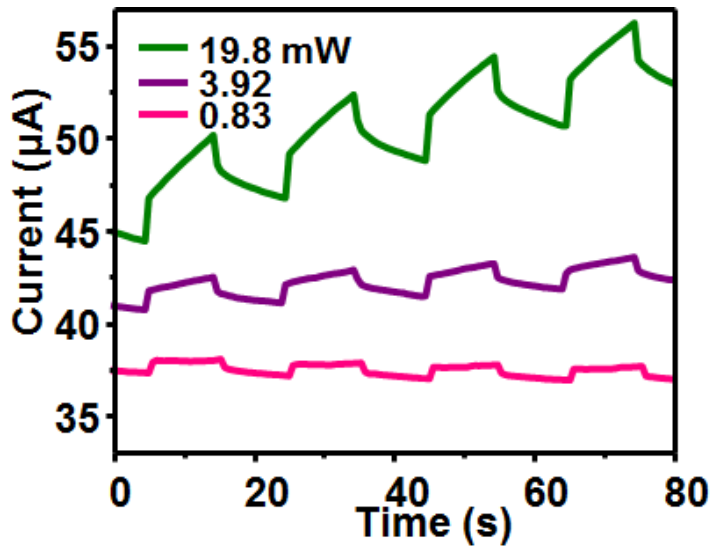

Figure 34 Photoresponse of the heterojunction photodetector at various intensities under 325 nm laser illumination.

6.4 Conclusion

In conclusion we have demonstrated the first ZnO/Si nanostructured heterojunction based off of solution grown *p*-type ZnO. The synthesis methods for both materials are simple and easily scalable, making this technique suitable for mass production. By using a solution designed to grow densely packed ZnO nanowires, it's possible to completely backfill the gaps between the Si nanowires, increasing the active area for photoresponse. The formation of a *p*-*n* junction between the two materials was confirmed, and a peak photoresponsivity of 1.02 was measured with a 442 nm light source. As Sb doped *p*-type ZnO is still a relatively new system, it is important to investigate its compatibility with other material systems in order to broaden its applications. While silicon is the most commonly used semiconductor today, there is the potential for other novel applications when integrated with other semiconductors such as GaN or CdTe. Other potential optoelectronic applications for this structure include water splitting, photovoltaics, and light emitting diodes.

CHAPTER 7: CONCLUSION

7.1 Summary of Work

Over the past four years as a graduate student here at Georgia Tech, I have made numerous contributions to both the fields of semiconductor nanowire growth and piezotronics through my studies of *p*-type zinc oxide. I have shown that not only is it possible to grow *p*-type ZnO using antimony as a dopant, but that it remains stably *p*-type for 3 years, more than double the time previously demonstrated. Furthermore, I have shown full mastery of the growth parameters, as I am able to produce a myriad of architectures from ultra-long wires, to fine wires, to thin films. I was also able to grow various *p-n* junction architectures such as stacked films and core-shell structures, all at low temperatures and cost in an aqueous environment. This point is especially important, as it has applicability in next generation flexible and implantable devices which depend heavily on less thermally robust polymer materials.

My main contribution to the field of piezotronics has been in showing that the piezotronic effect is universal to all piezoelectric semiconductors, regardless of primary carrier type. This investigation was only made possible through the development of the aforementioned ultra-long ZnO nanowires, as nanowires long enough for mechanical manipulation are needed to record any meaningful measurements. To further show that the piezoelectric properties remained intact, simple piezoelectric nanogenerators were fabricated using the doped nanowires. This concept was later expanded upon, as I showed that it was possible to enhance their performance by growing homojunction structures, which effectively reduce screening by free charge carriers through the formation of the

depletion layer. These homojunction structures were shown to have application in gesture detection, as they were grown on silicone rubber, then mounted to the human wrist. This device would produce voltage output when the fingers were moved, and the output could be correlated to different motions depending on its intensity and signal pattern.

To expand *p*-type ZnO's applicability to optoelectronics, its photodetection properties were demonstrated using both ZnO core-shell homojunctions, and branched heterojunctions with n-type Si nanowires. In both cases, because of the increased surface area between the two materials, it was possible to build simple photodetectors using both structures, which showed good response in the blue and ultraviolet range. The work with silicon is especially important, as it shows that *p*-type ZnO can be easily integrated with other semiconducting materials, opening up the possibilities for using it in other systems and applications.

7.2 Future Work

Despite the considerable amount of work I put into the development of Sb doped ZnO nanowires, there is still room for future investigations. While I believe this growth technique has potential for commercialization, there are certain limitations that need to be looked into. In order to provide guidance for future researchers who choose to continue where my research left off, here are a few recommendations.

1. Fundamental electrical characterization is needed to quantify doping. While the amount of Sb added to the growth solution is known, how much is actually integrated into the ZnO lattice, and how much of it is electrically active is unknown. This will require

extensive study of the microstructure, the electrical properties, and probably some extensive molecular dynamics simulation work.

2. The homojunction gesture recognition study can be pursued in more detail. These measurements were performed only by measuring one group of muscles at a time. However, if multiple groups, such as the extensors and tensors on the back of the hand and the wrist, were measured in parallel, much more complex signals could be obtained. A collaborative effort with groups in biomedical engineering could also bring out the full potential of this concept.

3. The ZnO/Si heterojunction structure showed promise for optoelectronics. It may be of interest to see how well *p*-type ZnO can be integrated with other semiconductors such as CdSe or GaN, especially as these have shown interesting piezophototronic applications in the past.

4. Development of patterned growth would be of interest for future device work. The commonly used lithography techniques for patterned ZnO nanowire arrays in the past are not compatible with the growth environment used for the nanowire solution I developed due to the instability of photoresists in high concentrations of ammonia. Therefore, a much more involved process involving patterning of inorganic materials such as SiO_2 as a mask may be necessary to do so.

APPENDIX A: STEM OF SB DOPED NANOWIRE

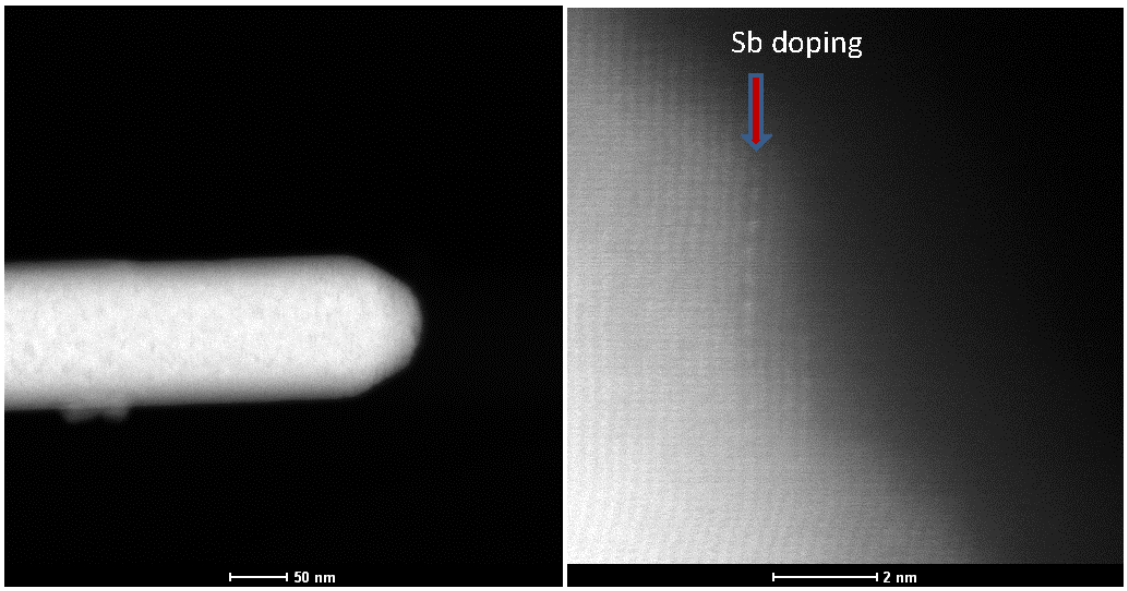

Figure 35 Low magnification and high magnification annular-dark-field (Z-contrast) scanning transmission electron microscopy images of a Sb doped ZnO nanowire.[46]

APPENDIX B: DETERMINATION OF APPLIED STRAIN

Strain calculations were adapted from Saint-Venant bending theory[86]. The formula used to calculate strain perpendicular to the wire film's polar axis was:

$$\varepsilon = 3\frac{a}{l}\frac{D_{max}}{l}\left(1 - \frac{z_0}{l}\right)$$

where $2a$ and l are the substrate thickness (0.0127 cm) and length (1.5 cm), respectively. D_{max} is the deflection experienced by the substrate (1 cm), and z_0 is the distance from the fixed end of the substrate to the center nanowire film (0.5 cm). The deflection was performed at a constant velocity of 5 mm/s, and acceleration of 5 mm/s^2. The value of ε is positive as the film is under tensile strain. Poisson's ratio of ZnO ($v = 0.3492$) is used to find the compressive strain experienced along the film's axis, so the final equation for strain is

$$\varepsilon_{trans} = -v\varepsilon_{axial} = -3v\frac{a}{l}\frac{D_{max}}{l}\left(1 - \frac{z_0}{l}\right) = -0.22\%$$

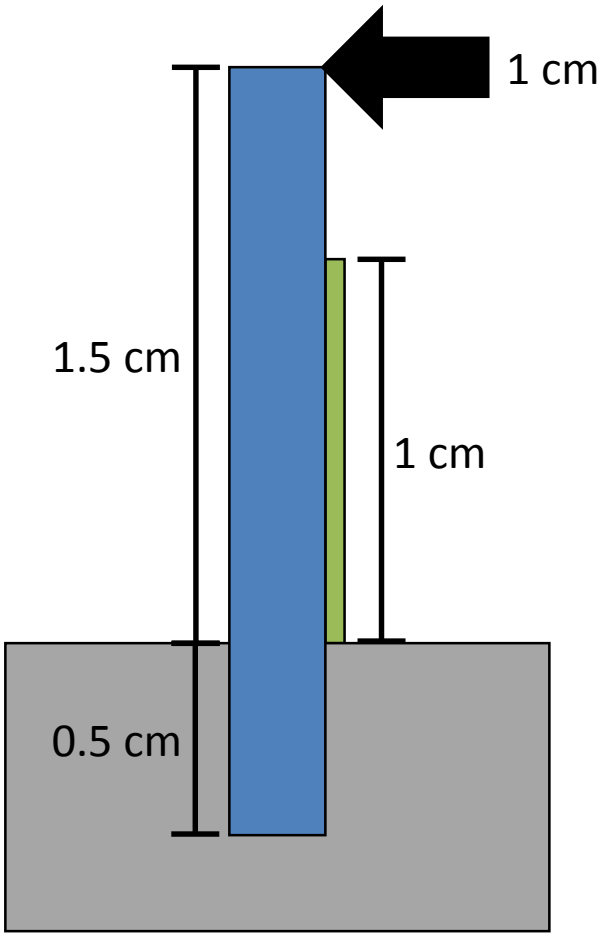

Figure 36 Schematic of testing setup used to measure piezoelectric output. Substrate and film dimensions are exaggerated for clarity.[87]

APPENDIX C: SHORT-CIRCUIT CURRENT AND POWER UNDER LOAD OF HOMOJUNCTION NANOGENERATORS

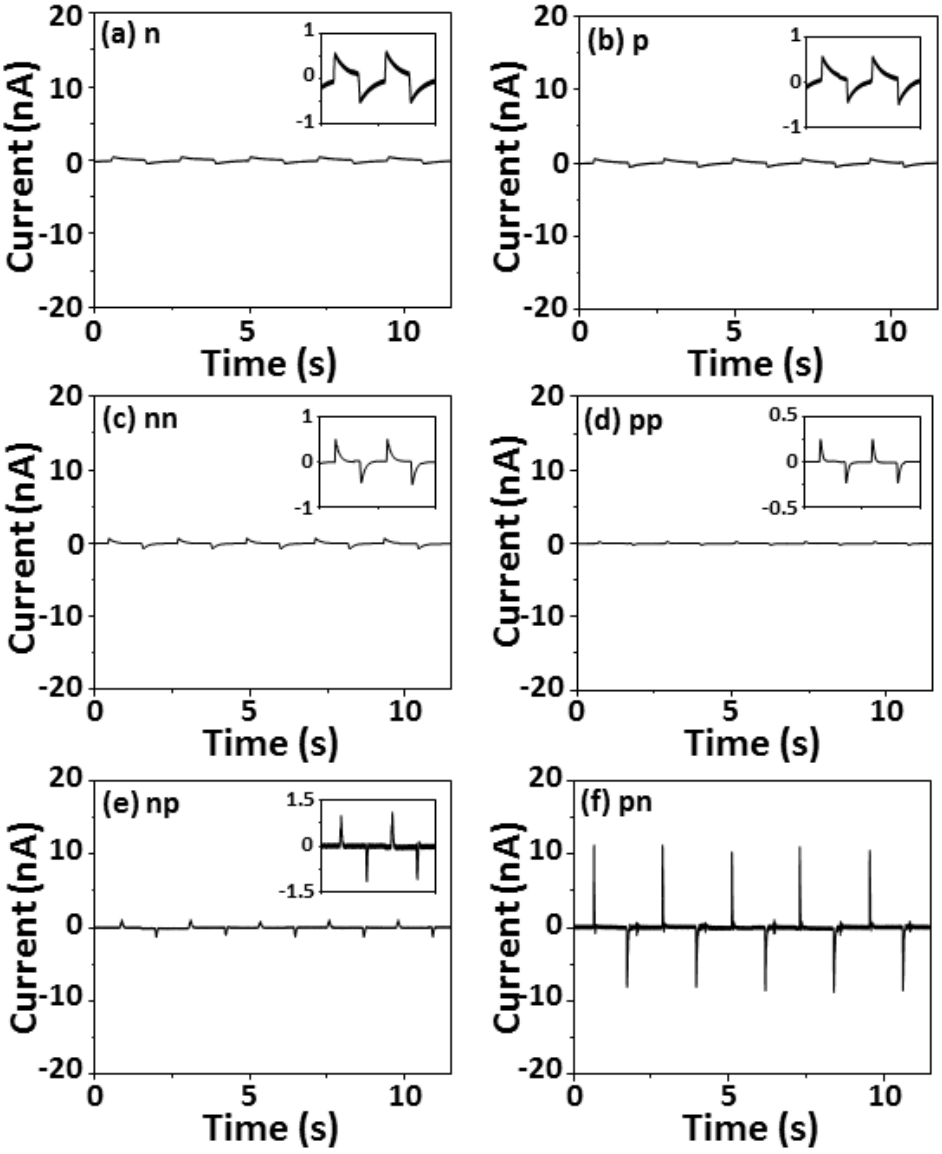

Figure 37 Short circuit current of homojunction nanogenerators in various growth orders[87]

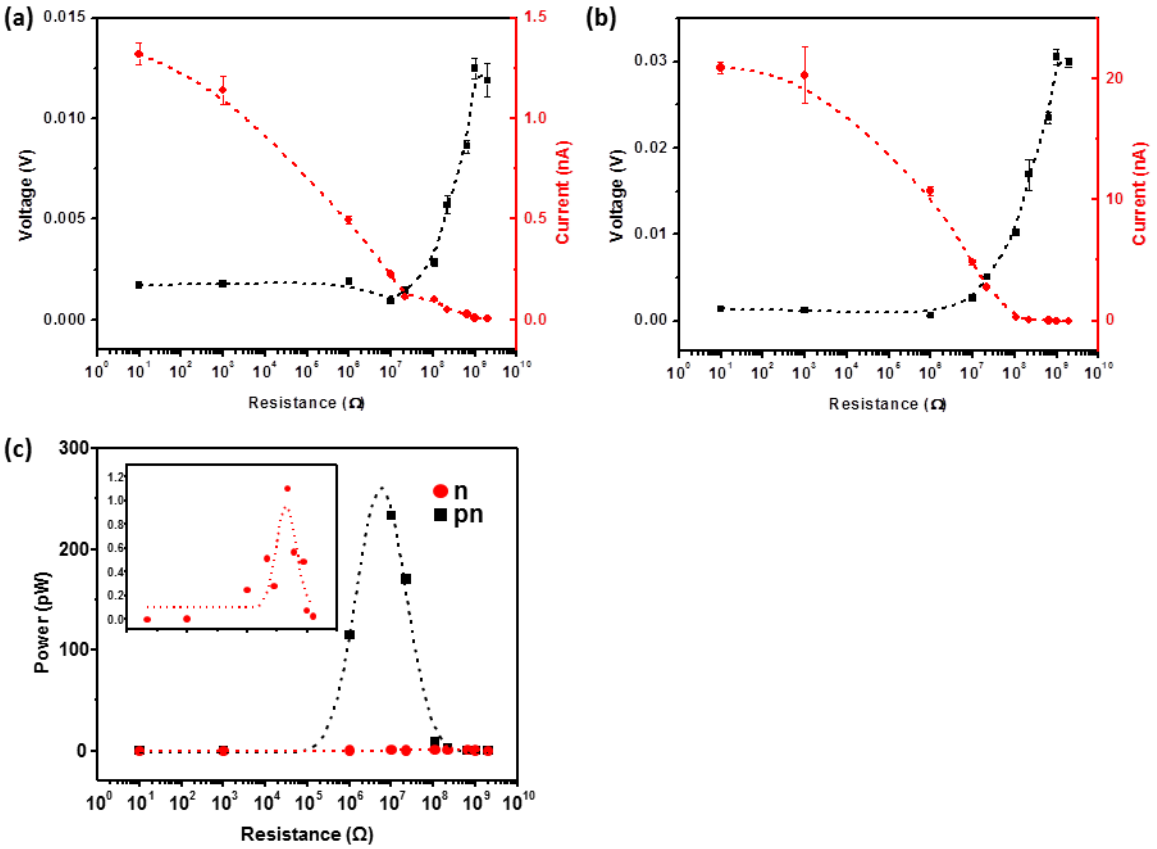

Figure 38 Current and voltage output for (a) n and (b) pn devices as a function of load resistance. (c) Calculated peak power output for the two devices under different loads. The inset shows a zoomed in view of the trend for the n sample. A maximum peak power output of 232 pW was achieved for the pn device, while only 1.1 pW was achieved in the baseline n device.[87]

APPENDIX D: OUTPUT CURRENT OF PLASMA TREATED HOMOJUNCTION DEVICES

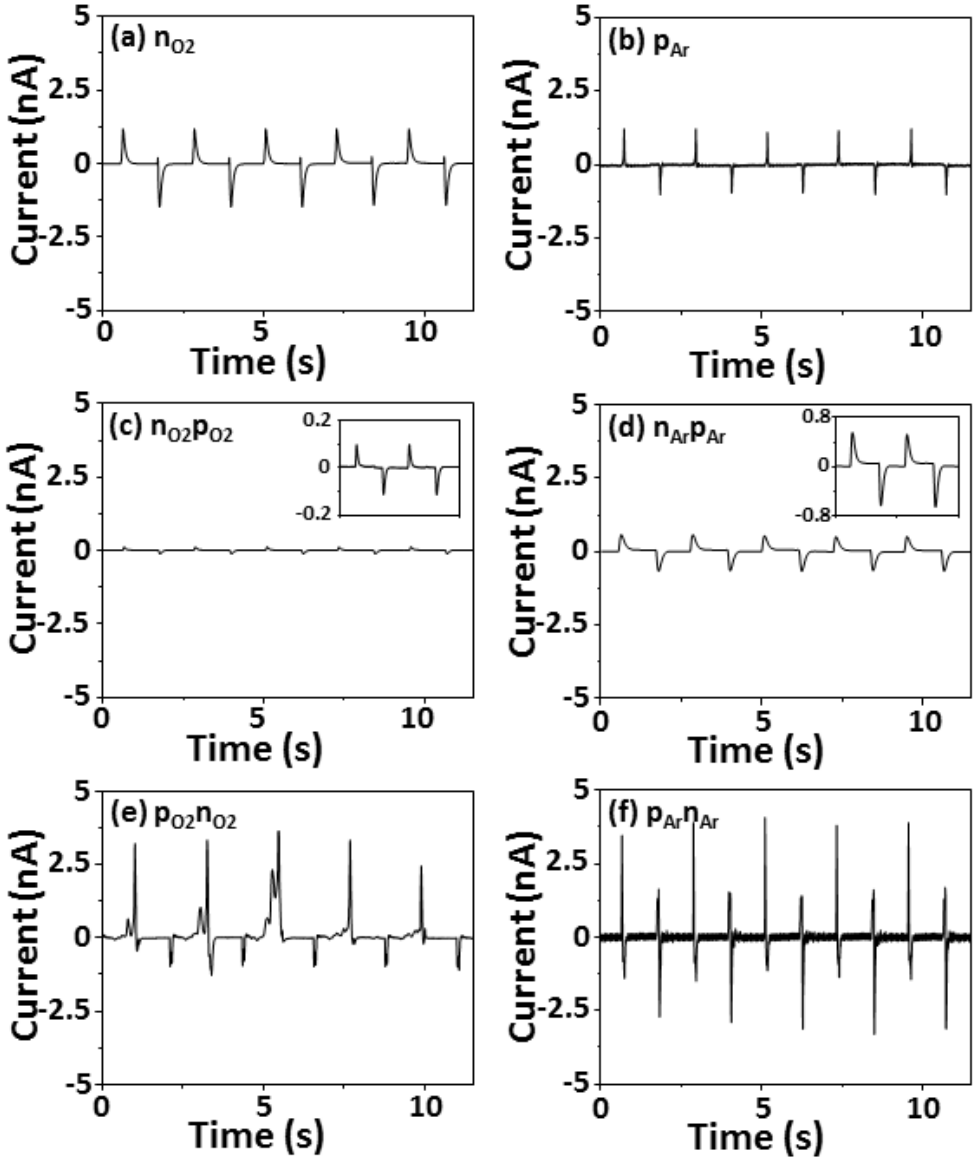

Figure 39 Output current corresponding to the plasma treated devices[87]

APPENDIX E: RAW OUTPUT OF NANOGENERATOR FOR GESTURE DETECTION

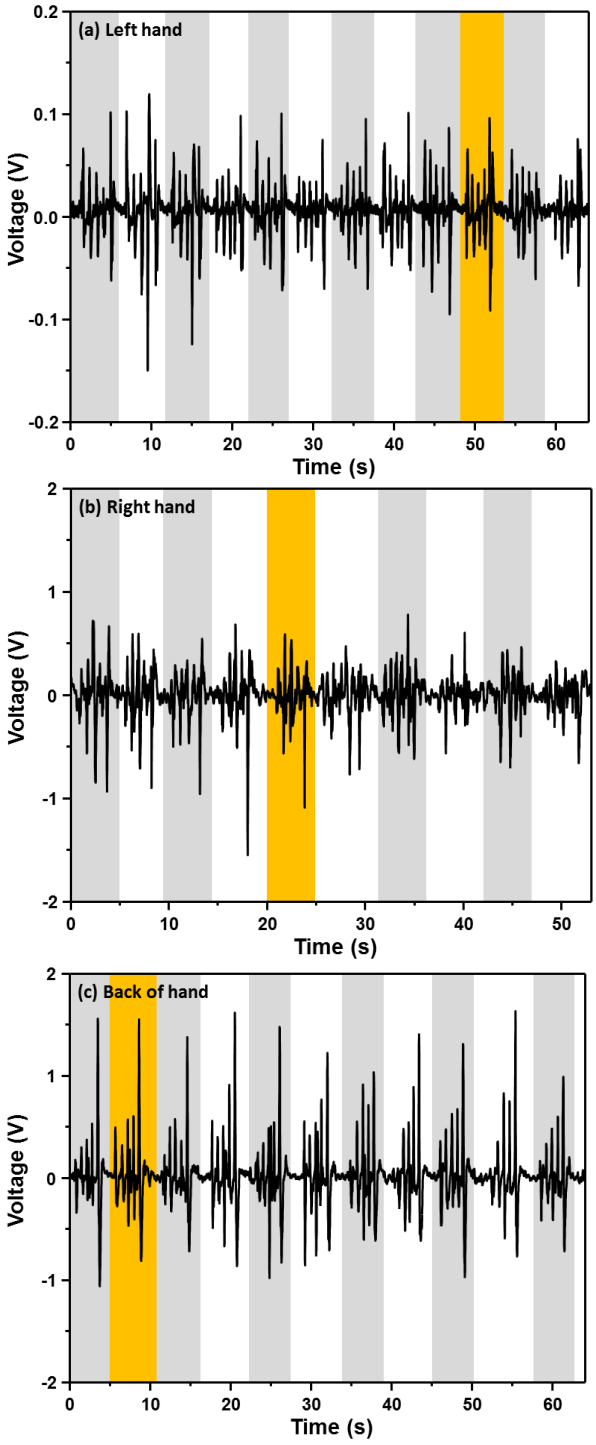

Figure 40 Raw voltage output for the (a) left, (b) right, and (c) back of hand sequence. The sequences highlighted in orange are those selected.[87]

REFERENCES

1. Wang, Z. L. *Advanced Materials* **2007,** 19, (6), 889-892.
2. Lyons, J. L.; Janotti, A.; Van de Walle, C. G. *Applied Physics Letters* **2009,** 95, (25), 252105.
3. Wang, Z. L. *Materials Science and Engineering: R: Reports* **2009,** 64, (3–4), 33-71.
4. Wang, Z. L. *MRS Bulletin* **2012,** 37, (09), 814-827.
5. Yang, R.; Qin, Y.; Dai, L.; Wang, Z. L. *Nat Nano* **2009,** 4, (1), 34-39.
6. Wang, Z. L.; Song, J. *Science* **2006,** 312, (5771), 242-246.
7. Hu, Y.; Lin, L.; Zhang, Y.; Wang, Z. L. *Advanced Materials* **2012,** 24, (1), 110-114.
8. Xu, S.; Qin, Y.; Xu, C.; Wei, Y.; Yang, R.; Wang, Z. L. *Nat Nano* **2010,** 5, (5), 366-373.
9. Zhu, G.; Wang, A. C.; Liu, Y.; Zhou, Y.; Wang, Z. L. *Nano Letters* **2012,** 12, (6), 3086-3090.
10. Wu, W.; Wei, Y.; Wang, Z. L. *Advanced Materials* **2010,** 22, (42), 4711-4715.
11. Zhang, Y.; Liu, Y.; Wang, Z. L. *Advanced Materials* **2011,** 23, (27), 3004-3013.
12. Wang, Z. L. *Advanced Materials* **2012,** 24, (34), 4632-4646.
13. Wang, Z. L., Introduction of Piezotronics and Piezo-Phototronics. In *Piezotronics and Piezo-Phototronics*, Springer: 2012; pp 1-17.
14. Wu, W.; Wang, Z. L. *Nano Letters* **2011,** 11, (7), 2779-2785.
15. Wu, W.; Wen, X.; Wang, Z. L. *Science* **2013,** 340, (6135), 952-957.
16. Wang, Z. L. *The Journal of Physical Chemistry Letters* **2010,** 1, (9), 1388-1393.
17. Hu, Y.; Chang, Y.; Fei, P.; Snyder, R. L.; Wang, Z. L. *ACS Nano* **2010,** 4, (2), 1234-1240.
18. Yang, Q.; Guo, X.; Wang, W.; Zhang, Y.; Xu, S.; Lien, D. H.; Wang, Z. L. *ACS Nano* **2010,** 4, (10), 6285-6291.
19. Liu, Y.; Yang, Q.; Zhang, Y.; Yang, Z.; Wang, Z. L. *Advanced Materials* **2012,** 24, (11), 1410-1417.
20. Zhang, F.; Ding, Y.; Zhang, Y.; Zhang, X.; Wang, Z. L. *ACS Nano* **2012,** 6, (10), 9229-9236.
21. Yang, Y.; Guo, W.; Zhang, Y.; Ding, Y.; Wang, X.; Wang, Z. L. *Nano Letters* **2011,** 11, (11), 4812-4817.
22. Pan, C.; Niu, S.; Ding, Y.; Dong, L.; Yu, R.; Liu, Y.; Zhu, G.; Wang, Z. L. *Nano Letters* **2012,** 12, (6), 3302-3307.
23. Yang, Q.; Wang, W.; Xu, S.; Wang, Z. L. *Nano Letters* **2011,** 11, (9), 4012-4017.
24. Pan, C.; Dong, L.; Zhu, G.; Niu, S.; Yu, R.; Yang, Q.; Liu, Y.; Wang, Z. L. *Nat Photon* **2013,** 7, (9), 752-758.
25. Pan, Z. W.; Wang, Z. L. *Science* **2001,** 291, (5510), 1947-1949.
26. Heo, Y. W.; Varadarajan, V.; Kaufman, M.; Kim, K.; Norton, D. P.; Ren, F.; Fleming, P. H. *Applied Physics Letters* **2002,** 81, (16), 3046-3048.

27. Greene, L. E.; Law, M.; Goldberger, J.; Kim, F.; Johnson, J. C.; Zhang, Y.; Saykally, R. J.; Yang, P. *Angewandte Chemie International Edition* **2003,** 42, (26), 3031-3034.
28. Greene, L. E.; Yuhas, B. D.; Law, M.; Zitoun, D.; Yang, P. *Inorganic Chemistry* **2006,** 45, (19), 7535-7543.
29. Xu, S.; Adiga, N.; Ba, S.; Dasgupta, T.; Wu, C. F. J.; Wang, Z. L. *ACS Nano* **2009,** 3, (7), 1803-1812.
30. Xu, S.; Lao, C.; Weintraub, B.; Wang, Z. L. *Journal of Materials Research* **2008,** 23, (08), 2072-2077.
31. Song, J.; Baek, S.; Lee, J.; Lim, S. *Journal of Chemical Technology & Biotechnology* **2008,** 83, (3), 345-350.
32. Li, W.-J.; Shi, E.-W.; Zhong, W.-Z.; Yin, Z.-W. *Journal of Crystal Growth* **1999,** 203, (1–2), 186-196.
33. Le, H. Q.; Chua, S. J.; Koh, Y. W.; Loh, K. P.; Fitzgerald, E. A. *Journal of Crystal Growth* **2006,** 293, (1), 36-42.
34. Xu, S.; Wei, Y.; Kirkham, M.; Liu, J.; Mai, W.; Davidovic, D.; Snyder, R. L.; Wang, Z. L. *Journal of the American Chemical Society* **2008,** 130, (45), 14958-14959.
35. Yuan, D.; Guo, R.; Wei, Y.; Wu, W.; Ding, Y.; Wang, Z. L.; Das, S. *Advanced Functional Materials* **2010,** 20, (20), 3484-3489.
36. Ji, L.-W.; Peng, S.-M.; Wu, J.-S.; Shih, W.-S.; Wu, C.-Z.; Tang, I. T. *Journal of Physics and Chemistry of Solids* **2009,** 70, (10), 1359-1362.
37. Song, J.; Lim, S. *The Journal of Physical Chemistry C* **2006,** 111, (2), 596-600.
38. Ghayour, H.; Rezaie, H. R.; Mirdamadi, S.; Nourbakhsh, A. A. *Vacuum* **2011,** 86, (1), 101-105.
39. Baruah, S.; Dutta, J. *Science and Technology of Advanced Materials* **2009,** 10, (1), 013001.
40. Tian, Z. R.; Voigt, J. A.; Liu, J.; McKenzie, B.; McDermott, M. J.; Rodriguez, M. A.; Konishi, H.; Xu, H. *Nat Mater* **2003,** 2, (12), 821-826.
41. Zhang; Yanagisawa, K. *Chemistry of Materials* **2007,** 19, (9), 2329-2334.
42. Sun, K.; Wei, W.; Ding, Y.; Jing, Y.; Wang, Z. L.; Wang, D. *Chemical Communications* **2011,** 47, (27), 7776-7778.
43. Zhang, H.; Yang, D.; Li, D.; Ma, X.; Li, S.; Que, D. *Crystal Growth & Design* **2005,** 5, (2), 547-550.
44. Xu, C.; Shin, P.; Cao, L.; Gao, D. *The Journal of Physical Chemistry C* **2009,** 114, (1), 125-129.
45. Wang, L.; Tsan, D.; Stoeber, B.; Walus, K. *Advanced Materials* **2012,** 24, (29), 3999-4004.
46. Pradel, K. C.; Wu, W. Z.; Zhou, Y. S.; Wen, X. N.; Ding, Y.; Wang, Z. L. *Nano Letters* **2013,** 13, (6), 2647-2653.
47. Lu, M.-P.; Lu, M.-Y.; Chen, L.-J. *Nano Energy* **2012,** 1, (2), 247-258.
48. Fan, J. C.; Sreekanth, K. M.; Xie, Z.; Chang, S. L.; Rao, K. V. *Progress in Materials Science* **2013,** 58, (6), 874-985.
49. Zhang, S. B.; Wei, S. H.; Zunger, A. *Physical Review B* **2001,** 63, (7), 075205.
50. Van de Walle, C. G. *Physical Review Letters* **2000,** 85, (5), 1012-1015.
51. Janotti, A.; Van de Walle, C. G. *Applied Physics Letters* **2005,** 87, (12), -.
52. Kim, Y.-S.; Park, C. H. *Physical Review Letters* **2009,** 102, (8), 086403.

53. Lany, S.; Zunger, A. *Physical Review B* **2005,** 72, (3), 035215.
54. Yuan, G. D.; Zhang, W. J.; Jie, J. S.; Fan, X.; Zapien, J. A.; Leung, Y. H.; Luo, L. B.; Wang, P. F.; Lee, C. S.; Lee, S. T. *Nano Letters* **2008,** 8, (8), 2591-2597.
55. Lu, M.-P.; Song, J.; Lu, M.-Y.; Chen, M.-T.; Gao, Y.; Chen, L.-J.; Wang, Z. L. *Nano Letters* **2009,** 9, (3), 1223-1227.
56. Cao, B. Q.; Lorenz, M.; Rahm, A.; Wenckstern, H. v.; Czekalla, C.; Lenzner, J.; Benndorf, G.; Grundmann, M. *Nanotechnology* **2007,** 18, (45), 455707.
57. Look, D. C.; Reynolds, D. C.; Litton, C. W.; Jones, R. L.; Eason, D. B.; Cantwell, G. *Applied Physics Letters* **2002,** 81, (10), 1830-1832.
58. Sun, J. W.; Lu, Y. M.; Liu, Y. C.; Shen, D. Z.; Zhang, Z. Z.; Li, B. H.; Zhang, J. Y.; Yao, B.; Zhao, D. X.; Fan, X. W. *Solid State Communications* **2006,** 140, (7–8), 345-348.
59. Xiang, B.; Wang, P.; Zhang, X.; Dayeh, S. A.; Aplin, D. P. R.; Soci, C.; Yu, D.; Wang, D. *Nano Letters* **2006,** 7, (2), 323-328.
60. Lee, J.; Cha, S.; Kim, J.; Nam, H.; Lee, S.; Ko, W.; Wang, K. L.; Park, J.; Hong, J. *Advanced Materials* **2011,** 23, (36), 4183-4187.
61. Tay, C. B.; Chua, S. J.; Loh, K. P. *The Journal of Physical Chemistry C* **2010,** 114, (21), 9981-9987.
62. Tay, C. B.; Tang, J.; Nguyen, X. S.; Huang, X. H.; Chai, J. W.; Venkatesan, V. T.; Chua, S. J. *The Journal of Physical Chemistry C* **2012,** 116, (45), 24239-24247.
63. Fang, X.; Li, J.; Zhao, D.; Shen, D.; Li, B.; Wang, X. *The Journal of Physical Chemistry C* **2009,** 113, (50), 21208-21212.
64. Hwang, S.-H.; Moon, K.-J.; Lee, T. I.; Lee, W.; Myoung, J.-M. *Materials Chemistry and Physics* **2014,** 143, (2), 600-604.
65. Limpijumnong, S.; Zhang, S. B.; Wei, S.-H.; Park, C. H. *Physical Review Letters* **2004,** 92, (15), 155504.
66. Wang, F.; Seo, J. H.; Bayerl, D.; Shi, J. A.; Mi, H. Y.; Ma, Z. Q.; Zhao, D. Y.; Shuai, Y. C.; Zhou, W. D.; Wang, X. D. *Nanotechnology* **2011,** 22, (22).
67. Yankovich, A. B.; Puchala, B.; Wang, F.; Seo, J. H.; Morgan, D.; Wang, X. D.; Ma, Z. Q.; Kvit, A. V.; Voyles, P. M. *Nano Letters* **2012,** 12, (3), 1311-1316.
68. Lin, S.; Song, J.; Lu, Y.; Wang, Z. *Nanotechnology* **2009,** 20, (36), 365703.
69. Hu, Y.; Zhang, Y.; Lin, L.; Ding, Y.; Zhu, G.; Wang, Z. L. *Nano Letters* **2012,** 12, (7), 3851-3856.
70. Chung, S. Y.; Kim, S.; Lee, J.-H.; Kim, K.; Kim, S.-W.; Kang, C.-Y.; Yoon, S.-J.; Kim, Y. S. *Advanced Materials* **2012,** 24, (45), 6022-6027.
71. Briscoe, J.; Stewart, M.; Vopson, M.; Cain, M.; Weaver, P. M.; Dunn, S. *Advanced Energy Materials* **2012,** 2, (10), 1261-1268.
72. Sun, K.; Jing, Y.; Park, N.; Li, C.; Bando, Y.; Wang, D. *Journal of the American Chemical Society* **2010,** 132, (44), 15465-15467.
73. Um, H.-D.; Moiz, S. A.; Park, K.-T.; Jung, J.-Y.; Jee, S.-W.; Ahn, C. H.; Kim, D. C.; Cho, H. K.; Kim, D.-W.; Lee, J.-H. *Applied Physics Letters* **2011,** 98, (3), 033102.
74. Urgessa, Z. N.; Dobson, S. R.; Talla, K.; Murape, D. M.; Venter, A.; Botha, J. R. *Physica B: Condensed Matter* **2014,** 439, 149-152.
75. Wang, Z.; Yu, R.; Wen, X.; Liu, Y.; Pan, C.; Wu, W.; Wang, Z. L. *ACS Nano* **2014,** 8, (12), 12866-12873.
76. Fan, H. J.; Werner, P.; Zacharias, M. *Small* **2006,** 2, (6), 700-717.

77. Wagner, R.; Ellis, W., *Vapor-liquid-solid mechanism of crystal growth and its application to silicon*. Bell Telephone Laboratories: 1965.
78. Peng, K. Q.; Lee, S. T. *Advanced Materials* **2011,** 23, (2), 198-215.
79. Chou, S. Y.; Krauss, P. R.; Renstrom, P. J. *Journal of Vacuum Science & Technology B* **1996,** 14, (6), 4129-4133.
80. Morton, K. J.; Nieberg, G.; Bai, S.; Chou, S. Y. *Nanotechnology* **2008,** 19, (34), 345301.
81. Yu, Z.; Gao, H.; Wu, W.; Ge, H.; Chou, S. Y. *Journal of Vacuum Science & Technology B* **2003,** 21, (6), 2874-2877.
82. Laermer, F.; Schilp, A., Method for anisotropic plasma etching of substrates. Google Patents: 1996.
83. Davey, R. *Journal of Crystal Growth* **1976,** 34, (1), 109-119.
84. Porter, D. A.; Easterling, K. E.; Sherif, M., *Phase Transformations in Metals and Alloys*. CRC press: 2009.
85. Ding, Y.; Zhang, F.; Wang, Z. *Nano Res.* **2013,** 6, (4), 253-262.
86. Zhou, J.; Gu, Y.; Fei, P.; Mai, W.; Gao, Y.; Yang, R.; Bao, G.; Wang, Z. L. *Nano Letters* **2008,** 8, (9), 3035-3040.
87. Pradel, K. C.; Wu, W.; Ding, Y.; Wang, Z. L. *Nano Letters* **2014,** 14, (12), 6897-6905.
88. Kingon, A. I.; Srinivasan, S. *Nature Materials* **2005,** 4, (3), 233-237.
89. Zhou, J.; Fei, P.; Gao, Y.; Gu, Y.; Liu, J.; Bao, G.; Wang, Z. L. *Nano Letters* **2008,** 8, (9), 2725-2730.
90. Gao, Y.; Wang, Z. L. *Nano Letters* **2007,** 7, (8), 2499-2505.
91. Dagdeviren, C.; Yang, B. D.; Su, Y. W.; Tran, P. L.; Joe, P.; Anderson, E.; Xia, J.; Doraiswamy, V.; Dehdashti, B.; Feng, X.; Lu, B. W.; Poston, R.; Khalpey, Z.; Ghaffari, R.; Huang, Y. G.; Slepian, M. J.; Rogers, J. A. *P Natl Acad Sci USA* **2014,** 111, (5), 1927-1932.
92. Li, Z.; Zhu, G.; Yang, R.; Wang, A. C.; Wang, Z. L. *Advanced Materials* **2010,** 22, (23), 2534-2537.
93. Lee, S.; Hinchet, R.; Lee, Y.; Yang, Y.; Lin, Z.-H.; Ardila, G.; Montès, L.; Mouis, M.; Wang, Z. L. *Advanced Functional Materials* **2014,** 24, (8), 1163-1168.
94. Gallo, L.; Placitelli, A. P.; Ciampi, M. In *Controller-free exploration of medical image data: Experiencing the Kinect*, Computer-Based Medical Systems (CBMS), 2011 24th International Symposium on, 27-30 June 2011, 2011; pp 1-6.
95. Burger, B.; Ferrané, I.; Lerasle, F.; Infantes, G. *Autonomous Robots* **2012,** 32, (2), 129-147.
96. Xu, Z.; Xiang, C.; Yun, L.; Lantz, V.; Kongqiao, W.; Jihai, Y. *Systems, Man and Cybernetics, Part A: Systems and Humans, IEEE Transactions on* **2011,** 41, (6), 1064-1076.
97. Fukui, R.; Watanabe, M.; Shimosaka, M.; Sato, T. *The International Journal of Robotics Research* **2014**.
98. Jeong, J. W.; Yeo, W. H.; Akhtar, A.; Norton, J. J. S.; Kwack, Y. J.; Li, S.; Jung, S. Y.; Su, Y. W.; Lee, W.; Xia, J.; Cheng, H. Y.; Huang, Y. G.; Choi, W. S.; Bretl, T.; Rogers, J. A. *Advanced Materials* **2013,** 25, (47), 6839-6846.
99. Ferren, R. A. *Nature* **1991,** 350, (6319), 26-27.

100. Drake, R.; Vogl, A. W.; Mitchell, A. W. M., *Gray's Anatomy for Students*. Elsevier Health Sciences: 2009.
101. Wang, K.; Chen, J.; Zeng, Z.; Tarr, J.; Zhou, W.; Zhang, Y.; Yan, Y.; Jiang, C.; Pern, J.; Mascarenhas, A. *Applied Physics Letters* **2010,** 96, (12), 123105.
102. Wang, K.; Chen, J.; Zhou, W.; Zhang, Y.; Yan, Y.; Pern, J.; Mascarenhas, A. *Adv. Mater* **2008,** 20, (17), 3248-3253.
103. Si, S.; Li, C.; Wang, X.; Peng, Q.; Li, Y. *Sensors and Actuators B: Chemical* **2006,** 119, (1), 52-56.
104. Chen, Y.-J.; Zhang, F.; Zhao, G.-g.; Fang, X.-y.; Jin, H.-B.; Gao, P.; Zhu, C.-L.; Cao, M.-S.; Xiao, G. *The Journal of Physical Chemistry C* **2010,** 114, (20), 9239-9244.
105. Law, M.; Greene, L. E.; Radenovic, A.; Kuykendall, T.; Liphardt, J.; Yang, P. *The Journal of Physical Chemistry B* **2006,** 110, (45), 22652-22663.
106. Nguyen, X. S.; Tay, C. B.; Fitzgerald, E. A.; Chua, S. J. *Small* **2012,** 8, (8), 1204-1208.
107. Baeg, K.-J.; Binda, M.; Natali, D.; Caironi, M.; Noh, Y.-Y. *Advanced Materials* **2013,** 25, (31), 4267-4295.
108. Sun, K.; Jing, Y.; Li, C.; Zhang, X.; Aguinaldo, R.; Kargar, A.; Madsen, K.; Banu, K.; Zhou, Y.; Bando, Y.; Liu, Z.; Wang, D. *Nanoscale* **2012,** 4, (5), 1515-1521.
109. Hu, Y.; Zhang, Y.; Xu, C.; Lin, L.; Snyder, R. L.; Wang, Z. L. *Nano letters* **2011,** 11, (6), 2572-2577.
110. Cheng, J.; Poduska, K. M. *ECS Journal of Solid State Science and Technology* **2014,** 3, (5), P133-P137.
111. Lupan, O.; Pauporté, T.; Chow, L.; Viana, B.; Pellé, F.; Ono, L. K.; Roldan Cuenya, B.; Heinrich, H. *Applied Surface Science* **2010,** 256, (6), 1895-1907.
112. Muth, J.; Kolbas, R.; Sharma, A.; Oktyabrsky, S.; Narayan, J. *Journal of Applied Physics* **1999,** 85, (11), 7884-7887.
113. Yoshihiro, H.; Noboru, N.; Shinya, T.; Shoichi, N.; Yasuo, K.; Yukinori, K. *Japanese Journal of Applied Physics* **1991,** 30, (5R), 1008.